# Assessing Element Recycling within Subduction Zones and the Deep Mantle based on Molybdenum Isotopes

Inaugural Dissertation
of the Faculty of Science,
University of Bern

presented by

**Qasid Ahmad**

from Germany

Supervisor of the doctoral thesis:
PD. Dr. Martin Wille
Prof. Dr. Klaus Mezger
Institute of Geological Sciences, University of Bern

# Assessing Element Recycling within Subduction Zones and the Deep Mantle based on Molybdenum Isotopes

Inaugural Dissertation
of the Faculty of Science,
University of Bern

presented by

**Qasid Ahmad**

from Germany

Supervisor of the doctoral thesis:
PD. Dr. Martin Wille
Prof. Dr. Klaus Mezger
Institute of Geological Sciences

Accepted by the Faculty of Science.

Bern, 14.03.2023

The Dean
Prof. Dr. Marco Herwegh

# Acknowledgements

First and foremost I would like to thank Martin Wille for giving me the opportunity to work on such an exciting project and discover the world of non-traditional isotope geochemistry. You have been the best supervisor one could imagine, and it was an honor to work with you. In these past four years, I enjoyed the healthy balance between the scientific freedom and guidance maintained by you, which allowed me to become, I hope, a proper scientist. I am also grateful to my co-supervisor Klaus Mezger for his guidance throughout the project. I really enjoyed the discussions on science but also other topics despite our Baden-Swabia rivalry. I am grateful to Helen Williams, who agreed to evaluate this thesis as an external examiner. This thesis is funded by the Swiss National Science Foundation (grant number 182508).

I am indebted to Jörg Hermann for chairing my defense, reading my introduction, and stimulating discussions and feedback throughout the project. The input from you and Thomas Pettke during fieldwork enabled me to loosen my relatively tight-fitted isotope geochemist hat and expand my knowledge in petrology. My thanks also go to Stephan König and Carolina Rosca for their continuous support and valuable discussions. Through both of you and Jabrane Labidi, I had the opportunity to work on “side projects”, which eventually became main projects and greatly contributed to my understanding of mantle geochemistry.

I would like to thank Alessandro, Arathy, Edel, and Dipankar for their help and guidance with lab- or Neptune-related issues especially during unusual hours. I would like to thank Jan, Aryavart, Sukalpa, Pascal, and Adrianus for the long hours that passed in the clean lab. The Springfield Isotopes became friends throughout the last years. I greatly enjoyed being part of office 207. I want to thank in particular Julijana, the “mother” of the office, and Timothy, the best company during night shifts. I would like to acknowledge the relaxed atmosphere. The frequent visits of Bennet have certainly contributed to that. I would like to extend my gratitude to so far unmentioned colleagues and friends, who I cannot all list here. The social bond built in this group is truly exceptional.

I would like to thank my family for their everlasting support and encouragement. I dedicate this thesis to my dearest parents, whose continuous sacrifice and support have given me the best opportunities in life, Alhamdulillah.

# Contents

# Introduction

# Introduction

Subduction zone processes are a key mechanism for chemical exchange between Earth's surface and interior. This exchange influences solid Earth's principal geochemical reservoirs by redistributing elements during Earth's evolution. This bidirectional mass transport between Earth's crust and mantle results in mineralogical and chemical heterogeneities within Earth's silicate reservoirs. Quantifying mass and element fluxes into subduction zones allows constraining processes and conditions that control element transfer from the slab to the mantle wedge, which is crucial to evaluate the evolution of the continental crust and the mantle through Earth's history. This element exchange determines the chemical composition of Earth's mantle, crust, atmosphere, and hydrosphere, and consequently has an impact on the evolution of complex life (e.g., Zerkle, 2018; Hawkesworth et al., 2020).

An intrinsic feature of subduction zones is the complex interplay between the input of diverse material from the surface into the mantle and its recycling into the overlying mantle wedge by slab-derived fluids (e.g., Tatsumi and Eggins, 1995). These fluids are released at different stages of subduction with an initial discharge of pore water during early compaction of subducted sediment and oceanic crust followed by dehydration reactions of hydrous minerals in the slab and the underlying metasomatized mantle during increasing P-T conditions. At sufficiently hot conditions, hydrous melts can form from the sediments or the oceanic crust (e.g., Hermann and Spandler, 2008). Fluids that enter the overlying mantle wedge trigger flux melting of the mantle peridotite forming arc magmas leading to the formation of a new continental crust. During this process, certain slab-derived elements can be efficiently mobilized and enter the newly generated magma. The mobility of elements in these different fluids is dependent on subduction zone conditions such as temperature, oxidation state, and the stability of (metamorphic) minerals in the subducted slab that can retain elements depending on their compatibility (e.g., Klimm et al., 2008; Hermann and Rubatto, 2009; Plank et al., 2009). These parameters dictate the different extent and modes of element recycling in subduction zones and lead to variability in element mobility in aqueous fluids or hydrous melts and the slab composition. In sum, the geochemical composition of newly formed rocks in arc magmatic settings can be seen as the superimposition of three components that are mixed to different extents: the subarc mantle wedge, aqueous fluids, and hydrous melts. For aqueous fluid and hydrous melt, there are different signatures for fluids and melts from subducted sediments, altered oceanic crust and unaltered oceanic crust (e.g., Elliott, 2003; Hermann et al., 2006; Li et al., 2022). This adds additional complexity.

To determine the processes that control element cycling within arc settings a variety of approaches have been applied. These include the study of natural samples such as arc lavas and high- to ultrahigh-pressure metamorphic rocks, experimental studies performed at subduction-relevant P-T conditions, as well as numerical and thermodynamic modeling (e.g., Spandler and Pirard, 2013). The comparison of geochemical information between subduction input material such as sediments and altered oceanic crust (AOC) and the subduction output material such as primitive arc lavas, allows to quantitative mass balance elements and to identify subducted crustal material as a major source of certain elements (e.g., Plank and Langmuir, 1993; Elliott, 2003; Bebout, 2014). These geochemical data include major- and trace element geochemistry and radiogenic isotopes (such as Sr, Nd, and Pb). For example, specific patterns in primitive mantle normalized element diagrams support enrichments and depletion of elements such as Pb and Nb that are characteristic for arc magmas. These distinctive patterns are attributed to the specific mobility of elements from the subducting slab and the stability of (accessory) mineral phases in the slab that can retain certain elements (e.g., Keppler, 1996; Kessel et al., 2005; Hermann and Rubatto, 2009). The mobility of elements in subduction zone settings is dependent on the mineralogical composition of the subducted material and the prevailing physical and chemical conditions including pressure, temperature, fluid salinity, and redox state. These findings are mainly based on studies on exhumed rocks that have experienced a large range of peak P-T conditions covering the entire forearc region of (paleo-) subduction zones, and experimental studies that were conducted at forearc to subarc-relevant metamorphic conditions. In this sense, different transport mechanisms, apart from aqueous fluids, such as hydrous melts (and supercritical fluids) have gained substantial importance to explain arc magma geochemistry (e.g., Kessel et al., 2005; Hermann et al., 2006; Li et al., 2022).

The subduction of Earth’s surface material that has been geochemically modified by low-temperature processes as well as subduction-related prograde metamorphisms, leads to heterogeneities within the shallow and deep mantle reservoirs (e.g., Stracke, 2012). The origin, nature, and scale of compositional heterogeneity in the Earth’s mantle has been inferred using major- and trace-element geochemistry and radiogenic isotope systematics of geochemically enriched mid-ocean-ridge basalts (MORB), mantle peridotites, mantle xenoliths, and hotspot-influenced volcanic rocks such as ocean-island basalts (OIB) (e.g., Zindler and Hart, 1986; Allègre, 1987; Hofmann, 1997). For example, OIBs and MORBs can host recycled crustal components and have been used to study a complete rock cycle starting from oceanic crust being subducted, mixed into the mantle, and the return of this mixture to the surface via partial melts triggered by hot spot activity. The geochemical imprint on subducted lithologies by low-temperature Earth surface processes such as sediment deposition and hydrothermal alteration as well as subduction-related metamorphic reactions in turn can be directly linked to changing surface conditions. For example, the oxygenation of Earth's atmosphere and hydrosphere has a direct influence on the redox budget of the slab (Evans, 2012). Therefore, the interior of the Earth can provide constraints on the ocean-atmosphere redox evolution through time and possibly the control of these changing Earth surface conditions onto redox conditions during subduction (e.g., Evans, 2012; Labidi et al., 2013; Andersen et al., 2015; Stolper and Bucholz, 2019; Liu et al., 2019; Yierpan et al., 2020).

Although the major inputs at subduction zones can be identified by chemical and isotopic data, there remain considerable uncertainties on the mobility of certain elements within and before subarc regions. This is because of the variety of slab-derived fluids and their release at different subduction P-T conditions and the direct control of their e.g., redox state and fluid salinity that in turn can be poorly constrained. Furthermore, there is still active debate about the origin of the mantle heterogeneity, because besides subduction recycling of crustal material other processes, such as delamination and foundering of the subcontinental lithosphere or different types of mantle metasomatism, can theoretically account for the trace element and radiogenic isotope differences observed in enriched MORBs and OIBs (e.g., Hirschmann and Stolper, 1996; Niu et al., 2002; Donnelly et al., 2004; Willbold and Stracke, 2006; Stracke, 2012).

The development of Multi Collector Inductively Coupled Plasma Mass Spectrometers (MC-ICP-MS) allowed the analysis of non-traditional (heavy) stable isotopes with a precision sufficiently to resolve the isotopic differences between e.g., magmatic rocks, metamorphic rocks, pre-subducted lithologies, and their mineral separates (e.g., Aarons et al., 2021; Tissot and Ibañez-Mejia, 2021; Watkins and Antonelli, 2021). These isotopic differences possibly enable to evaluate processes such as redox-dependent element partitioning between mineral-mineral or mineral-fluid phases (e.g., Chen et al., 2019), allowing to further constrain element recycling in subduction zones as well as the conditions during element mobilization and their potential influence on the deep mantle (Teng et al., 2019 and references therein). This is because stable isotope fractionation that occurs during Earth's surface processes can lead to isotopically distinct subducted reservoirs such as marine sediments or AOC (e.g., Freymuth et al., 2015; Kendall et al., 2017; Aarons et al., 2021). Additionally, metamorphic minerals that form along the prograde subduction path can fractionate the stable isotope composition of heavy elements. Therefore, the stable isotope composition of certain incompatible elements can be applied as a source tracer as well as a proxy for processes occurring within subduction zones that are not directly observable. Moreover, the stable isotope signature of recycled crustal components in hotspot-influenced volcanic rocks can be different compared to products of subcontinental lithosphere recycling as well as mantle metasomatism. Hence, the additional use of stable isotope variations of heavy elements potentially allows deciphering between the different enrichment processes for mantle-derived rocks.

The aim of this thesis is to use high-precision stable Mo isotope ratios of natural samples including arc lavas, pelagic sediments and AOC, and their subducted analogs (metasediments and AOC-type eclogites) to better understand recycling mechanisms and conditions within subduction zones. The Mo isotope composition of hotspot-influenced volcanic rocks was determined to gain complementary insights into the influence of recycled crustal material on the deep mantle heterogeneity. The results of the study are presented in three separate chapters.

The redox-sensitive transition metal Mo has seven stable isotopes, covering a mass range ($\Delta m/m$) of ~8 % and includes the isotopes (abundance in brackets): $^{92}$Mo (14.65%), $^{94}$Mo (9.19%), $^{95}$Mo (15.87%), $^{96}$Mo (16.67%), $^{97}$Mo (9.58%), $^{98}$Mo (24.29%), and $^{100}$Mo (9.74%) (Mayer and Wieser, 2013). Variations in stable Mo isotope compositions are reported in the δ-notation using the parts per thousand deviation of the $^{98}$Mo/$^{95}$Mo ratio relative to the NIST SRM 3134 standard solution:

$$\delta^{98/95}Mo\ (‰) = \left( \frac{\left(\frac{^{98}Mo}{^{95}Mo}\right)_{Sample}}{\left(\frac{^{98}Mo}{^{95}Mo}\right)_{NIST-SRM-3134}} - 1 \right) * 1{,}000$$

Due to its incompatible character during mantle melting, Mo is enriched in the upper continental crust (UCC) ([Mo] = 1.1 µg/g; Rudnick and Gao, 2014) relative to the depleted mantle ([Mo] = 0.025 µg/g; Salters and Stracke, 2004). In the present-day fully oxygenated ocean, Mo is the most abundant transition metal and behaves as a conservative element with an average residence time of ~440,000 years (Miller et al., 2011). Marine sediments commonly display higher enrichments in Mo compared to the UCC, indicating a significant hydrogenous component compared to the lithogenic component. Furthermore, due to its redox-dependent mobility in aqueous solutions (Mo is mainly present as either $Mo^{6+}$ or $Mo^{4+}$ in terrestrial environments) and during low-temperature processes (e.g., water-rock-sediment interactions) at the Earth's surface, Mo can be enriched significantly and develop distinct isotope signatures in different marine sediments and AOC (e.g., Freymuth et al., 2015; Kendall et al., 2017). These processes lead to different isotopic compositions in pre-subduction lithologies compared to the UCC ($\delta^{98/95}$Mo = 0.05 to 0.15 ‰; e.g., Voegelin et al., 2014; Greber et al., 2014; Willbold and Elliott, 2017; Yang et al., 2017) and the rather homogeneous depleted mantle signature ($\delta^{98/95}$Mo = -0.20 ‰; McCoy-West et al., 2019). Thus, the elemental enrichments and distinctive isotope signatures of different subducted lithologies potentially allow the tracing of different sources of slab-derived Mo in arc settings as well as mantle-derived rocks. Moreover, the redox-sensitive fluid and hydrous melt mobility of Mo at different stages of subduction (Bali et al., 2012; Skora et al., 2017; Chowdhury et al., 2022) can give insights into redox conditions of subduction zones. Therefore, Mo is particularly suited to study element recycling within the deep mantle and subduction zones, the associated control of redox conditions during subduction, and possibly its link to Earth's surface oxygenation.

## Chapter 1: The Molybdenum isotope subduction recycling conundrum: A case study from the Tongan subduction zone, Western Alps and Alpine Corsica

Prominent variability in Mo isotopic composition has been documented for modern island arc lavas, but the processes causing this variability are still controversial. This is because mainly three superimposing processes can influence the Mo isotopic composition of island arc lavas: 1) Fractional crystallization during igneous differentiation (e.g., Voegelin et al., 2014; Wille et al., 2018); 2) direct recycling of isotopically heterogeneous slab-derived Mo (e.g., Gaschnig et al., 2017; Casalini et al., 2019); 3) isotope fractionation of Mo during prograde subduction-related metamorphism (e.g., Freymuth et al., 2015; König et al., 2016; Chen et al., 2019). To untangle this controversy, Chapter 1 of this thesis presents the first study that applies a combined approach by analyzing the Mo isotopic composition of subduction input and output of the Tongan subduction zone together with subducted analogs from the Western Alps and Alpine Corsica. The analyzed metamorphic rocks potentially give complementary insights into the behavior of elements and their isotopes during prograde subduction metamorphism. The Tongan arc represents a suitable end member to study Mo recycling in intra-oceanic subduction zones because of the subduction of Mn-rich pelagic sediments (rich in Mo), one of the fastest convergence rates, coldest slab temperatures, and most depleted subarc mantle wedge worldwide. Pelagic sediments on the subducting SW-Pacific Plate dominate the Mo budget of the Tongan subduction zone with $\delta^{98/95}$Mo mostly lighter than the mantle signature. However, prominent loss of heavy Mo from sediments occurs early upon subduction as revealed by Mn-rich eclogite facies metapelites that indicate a residual isotopically light, and Mo-depleted subducted sedimentary unit before reaching subarc depths. Furthermore, non-subducted and eclogite facies AOC show (heavy) Mo-depletion patterns indicating a major control of seafloor alteration onto the Mo isotope signature and a possible loss of heavy Mo during early subduction. In sum, Mo loss and isotope fractionation occur mainly before and during early subduction in the forearc. Stable Mo hosts in the subducted slab, such as rutile (and possibly sulfides), that form early during subduction (rutile at around 30 km) are considered as the dominant hosts of subducted (light) Mo. However, due to the low solubility of rutile in aqueous fluids at subarc P-T conditions (Audétat and Keppler, 2005), no Mo-enriched subarc aqueous fluids are expected to be derived from an already Mo-depleted, isotopically light crust. This creates an “arc Mo-conundrum” as the devolatilization of the slab at subarc depths is not able to account for the enrichments of Tongan arc lavas via fluid-derived heavy Mo that contrasts with the lighter Mo isotope compositions of the slab. Therefore, alternative and multistage processes are required that recycle the serpentinized hanging wall mantle of the forearc, which is metasomatized by slab-derived heavy Mo-rich fluids during early subduction. These processes require mechanical transport of serpentinized mantle to subarc regions, where dehydration reactions eventually release previously incorporated heavy Mo and other fluid-mobile elements into the subarc mantle wedge. Geophysical data and geodynamic modeling indicate that this transport might be facilitated by subduction erosion and/or slab rollback. The recycling of the metasomatized forearc mantle to subarc regions is supported by positive covariations between Mo isotopes and fluid mobile elements, such as As, Sb, and Cs, that are released early during subduction. These sequences of processes can explain the Mo isotope variations observed at the Tongan subduction zone. It highlights the importance of the forearc mantle as a fluid mobile element (and volatile) carrier. This forearc mantle was conventionally thought to have only a minor influence on volcanic arc magma geochemistry as it is mechanically decoupled from the subducted slab.

## Chapter 2: Molybdenum isotopes in plume-influenced MORBs reveal recycling of ancient anoxic sediments

Previous studies suggested that subducted Phanerozoic oxidized sediments rich in e.g., $Fe^{3+}$, $Mn^{4+}$, and $SO_4^{2-}$ can efficiently buffer subduction zone redox conditions to high $fO_2$ (Ague et al., 2022 and references therein), which in turn increase the mobility of Mo (Bali et al., 2012;

Skora et al., 2017). Considering that under modern oxic settings the subducted slab in bulk (i.e. subducted sediments and AOC) is depleted in heavy Mo (Chapter 1), this supports the redox-dependent loss of (heavy) $Mo^{6+}$ during the subduction of oxic (sedimentary) lithologies into the mantle wedge (Bali et al., 2012; Skora et al., 2017; Chen et al., 2019; Chowdhury et al., 2022). This suggests that an isotopically light residual slab enters the deep mantle and can be potentially incorporated into plume-influenced rocks. Previous studies revealed an isotopically light signature in OIBs and continental basalts suggesting the incorporation of a devolatilized oceanic crust in their source (e.g., Gaschnig et al., 2021; Ma et al., 2022). Experimental studies suggest a decreased mobility of Mo in slab-derived fluids (such as aqueous fluids and hydrous melts) under more reducing conditions (when Mo is mainly present as $Mo^{4+}$ in the subducted slab) due to the increased compatibility of $Mo^{4+}$ in residual rutile and sulfide (Bali et al., 2012; Skora et al., 2017; Chowdhury et al., 2022). This leads to a minor net isotope fractionation of Mo during subduction, because of an insignificant loss of heavy $Mo^{6+}$, which in turn is less abundant in rocks that formed in reduced settings. This might have implications for the Mo cycle in subduction zone settings in the Precambrian, due to the prevailing anoxic deep ocean conditions, which have direct control over the slab redox budget (Evans, 2012). This in turn potentially has implications for the Mo isotope composition of recycled crustal components in the deep mantle, which can then eventually resurface through plume activity.

To test this hypothesis, Chapter 2 presents the Mo isotope composition of MORB lavas from the South-Mid Atlantic Ridge (S-MAR) that are influenced by the Shona and Discovery mantle plume, which carry the enriched mantle 1 (EM-1) signature. Previous studies based on radiogenic isotopes and stable S and Se isotopes suggested the contribution of Proterozoic anoxic sediments in their source (Douglass et al., 1999; Andres et al., 2002; Labidi et al., 2013; Yierpan et al., 2020). The lavas show covariations between radiogenic isotopes (Sr, Nd, Hf) and stable Mo, Se, and S isotopes. Heavier Mo isotopic compositions are preserved in the more enriched sources compared to the ambient depleted mantle, which cannot be explained by e.g., lower crustal recycling or mantle metasomatism. Modeling the Mo signature of the potential sedimentary end member that has fertilized the enriched mantle source suggests a sedimentary Mo concentration and isotopic composition close to the UCC composition. This is in line with Proterozoic pelagic anoxic sediments with lithogenic UCC-like Mo isotope compositions with a minor authigenic enrichment derived from heavy seawater Mo. The preservation of pre-subduction sediment signatures indicates that Mo was retained in the sedimentary unit supporting the immobile behavior of Mo during subduction, which in turn implies reducing conditions during subduction in the Proterozoic. Hence, Mo isotope fractionation between different terrestrial reservoirs likely depends on the slab redox budget, and therefore on the timing of subduction with regard to Earth's surface oxygenation.

## Chapter 3: Heavy Mo in the Pitcairn plume and global implications for the subduction cycle of anoxic sediments

In addition to the EM-1 end member, Earth's compositionally heterogeneous mantle can be mainly defined by a mixture of three additional end members: depleted mantle (DM), enriched mantle 2 (EM-2), and HIMU (high time-integrated $\mu = {}^{238}U/{}^{204}Pb$). For the generation of EM-1 signatures vastly different scenarios have been proposed, including different types of mantle metasomatism, recycling of subcontinental mantle, delamination of lower continental crust, and the recycling of different marine sediments with different recycling ages (Stracke, 2012 and references therein).

To further constrain the nature of the recycled components of EM-1, Mo isotope ratios of fresh hotspot-influenced basaltic glasses from Pitcairn Island were analyzed. These samples exhibit homogeneously heavier Mo isotope compositions than the depleted Pacific mantle and have high time-integrated ${}^{232}Th/{}^{238}U$, which can be attributed to the recycling of pelagic sediments that were deposited in a Proterozoic redox-stratified deep ocean. This model is in line with EM-1 influenced MORBs from the S-MAR (Chapter 2) indicating widespread chemical modification of Earth's two large low shear wave velocity provinces (LLSVPs) residing below Africa and the Pacific through the addition of reduced sediments. The preservation of pre-subduction signatures indicates that subduction recycling of certain redox-sensitive elements was inefficient in the Precambrian compared to the Phanerozoic. This can be linked with the widespread oxidation of global arc magmas only to have occurred after the Neoproterozoic Oxidation Event, in the case it requires an oxidized fluid from the slab (e.g., Stolper and Bucholz, 2019). Likely, the transition to a fully aerobic ocean during the Phanerozoic impacted the redox budget in subduction zones, thus affecting the mobility and recycling of redox-sensitive elements within convergent margin settings, where new continental crust is dominantly formed. This change in the composition and redox state of subducted material had likely an influence on the composition of the Precambrian continental crust, and therefore, the element budget of the ocean and the evolution of life itself.

## References

Aarons, S.M., Johnson, A.C., and Rader, S.T., 2021, Forming Earth's Continental Crust: A Nontraditional Stable Isotope Perspective: Elements, v. 17, p. 413–418, https://doi.org/10.2138/GSELEMENTS.17.6.413.

Ague, J.J., Tassara, S., Holycross, M.E., Li, J.-L., Cottrell, E., Schwarzenbach, E.M., Fassoulas, C., and John, T., 2022, Slab-derived devolatilization fluids oxidized by subducted metasedimentary rocks: Nature Geoscience 2022, p. 1–7, https://doi.org/10.1038/s41561-022-00904-7.

Allègre, C.J., 1987, Isotope geodynamics: Earth Planet. Sci. Lett., v. 86, p. 175–203, https://doi.org/10.1016/0012-821x(87)90220-2.

Andersen, M.B., Elliott, T., Freymuth, H., Sims, K.W.W., Niu, Y., and Kelley, K.A., 2015, The terrestrial uranium isotope cycle: Nature 2015 517:7534, v. 517, p. 356–359, https://doi.org/10.1038/nature14062.

Andres, M., Blichert-Toft, J., and Schilling, J.-G., 2002, Hafnium isotopes in basalts from the southern Mid-Atlantic Ridge from 40°S to 55°S: Discovery and Shona plume–ridge interactions and the role of recycled sediments: Geochemistry, Geophysics, Geosystems, v. 3, p. 1–25, https://doi.org/10.1029/2002GC000324.

Audétat, A., and Keppler, H., 2005, Solubility of rutile in subduction zone fluids, as determined by experiments in the hydrothermal diamond anvil cell: Earth and Planetary Science Letters, v. 232, p. 393–402, https://doi.org/10.1016/j.epsl.2005.01.028.

Bali, E., Keppler, H., and Audetat, A., 2012, The mobility of W and Mo in subduction zone fluids and the Mo-W-Th-U systematics of island arc magmas: Earth and Planetary Science Letters, v. 351–352, p. 195–207, https://doi.org/10.1016/j.epsl.2012.07.032.

Bebout, G.E., 2014, Chemical and Isotopic Cycling in Subduction Zones: Treatise on Geochemistry: Second Edition, v. 4, p. 703–747, https://doi.org/10.1016/B978-0-08-095975-7.00322-3.

Casalini, M., Avanzinelli, R., Tommasini, S., Elliott, T., and Conticelli, S., 2019, Ce/Mo and Molybdenum Isotope Systematics in Subduction-Related Orogenic Potassic Magmas of Central-Southern Italy: Geochemistry, Geophysics, Geosystems, v. 20, p. 2753–2768, https://doi.org/10.1029/2019GC008193.

Chen, S., Hin, R.C., John, T., Brooker, R., Bryan, B., Niu, Y., and Elliott, T., 2019, Molybdenum systematics of subducted crust record reactive fluid flow from underlying slab serpentine dehydration: Nature Communications, v. 10, https://doi.org/10.1038/s41467-019-12696-3.

Chowdhury, P., Dasgupta, R., Phelps, P.R., Costin, G., and Lee, C.T.A., 2022, Oxygen fugacity range of subducting crust inferred from fractionation of trace elements during fluid-present slab melting in the presence of anhydrite versus sulfide: Geochimica et Cosmochimica Acta, v. 325, p. 214–231, https://doi.org/10.1016/J.GCA.2022.02.030.

Donnelly, K.E., Goldstein, S.L., Langmuir, C.H., and Spiegelman, M., 2004, Origin of enriched ocean ridge basalts and implications for mantle dynamics: Earth and Planetary Science Letters, v. 226, p. 347–366, https://doi.org/10.1016/J.EPSL.2004.07.019.

Douglass, J., Schilling, J.-G., and Fontignie, D., 1999, Plume-ridge interactions of the Discovery and Shona mantle plumes with the southern Mid-Atlantic Ridge (40°-55°S): Journal of Geophysical Research: Solid Earth, v. 104, p. 2941–2962, https://doi.org/10.1029/98JB02642.

Elliott, T., 2003, Tracers of the slab: Geophysical Monograph-American Geophysical Union, v. 138, p. 23–46.

Evans, K.A., 2012, The redox budget of subduction zones: Earth-Science Reviews, v. 113, p. 11–32, https://doi.org/10.1016/J.EARSCIREV.2012.03.003.

Freymuth, H., Vils, F., Willbold, M., Taylor, R.N., and Elliott, T., 2015, Molybdenum mobility and isotopic fractionation during subduction at the Mariana arc: Earth and Planetary Science Letters, v. 432, p. 176–186, https://doi.org/10.1016/j.epsl.2015.10.006.

Gaschnig, R.M., Reinhard, C.T., Planavsky, N.J., Wang, X., Asael, D., and Chauvel, C., 2017, The Molybdenum Isotope System as a Tracer of Slab Input in Subduction Zones: An Example From Martinique, Lesser Antilles Arc: Geochemistry, Geophysics, Geosystems, v. 18, p. 4674–4689, https://doi.org/10.1002/2017GC007085.

Gaschnig, R.M., Reinhard, C.T., Planavsky, N.J., Wang, X., Asael, D., and Jackson, M.G., 2021, The impact of primary processes and secondary alteration on the stable isotope composition of ocean island basalts: Chemical Geology, v. 581, p. 120416, https://doi.org/10.1016/J.CHEMGEO.2021.120416.

Greber, N.D., Pettke, T., and Nägler, T.F., 2014, Magmatic–hydrothermal molybdenum isotope fractionation and its relevance to the igneous crustal signature: Lithos, v. 190–191, p. 104–110, https://doi.org/10.1016/J.LITHOS.2013.11.006.

Hawkesworth, C.J., Cawood, P.A., and Dhuime, B., 2020, The Evolution of the Continental Crust and the Onset of Plate Tectonics: Frontiers in Earth Science, v. 8, p. 326, https://doi.org/10.3389/FEART.2020.00326.

Hermann, J., and Rubatto, D., 2009, Accessory phase control on the trace element signature of sediment melts in subduction zones: Chemical Geology, v. 265, p. 512–526, https://doi.org/10.1016/J.CHEMGEO.2009.05.018.

Hermann, J., and Spandler, C.J., 2008, Sediment Melts at Sub-arc Depths: an Experimental Study: Journal of Petrology, v. 49, p. 717–740, https://doi.org/10.1093/PETROLOGY/EGM073.

Hermann, J., Spandler, C., Hack, A., and Korsakov, A. V., 2006, Aqueous fluids and hydrous melts in high-pressure and ultra-high pressure rocks: Implications for element transfer in subduction zones: Lithos, v. 92, p. 399–417, https://doi.org/10.1016/j.lithos.2006.03.055.

Hirschmann, M.M., and Stolper, E.M., 1996, A possible role for garnet pyroxenite in the origin of the “garnet signature” in MORB: Contributions to Mineralogy and Petrology, v. 124, p. 185–208, https://doi.org/10.1007/S004100050184.

Hofmann, A.W., 1997, Mantle geochemistry: the message from oceanic volcanism: Nature 1997 385:6613, v. 385, p. 219–229, https://doi.org/10.1038/385219a0.

Kendall, B., Dahl, T.W., and Anbar, A.D., 2017, Good Golly, Why Moly? The stable isotope geochemistry of molybdenum, in Non-Traditional Stable Isotopes, Walter de Gruyter GmbH, v. 82, p. 683–732, https://doi.org/10.2138/rmg.2017.82.16.

Keppler, H., 1996, Constraints from partitioning experiments on the composition of subduction-zone fluids: Nature 1996 380:6571, v. 380, p. 237–240, https://doi.org/10.1038/380237a0.

Kessel, R., Schmidt, M.W., Ulmer, P., and Pettke, T., 2005, Trace element signature of subduction-zone fluids, melts and supercritical liquids at 120–180 km depth: Nature 2005 437:7059, v. 437, p. 724–727, https://doi.org/10.1038/nature03971.

Klimm, K., Blundy, J.D., and Green, T.H., 2008, Trace Element Partitioning and Accessory Phase Saturation during H2O-Saturated Melting of Basalt with Implications for Subduction Zone Chemical Fluxes: Journal of Petrology, v. 49, p. 523–553, https://doi.org/10.1093/PETROLOGY/EGN001.

König, S., Wille, M., Voegelin, A., and Schoenberg, R., 2016, Molybdenum isotope systematics in subduction zones: Earth and Planetary Science Letters, v. 447, p. 95–102, https://doi.org/10.1016/j.epsl.2016.04.033.

Labidi, J., Cartigny, P., and Moreira, M., 2013, Non-chondritic sulphur isotope composition of the terrestrial mantle: Nature 2013 501:7466, v. 501, p. 208–211, https://doi.org/10.1038/nature12490.

Li, H., Hermann, J., and Zhang, L., 2022, Melting of subducted slab dictates trace element recycling in global arcs: Science Advances, v. 8, p. 2166, https://doi.org/10.1126/sciadv.abh2166.

Liu, H., Zartman, R.E., Ireland, T.R., and Sun, W. dong, 2019, Global atmospheric oxygen variations recorded by Th/U systematics of igneous rocks: Proceedings of the National Academy of Sciences of the United States of America, v. 116, p. 18854–18859, https://doi.org/10.1073/pnas.1902833116.

Ma, L., Xu, Y.G., Li, J., Chen, L.H., Liu, J.Q., Li, H.Y., Huang, X.L., Ma, Q., Hong, L.B., and Wang, Y., 2022, Molybdenum isotopic constraints on the origin of EM1-type continental intraplate basalts: Geochimica et Cosmochimica Acta, v. 317, p. 255–268, https://doi.org/10.1016/J.GCA.2021.11.013.

Mayer, A.J., and Wieser, M.E., 2013, The absolute isotopic composition and atomic weight of molybdenum in SRM 3134 using an isotopic double-spike: Journal of Analytical Atomic Spectrometry, v. 29, p. 85–94, https://doi.org/10.1039/C3JA50164G.

McCoy-West, A.J., Chowdhury, P., Burton, K.W., Sossi, P., Nowell, G.M., Fitton, J.G., Kerr, A.C., Cawood, P.A., and Williams, H.M., 2019, Extensive crustal extraction in Earth's early history inferred from molybdenum isotopes: Nature Geoscience, v. 12, p. 946–951, https://doi.org/10.1038/s41561-019-0451-2.

Miller, C.A., Peucker-Ehrenbrink, B., Walker, B.D., and Marcantonio, F., 2011, Re-assessing the surface cycling of molybdenum and rhenium: Geochimica et Cosmochimica Acta, v. 75, p. 7146–7179, https://doi.org/10.1016/J.GCA.2011.09.005.

Niu, Y., Regelous, M., Wendt, I.J., Batiza, R., and O'Hara, M.J., 2002, Geochemistry of near-EPR seamounts: importance of source vs. process and the origin of enriched mantle component: Earth and Planetary Science Letters, v. 199, p. 327–345, https://doi.org/10.1016/S0012-821X(02)00591-5.

Plank, T., Cooper, L.B., and Manning, C.E., 2009, Emerging geothermometers for estimating slab surface temperatures: Nature Geoscience 2009 2:9, v. 2, p. 611–615, https://doi.org/10.1038/ngeo614.

Plank, T., and Langmuir, C.H., 1993, Tracing trace elements from sediment input to volcanic output at subduction zones: Nature 1993 362:6422, v. 362, p. 739–743, https://doi.org/10.1038/362739a0.

Rudnick, R.L., and Gao, S., 2014, Composition of the Continental Crust, in Treatise on Geochemistry: Second Edition, Elsevier Inc., v. 4, p. 1–51, https://doi.org/10.1016/B978-0-08-095975-7.00301-6.

Salters, V.J.M., and Stracke, A., 2004, Composition of the depleted mantle: Geochemistry, Geophysics, Geosystems, v. 5, Q05B07. https://doi.org/10.1029/2003GC000597.

Skora, S., Freymuth, H., Blundy, J., Elliott, T., and Guillong, M., 2017, An experimental study of the behaviour of cerium/molybdenum ratios during subduction: Implications for tracing the slab component in the Lesser Antilles and Mariana Arc: Geochimica et Cosmochimica Acta, v. 212, p. 133–155, https://doi.org/10.1016/j.gca.2017.05.025.

Spandler, C., and Pirard, C., 2013, Element recycling from subducting slabs to arc crust: A review: Lithos, v. 170–171, p. 208–223, https://doi.org/10.1016/J.LITHOS.2013.02.016.

Stolper, D.A., and Bucholz, C.E., 2019, Neoproterozoic to early Phanerozoic rise in island arc redox state due to deep ocean oxygenation and increased marine sulfate levels: Proceedings of the National Academy of Sciences of the United States of America, v. 116, p. 8746–8755, https://doi.org/10.1073/pnas.182184711.

Stracke, A., 2012, Earth's heterogeneous mantle: A product of convection-driven interaction between crust and mantle: Chemical Geology, v. 330–331, p. 274–299, https://doi.org/10.1016/J.CHEMGEO.2012.08.007.

Tatsumi, Y., and Eggins, S., 1995, Subduction zone magmatism. Frontiers in Earth Sciences, Blackwell Science, Cambridge, Massachusetts.

Teng, F., Wang, S., and Moynier, F., 2019, Tracing the formation and differentiation of the Earth by non-traditional stable isotopes: Science China Earth Sciences 2019 62:11, v. 62, p. 1702–1715, https://doi.org/10.1007/S11430-019-9520-6.

Tissot, F.L.H., and Ibañez-Mejia, M., 2021, Unlocking the Single-Crystal Record of Heavy Stable Isotopes: Elements, v. 17, p. 389–394, https://doi.org/10.2138/GSELEMENTS.17.6.389.

Voegelin, A.R., Pettke, T., Greber, N.D., von Niederhäusern, B., and Nägler, T.F., 2014, Magma differentiation fractionates Mo isotope ratios: Evidence from the Kos Plateau Tuff (Aegean Arc): Lithos, v. 190–191, p. 440–448, https://doi.org/10.1016/j.lithos.2013.12.016.

Watkins, J.M., and Antonelli, M.A., 2021, Beyond Equilibrium: Kinetic Isotope Fractionation in High-Temperature Environments: Elements, v. 17, p. 383–388, https://doi.org/10.2138/GSELEMENTS.17.6.383.

Willbold, M., and Elliott, T., 2017, Molybdenum isotope variations in magmatic rocks: Chemical Geology, v. 449, p. 253–268, https://doi.org/10.1016/j.chemgeo.2016.12.011.

Willbold, M., and Stracke, A., 2006, Trace element composition of mantle end-members: Implications for recycling of oceanic and upper and lower continental crust: Geochemistry, Geophysics, Geosystems, v. 7, https://doi.org/10.1029/2005GC001005.

Wille, M., Nebel, O., Pettke, T., Vroon, P.Z., König, S., and Schoenberg, R., 2018, Molybdenum isotope variations in calc-alkaline lavas from the Banda arc, Indonesia: Assessing the effect of crystal fractionation in creating isotopically heavy continental crust: Chemical Geology, v. 485, p. 1–13, https://doi.org/10.1016/j.chemgeo.2018.02.037.

Yang, J., Barling, J., Siebert, C., Fietzke, J., Stephens, E., and Halliday, A.N., 2017, The molybdenum isotopic compositions of I-, S- and A-type granitic suites: Geochimica et Cosmochimica Acta, v. 205, p. 168–186, https://doi.org/10.1016/j.gca.2017.01.027.

Yierpan, A., König, S., Labidi, J., and Schoenberg, R., 2020, Recycled selenium in hot spot–influenced lavas records ocean-atmosphere oxygenation: Science Advances, v. 6, p. eabb6179, https://doi.org/10.1126/SCIADV.ABB6179.

Zerkle, A.L., 2018, Biogeodynamics: bridging the gap between surface and deep Earth processes: Philosophical Transactions of the Royal Society A: Mathematical, Physical and Engineering Sciences, v. 376, https://doi.org/10.1098/RSTA.2017.0401.

Zindler, A., and Hart, S., 1986, Chemical Geodynamics. Annual Review of Earth and Planetary Sciences, p. 493–571, https://doi.org/10.1146/annurev.ea.14.050186.002425.

# 1

# The Molybdenum isotope subduction recycling conundrum: A case study from the Tongan subduction zone, Western Alps and Alpine Corsica

**Manuscript published in Chemical Geology**

Ahmad Q., Wille M., König S., Rosca C., Hensel A., Pettke T., and Hermann J. (2021)

Chemical Geology, 576, 120231.

# Abstract

Molybdenum isotopes have emerged as novel tracers for high-temperature igneous and metamorphic processes. The debate remains to what extent different subducted slab lithologies, such as oceanic crust and marine sediments, contribute to the Mo isotope signature of arc magmas and, hence, exert different controls on the terrestrial Mo cycle. Here we investigate Mo isotope systematics from input to output at the Tongan subduction zone: Arc lavas from different Tongan islands, pelagic sediments and altered oceanic crust (AOC) samples from DSDP site 595/596 on the subducting Pacific plate. For complementary insights into the fate of Mo and its isotopic signatures during prograde subduction metamorphism, we also present data of metasediments and variably altered AOC-type eclogites from the Zermatt-Saas ophiolite, Switzerland and Italy, and the Schistes Lustrés Complex in Alpine Corsica.

Manganese oxide-rich pelagic sediments from DSDP site 595/596 show variable, depth-dependent Mo/Mn ratios and Mo isotope compositions controlled by diagenetic reactions. As subducted equivalents, Mn-rich eclogitic metapelites display lower Mo contents and $\delta^{98/95}$Mo ratios compared to their non-subducted protolith. This indicates a prominent loss of Mo along with isotope fractionation during early subduction metamorphism. In comparison to unaltered MORB, low-temperature seafloor alteration has shifted Mo/Ce and $\delta^{98/95}$Mo in studied AOC samples towards lower ratios, in the range of most mafic eclogites published so far. However, some mafic eclogites show even lower Mo/Ce and $\delta^{98/95}$Mo ratios compared to AOC, likely due to fluid-related Mo loss upon early subduction and preferential incorporation of light Mo into residual rutile.

Our data document a prominent loss of isotopically heavy Mo before and upon early subduction metamorphism at shallow depths in the forearc region. Moreover, when prograde rutile crystallizes at ~30 km depth, it fixes the largest fraction of Mo in the subducting material. This creates an “arc Mo-conundrum” as devolatilization of the slab at subarc depths is not able to account for the fluid-mobile Mo source responsible for observed higher Mo/Ce and $\delta^{98/95}$Mo in Tongan arc lavas compared to the mantle. As an alternative scenario, Mo mobilization by slab-derived aqueous fluids during the early stages of subduction into the forearc mantle produces serpentinites enriched in Mo with a possible heavy Mo isotopic signature. Mechanical transport and devolatilization of forearc serpentinites at subarc regions is a plausible alternative recycling process accounting for the observed Mo systematics in Tongan arc lavas. This is supported by positive covariations of Mo/Ce and $\delta^{98/95}$Mo with elements such as As, Sb, and Cs, which are thought to be mostly released from the subducting material during theearly stages of subduction. We propose that multi-stage recycling of metasomatized forearc mantle can be an important process in the recycling of Mo and possibly other elements.

# Introduction

Subduction zone magmatism at convergent margins is closely associated with the formation of continental crust. These settings are characterized by high mass fluxes between the oceanic crust and mantle, where slab-derived fluids (aqueous fluids or hydrous melts) facilitate the element transfer into the mantle wedge (Hermann et al., 2006). Molybdenum has been shown to be mobile in subduction zone fluids (König et al., 2010; König et al., 2008) and experimental constraints indicate that this mobility is controlled by the redox state and salinity of hydrous fluids involved (Bali et al., 2012; Skora et al., 2017). In recent years, stable Mo isotope ratios, expressed as $\delta^{98/95}\mathrm{Mo}_{\mathrm{SRM3134}}$ (herein: $\delta^{98/95}\mathrm{Mo}$), have been applied to investigate the slab-mantle wedge transport and ultimately the incorporation of this element into arc lavas (Casalini et al., 2019; Chen et al., 2019; Freymuth et al., 2016; Freymuth et al., 2015; Gaschnig et al., 2017; König et al., 2016; Villalobos-Orchard et al., 2020; Zhang et al., 2020).

Present-day aqueous Mo mobilization and transformation processes induce a large variability in Mo concentrations and isotope signatures in different marine sediments ($\delta^{98/95}\mathrm{Mo} = -0.9$ to +2.1‰; e.g., Barling et al., 2001; Freymuth et al., 2016, Freymuth et al., 2015; Gaschnig et al., 2017; Kendall et al., 2017; Siebert et al., 2003) compared to the homogeneous signature of the depleted mantle with $\delta^{98/95}\mathrm{Mo}$ of −0.2‰ (McCoy-West et al., 2019). Manganese-rich pelagic sediments constitute one isotopically light sedimentary end member; hence, they are of particular interest to study the element recycling in subduction zones with Mo isotopes. This lithology is highly enriched in Mo and has a light Mo isotopic composition, down to $\delta^{98/95}\mathrm{Mo} = -0.9$‰, due to isotopic fractionation during Mo scavenging from seawater ($\delta^{98/95}\mathrm{Mo} = +2.1$‰) onto Mn-oxides (Barling et al., 2001; Barling and Anbar, 2004; Siebert et al., 2003). Anoxic sediments, such as black shales primarily deposited at continental margins, also show a large Mo isotopic range, with generally higher $\delta^{98/95}\mathrm{Mo}$ than the depleted mantle and up to the seawater Mo isotopic composition (e.g., Barling et al., 2001; Gordon et al., 2009; Siebert et al., 2003). Thus, the recycling of isotopically variable Mo during sediment subduction can be potentially traced in arc volcanic rocks. Indeed, direct recycling of sediments during subduction has been suggested to affect the Mo isotope signature of arc lavas (Casalini et al., 2019; Freymuth et al., 2016; Gaschnig et al., 2017; Zhang et al., 2020). A sediment melt contribution of isotopically heavy black shales has been proposed to explain the heavy Mo isotopic composition of arc lavas from the Lesser Antilles arc (Freymuth et al., 2016).

Higher $\delta^{98/95}\mathrm{Mo}$ signatures compared to the depleted mantle have also been observed in arc lavas from the Mariana arc (Freymuth et al., 2015), Solomon arc (König et al., 2016) and Izu arc (Villalobos-Orchard et al., 2020), which are recognized as aqueous, slab-fluid dominated subduction zone settings.

These signatures were attributed to the formation of secondary minerals during subduction metamorphism, which preferentially incorporate light Mo, leading to an isotopically heavy slab-derived fluid that enters the mantle wedge. Chen et al. (2019) analyzed the Mo isotopic composition of a suite of blueschists and MORB-type eclogites and found overall lower $\delta^{98/95}$Mo, ranging from −0.13 to −0.99‰ compared to that of mantle/MORB values −0.16 to −0.22‰ (Bezard et al., 2016; Burkhardt et al., 2014; Greber et al., 2015; Liang et al., 2017; McCoy-West et al., 2019). This light bulk rock Mo isotopic composition goes along with lower Mo/Ce ratios indicating a loss of Mo from eclogites. Chen et al. (2019) could further show that rutile, a major host of Mo in eclogites, preferentially incorporates light Mo with individual rutile grains in eclogites showing even lower $\delta^{98/95}$Mo (−0.31 to −1.26‰) than the bulk eclogites. Consequently, these authors argue that rutile formation and concurrent loss of Mo by oxidized fluid flow through the oceanic crust, with the dominant aqueous fluid source being the underlying serpentinized mantle, produces the complementary heavy Mo isotopic signature in fluids entering the mantle wedge. Subsequent melting of residual rutile hosted in e.g. sedimentary mélange recycles the isotopically light Mo into the subarc mantle wedge, as proposed to explain the isotopically light arc lavas with $\delta^{98/95}$Mo down to −0.8‰ found in Cyprus and Papua New Guinea (PNG; König et al., 2016).

Fractional crystallization of hydrous minerals such as biotite and amphibole, which preferentially incorporate light Mo, has also been suggested to explain an isotopically heavy residual melt (Voegelin et al., 2014; Wille et al., 2018), while anhydrous differentiation has no significant effect onto the Mo isotope signature (Bezard et al., 2016; McCoy-West et al., 2019; Yang et al., 2015). This commonly suggests that the rather large $\delta^{98/95}$Mo heterogeneity of primitive arc lavas (i.e. with >5 wt% MgO) comprises the sum of the Mo isotope signature of the subducted lithologies plus intrinsic processes (i.e. subduction metamorphism) that influence the mantle Mo budget and its isotopic composition.

To better constrain to what extent different subducted lithologies may contribute to the Mo isotope signature of arc lavas, we investigated the Mo isotope systematics at the Tongan subduction zone (Fig. 1). The Tongan arc represents a valuable end member to study Mo recycling in intra-oceanic subduction zones because of Mn-rich pelagic sediment subduction, one of the fastest convergence rates, coldest slab temperatures, and most depleted subarc mantle wedges worldwide (e.g., Bevis et al., 1995; Menard et al., 1987; Plank, 2005; Syracuse et al., 2010). Samples include pelagic clays from the Deep Sea Drilling Project (DSDP) site 595/596 (~5600–5700 m below sea level), which are compared with subducted analogs comprising Mn-rich pelitic metasediments from Zermatt-Saas ophiolite and Lago di Cignana in the Western Alps, and the Schistes Lustrés Complex in Alpine Corsica. Altered oceanic crust (AOC) samples from the same DSDP site are compared with exhumed

AOC-type eclogites from Zermatt-Saas ophiolite and Tongan arc lavas. Analyzed exhumed metamorphic rocks experienced a wide range of peak metamorphic pressure and temperature conditions (Fig. 2) and offer insight into the nature of Mo mobility and isotope fractionation during subduction.

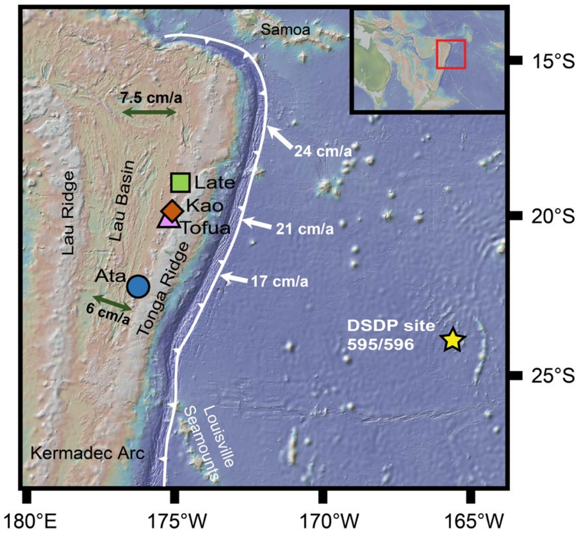

***Figure 1.*** *Map showing investigated Tongan arc islands of Late, Kao, Tofua and Ata and the DSDP site 595/596 together with convergence and spreading rates from Bevis et al. (1995). Figure made with GeoMapApp (www.geomapapp.org).*

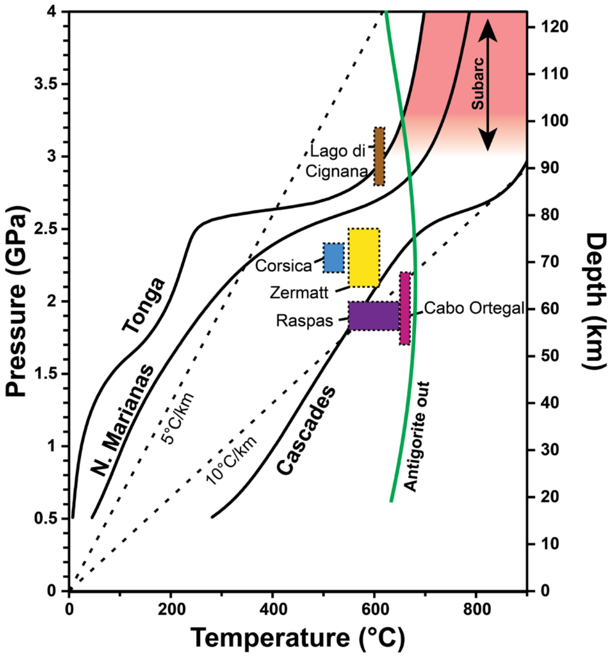

***Figure 2.*** *Pressure-temperature diagram displaying estimated peak-metamorphic conditions of studied metasediments and AOC-type eclogites from Zermatt, Lago di Cignana, and Corsica and corresponding approximate depth of subduction. For comparison, peak P-T conditions of blueschists and MORB-type eclogites from Cabo Ortegal and Raspas are displayed (Chen et al., 2019, and references therein). The stability of antigorite is shown for reference (Ulmer and Trommsdorff, 1995) together with modeled P-T paths of the slab surface of Tonga (D80 model of Syracuse et al. (2010)). Models of North Marianas and Cascades (Syracuse et al., 2010) exemplify intermediate and hot subduction zones, respectively.*

## Geological setting and sample material

### Tongan arc and DSDP site 595/596

Molybdenum isotope analyses were performed on a subset of 27 arc lavas (basalts to basaltic andesites), from a larger sample set collected on the uninhabited Tongan volcanic islands of Late, Tofua, Kao, and Ata in May 2017. The ~1500 km Tongan island arc is situated along a convergent margin in the southwest Pacific Ocean and is separated from the Kermadec arc to the south by the Louisville seamount chain (LSC) and to the north by the Vitiaz trench. The main Tongan arc formed by the subduction of the Jurassic-Cretaceous Pacific Plate beneath the Australian Plate since the Oligocene (e.g., Turner et al., 1997), a common feature in the evolution of many island arcs in the SW Pacific plate border region (e.g., Schuth et al., 2011). There is a northwards increase in convergence and backarc spreading rates along the arc (Fig. 1; Bevis et al., 1995), resulting in increasing relative mantle depletion northwards (Escrig et al., 2009; Ewart et al., 1998). High convergence rates and the subduction of old oceanic lithosphere led to one of the coldest subduction zones (e.g., Wei et al., 2017). Pleistocene to recent arc volcanic rocks of the Tongan islands are mainly of tholeiitic and basaltic andesite composition with minor occurrences of andesites and dacites (Caulfield et al., 2012, and references therein).

In addition to the arc lavas, 24 sample cuts (14 sediment samples and 10 AOC samples) covering the entire sampling depth of the DSDP site 595/596 core (~120 m below seafloor) were analyzed. It has been proposed that the overall subduction input into the Tongan mantle source consists mainly of AOC- and sediment-derived aqueous fluid and a hydrous sediment melt, while in the southern part additional contributions of volcanoclastic sediments from the LSC occur (Escrig et al., 2009). The sediment layer from the DSDP sites 595/596 has a thickness of only ~70 m. It consists of pelagic clays rich in ferromanganese oxides, with biogenic silica and porcellanite-rich layers in the bottom overlying N-MORB type AOC (Menard et al., 1987; Zhou and Kyte, 1992). The alteration of the basaltic crust corresponds to the lower temperature oxidation stage 5 of Johnson and Hall (1978) forming titanomaghemite from titanomagnetite, and the subsequent formation of alteration minerals like Fe-oxyhydroxides (Menard et al., 1987). The alteration is expressed by carbonate veins formed at low temperature (13–23 °C) consisting of Fe-oxyhydroxides and in part smectite (Gillis and Coogan, 2011; Menard et al., 1987). Due to the remoteness from continental shelf areas, pelagic clays, instead of terrigenous sediments, dominate the sedimentary subduction input (Menard et al., 1987). The absence of an accretionary wedge at the trench shows that the sediment is not physically eroded during subduction (Ballance et al., 1989; Clift and Vannucchi, 2004). Furthermore, the Tongan arc exhibits an extremely depleted mantle wedge signature in comparison to other arcs (e.g., based on relative high Sm/La ratios observed in arc lavas; Plank, 2005) invoking the possibility that already minor contributions of slab-derived, incompatible elements can be traced in the composition of arc magmas. Also, Leeman et al. (2017) argued that melt production in the Tongan arc is proportional to the overall fluid flux beneath the arc, which explains the depleted nature of the subarc setting, especially at Tofua where the highest slab-derived aqueous fluid flux within the arc is observed (e.g., Caulfield et al., 2012).

## Western Alps & Corsica

A total of 9 exhumed metasedimentary rocks from the Zermatt-Saas Unit (Southern Switzerland), Lago di Cignana (Italy), Alpine Corsica (France), and 4 AOC-type eclogites from Pfulwe (Zermatt, Switzerland) were analyzed (Table 1). These metamorphic rocks represent pelagic sediments and mafic oceanic crust, which attained variable peak P-T conditions upon convergence between Europe and Adria. The high-pressure Zermatt-Saas zone is a sequence of Mesozoic Tethys oceanic crust, which was subducted during early Alpine convergence. Peak P-T conditions for meta-AOC in the Pfulwe area and metasediments from the Trockener Steg area reached metamorphic conditions of 2.3 ± 0.2 GPa and 580 ± 30 °C (Angiboust et al., 2009). Samples PF18-25a and PF18-25c derive from a texturally preserved meta-pillow (PF18-25a: pillow core; PF18-25c: altered pillow rim) even though it experienced eclogite-facies metamorphism (Fig. S-1a). Samples PF18-20 (glaucophane-chloritoid eclogite; weakly altered AOC) and PF18-26 (chlorite-glaucophane-talc eclogite; strongly altered AOC) complete the metabasalt collection (Fig. S-1b). Further to the south, there is a small slice of the Saas-Zermatt unit with higher metamorphic conditions, the ultra-high pressure Lago di Cignana unit (Northern Italy). It comprises eclogites that derive from altered basalts, minor metagabbros, and a sedimentary cover with metapelites, calcschists, and quartzites that locally contain Mn-rich layers. Peak metamorphic conditions were 2.8–3.2 GPa and 600–620 °C (Groppo et al., 2009; Reinecke, 1991). The Schistes Lustrés complex (Alpine Corsica, France) represents the Ligurian part of the Jurassic western Tethys with meta-ophiolites and their metasedimentary cover rocks including turbidites. Peak conditions reached 2.3 ± 0.1 GPa and 520 ± 20 °C (Vitale-Brovarone et al., 2011).

***Table 1.*** *Sample location and mineralogy and peak P-T conditions of studied metamorphic rocks. See text for references.*

| **Sample** | **Rock type** | **Mineralogy** | **P (GPa)** | **T (°C)** |
|---|---|---|---|---|
| *Pfulwe, Zermatt* | | | | |
| PF18-20 | AOC-type eclogite | Glaucophane, Garnet, Epidote, Chlorite, Chloritoid, Paragonite, Rutile, Amphiboles | 2.3 ± 0.2 | 580 ± 30 |
| PF18-26 | AOC-type eclogite | Chlorite, Glaucophane, Garnet, Talc, Paragonite, Chloritoid, Epidote, Rutile ± Sulfides | 2.3 ± 0.2 | 580 ± 30 |
| PF18-25a | AOC-type eclogite | Omphacite, Amphiboles, Paragonite, Garnet, Glaucophane, Epidote, Carbonate, Rutile | 2.3 ± 0.2 | 580 ± 30 |
| PF18-25c | AOC-type eclogite | Epidote, Quartz, Garnet, Rutile, Apatite, Paragonite ± Sulfides | 2.3 ± 0.2 | 580 ± 30 |
| *Trockener Steg, Zermatt* | | | | |
| Z16TB31a | Grt-schist (clastic metasediment) | Quartz, White Mica, Zoisite, Garnet, Rutile ± Pyrite, Graphite | 2.3 ± 0.2 | 580 ± 30 |
| Z16TB31b | Grt-schist (clastic metasediment) | Quartz, White Mica, Zoisite, Garnet, Rutile ± Pyrite, Graphite | 2.3 ± 0.2 | 580 ± 30 |
| Z18TB20 | Grt-schist (clastic metasediment) | Quartz, White Mica, Zoisite, Tourmaline, Amphiboles, Garnet, Rutile ± Carbonate | 2.3 ± 0.2 | 580 ± 30 |
| *Lago di Cignana* | | | | |
| C13a | Mn-rich pelagic metasediment | Garnet, Omphacite, Quartz, Clinozoisite, Amphiboles, Epidote, Rutile ± Sulfides, Titanite | 3.0 ± 0.2 | 610 ± 10 |
| C13b | Mn-rich pelagic metasediment | Garnet, Omphacite, Quartz, Clinozoisite, Amphiboles, Epidote, Rutile ± Sulfides, Titanite | 3.0 ± 0.2 | 610 ± 10 |
| C11 | Mn-rich pelagic metasediment | Quartz, Garnet, White Mica, Piemontite, Fe-Mn-oxides, Tourmaline ± Rutile | 3.0 ± 0.2 | 610 ± 10 |
| *Schistes Lustrés Complex, Corsica* | | | | |
| COS 3 | Mn-rich pelagic metasediment | Quartz, Piemontite, White Mica, Fe-Mn-oxides | 2.3 ± 0.1 | 520 ± 20 |
| COS 2 | Mn-rich pelagic metasediment | Quartz, Garnet, White Mica, Rutile, Fe-Mn-oxides, Chlorite ± Graphite, Carbonate | 2.3 ± 0.1 | 520 ± 20 |
| COS 7 | Clastic metasediment | Quartz, Lawsonite, White Mica, Chlorite, Graphite ± Fe-oxides, Titanite, Sulfides | 2.3 ± 0.1 | 520 ± 20 |

# Analytical methods

## Bulk rock major oxide and trace element analysis

### Tongan arc lavas, sediments and oceanic crust (DSDP site 595/596)

Major and trace element investigations (preparations and measurements) of Tongan arc lavas, sediments and oceanic crust obtained from DSDP site 595/596 were performed at the Isotope Geochemistry laboratory, University of Tübingen. For major oxide composition determinations, fused beads were prepared using 1.5 g of dried and homogenized sample powder mixed with 7.5 g MERCK Spectromelt A12. Melting was conducted using an Oxiflux system from CBR analytical service reaching up to 1200 °C. Major oxide analyses were conducted using a Bruker AXS S4 Pioneer XRF device (Rh-tube at 4 kW) with 32 standardized samples. Analytical error and detection limits vary between elements and depend on sample composition. The composition of internal standards used here are compared to those of Govindaraju (1989). Absolute uncertainties are <0.250% for $SiO_2$ and $Al_2O_3$, <0.066% for $TiO_2$, $Na_2O$, MgO, MnO, CaO, and $Fe_2O_3$, while those for $P_2O_5$ are <0.009%.

For trace element analyses, the procedure as described in detail in Albut et al. (2018) was followed. In brief, ca. 30 mg of homogenized sample powders were digested either in bombs (arc lavas), or screw-top Savillex™ beakers (pelagic clays and AOC from the DSDP site 595/596) with single distilled HF-$HNO_3$ (3:1) mix in a total volume of 3 ml acid for 3 days at 100 °C, accompanied by daily ultrasonication. After gentle evaporation at 90 °C, the samples were again dissolved in 3.5 ml 6 M HCl and cooked for two more days at 120 °C to allow disintegration of fluorides until a particle free solution was obtained. Finally, the digested sample was converted 2 times to nitrates using 3 M $HNO_3$ followed by gentle evaporation. In preparation for analyses, all sample unknowns were gravimetrically dissolved in 2% $HNO_3$ stock solutions with an aimed dilution factor of 1 k. The final measurement dilution consisted of ~1 g from that stock solution and ~ 9 g of an internal standard solution as detailed below, to yield a sample dilution factor of ~10 k. Measurements were conducted via solution quadrupole ICP-MS using a ThermoFisher Scientific iCap-Qc and following the protocols described by Eggins et al. (1997) with slight modifications after Albut et al. (2018). Main steps include the addition of an internal standard (solution enriched in Li, In, Re and Bi) to all sample unknowns and rock reference materials which cover the full mass-range of analyzed elements. This artificial enrichment is used for instrumental mass-drift correction. Three different dilutions (10 k, 20 k, and 40 k) of the USGS W-2a reference material were used for calibration. Dimer, oxide/hydroxide interferences were corrected after Ulrich et al. (2010). To account for potential drift over the course of an entire measurement, an in-house prepared monitoring solution, consisting of digested and diluted

AGV-2 and W-2a rock reference materials, was measured six times interleaved between sample unknowns. Certified rock reference materials BIR-1a and BHVO-2 prepared in the same manner as sample unknowns were used as external quality controls. Measurement precision assessed by single relative standard deviations (RSD) of the mean of multiple measurements were typically <2%. Measurement accuracy was assessed by comparing the obtained element concentrations discussed in this study with the values of Babechuk et al. (2009) as presented in Table S-3, S-4. Obtained concentrations for Co, Ni, Cu, Ce, Ba, La, Sm, of BHVO-2, BIR-1a and W-2a match those of Babechuk et al. (2009) within uncertainties <2% (RSD). Slightly inferior reproducibilities (1–15% RSD) were obtained for Cs, Pb, Sb and Th and 1–32% for As. The poorer reproducibilities for Sb and As can be attributed to either very low concentration or known heterogeneity for this generation of USGS reference materials (e.g., Weis et al., 2006).

### Metamorphic rocks

Metasediment and eclogite samples were cut with a metal saw and polished with a diamond grinding wheel to eliminate contamination from the metal saw. Further crushing was performed with a hydraulic press, which was covered with aramid fabric to protect sample against contamination. After using an agate planetary ball mill to obtain homogenized sample powder, a powder aliquot was further wet-milled again in agate, dried, and pressed to powder pellets for bulk-rock LA-ICP-MS analysis following analytical protocols presented in Peters and Pettke (2017) and Garbe-Schönberg and Müller (2014). For major and trace element analysis a GeoLas-Pro 193 nm ArF Excimer laser system (Lambda Physik) combined with an Elan DRC-e quadrupole mass spectrometer (Perkin Elmer) was used, located at the Institute of Geological Sciences, University of Bern. Optimization of the instrument was performed following previously published protocols (Peters and Pettke, 2017; Pettke et al., 2012), using GSD-1G as the external standard. Measurements of control standard OKUM Komatiite (International Association of Geoanalysts) monitored measurement quality and reproducibility.

Before measurement, the sample spot was ablated with a diameter of 160 μm to remove surface contamination (pre-ablation). The laser was set to a pulse frequency of 8 Hz and 8 J/cm$^2$ energy density on the sample surface with a 120 μm diameter. In total, 6 spots per sample were measured and the average was taken for the sample element concentrations (with 1 SD uncertainty on external reproducibility; Table S-4). Data reduction was done using the open software SILLS (Guillong et al., 2008), with rigorous limits of detection calculation (Pettke et al., 2012).

## Molybdenum purification and isotope analysis

Homogenized powder aliquots equivalent to 25–100 ng Mo (depending on Mo concentration of sample) were spiked with a purified $^{97}$Mo-$^{100}$Mo double isotope tracer solution (Mo proportion of 1:1 spike to sample ratio). All spiked samples were then digested in a single-distilled concentrated HF-$HNO_3$ mixture (3:1) and re-dissolved in 6 M HCl for several days. The latter step was usually repeated to minimize the amount of fluorides. Remaining graphite in metasediment samples was physically removed by centrifuging before chemical separation. Chemical separation of Mo was achieved by applying anion- and cation-exchange chromatography following the steps reported by Wille et al. (2013). Ultimately, all samples were dissolved in 0.5 M $HNO_3$ for analyses conducted at the Institute of Geological Sciences, University of Bern using a ThermoFisher Scientific NeptunePlus MC-ICP-MS in low resolution mode. Sample-introduction was facilitated by a Cetac ARIDUS II desolvating nebulizer with an uptake rate of 140 - 200 $\mu l \cdot min^{-1}$. Signals of 6 Mo isotopes ($^{94}$Mo, $^{95}$Mo, $^{96}$Mo, $^{97}$Mo, $^{98}$Mo and $^{100}$Mo) were measured simultaneously with interference monitors on $^{99}$Ru and $^{101}$Ru to allow correction of $^{98}$Ru on $^{98}$Mo and $^{100}$Ru on $^{100}$Mo. Resistors of $10^{-11}\Omega$ were used to analyze the signals of all isotopes except $^{101}$Ru, which was measured using a $10^{-12}\Omega$ resistor. Interference corrected $\delta^{98/95}$Mo values based on $^{99}$Ru and $^{101}$Ru correction were compared and discarded if differences were too large (>0.03‰). Background correction was applied by averaging background intensities on pure 0.5 M $HNO_3$ carrier solution that was measured on-peak before and after every sample analysis. Background and sample measurement consisted of 30 and 80 cycles, respectively, with a signal integration time of 4.194 s for each cycle. Our double spike correction method is based on an iterative calculation procedure reported previously (Siebert et al., 2001). Procedural blanks were generally <0.7 ng Mo. Molybdenum isotope ratios are reported as parts per thousand deviation of $^{98}$Mo/$^{95}$Mo of the sample relative to NIST SRM 3134 (Goldberg et al., 2013; Greber et al., 2012) with an interference correction based on $^{99}$Ru. Repeated measurements of the in-house J&M standard solution lot 602332B (Siebert et al., 2001) gave an isotopic difference of 0.271 ± 0.032‰ $\delta^{98/95}$Mo (2SD, n = 56) relative to NIST SRM 3134 (Goldberg et al., 2013), in agreement with Greber et al. (2012). Analyses of the individually digested AGV-2, BHVO-2 and W-2a whole-rock reference materials yielded a $\delta^{98/95}$Mo of −0.19 ± 0.04‰ (2SD, n = 6), −0.08 ± 0.05‰ (2SD, n = 7) and −0.06 ± 0.04‰ (2SD, n = 6), within uncertainty to that determined by Willbold et al. (2016), Burkhardt et al. (2014), and Zhao et al. (2016). Analyses of NOD-A-1 and NOD-P-1 Mn-nodule reference materials (same digested aliquot but individual chemical separation runs) yielded a $\delta^{98/95}$Mo of −0.63 ± 0.05‰ (2SD, n = 2) and −0.87 ± 0.02‰ (2SD, n = 3), within uncertainty to that determined by Asael et al. (2013). Individual measurements of geological reference materials can be found in Table S-1. We consider ±0.05‰ the long-term 2 SD reproducibility of the sample measurements as determined by the measurements of BHVO-2. This is a conservative estimate, as heterogeneity has been reported for Mo isotope ratios and overall concentration in BHVO-2 (e.g., Burkhardt et al., 2014; Willbold et al., 2016). Accurate Mo concentrations were obtained by means of inverse isotope dilution method from the double spike deconvolution (Table 2).

***Table 2.*** *Molybdenum concentrations and isotope ratios together with selected element concentrations and ratios of studied samples. 2SE = 2σ standard error.*

| Sample | Type | $\delta^{98/95}$Mo (‰) | 2 SE (‰) | Mo (µg/g) | $SiO_2$ (wt%) | MgO (wt%) | Ce (µg/g) | Mo/Ce | Ba/Th |
|---|---|---|---|---|---|---|---|---|---|
| *DSDP site 595/596* | | | | | | | | | |
| 595A_1 | Pelagic clay | −0.470 | 0.018 | 42 | 44.3 | 2.74 | 75.2 | 0.559 | – |
| 595A_2A | Pelagic clay | −0.330 | 0.021 | 44.8 | 39.3 | 2.6 | 83.4 | 0.538 | – |
| 595A_3 | Pelagic clay | −0.091 | 0.017 | 55.9 | 42.5 | 2.04 | 70.6 | 0.791 | – |
| 595A_4 | Pelagic clay | −0.219 | 0.019 | 103 | 36.4 | 2.91 | 408 | 0.253 | – |
| 595A_5 | Pelagic clay | −0.274 | 0.016 | 97.1 | 37.8 | 3.12 | 582 | 0.167 | – |
| 595A_6 | Pelagic clay | −0.164 | 0.016 | 69.6 | 38.7 | 2.82 | 507 | 0.137 | – |
| 595A_7 | Pelagic clay | 0.161 | 0.016 | 55.7 | 44.9 | 3 | 336 | 0.166 | – |
| 595A_8 | Pelagic clay | −0.053 | 0.016 | 34.5 | 43.3 | 3.1 | 300 | 0.115 | – |
| 595A_9 | Pelagic clay | −0.030 | 0.014 | 38.7 | 44.9 | 3.15 | 309 | 0.125 | – |
| 595A_10 | Pelagic clay | −0.107 | 0.015 | 31 | 45.4 | 3.25 | 278 | 0.112 | – |
| 595A_11 | Porcellanite-rich pelagic clay | 0.014 | 0.016 | 7.36 | 82.4 | 1.05 | 40.4 | 0.182 | – |
| 595A_12 | Porcellanite-rich pelagic clay | 0.033 | 0.02 | 6.31 | 69.3 | 1.18 | 41.5 | 0.152 | – |
| 595A_13 | Porcellanite-rich pelagic clay | 0.192 | 0.015 | 4 | 83.9 | 0.694 | 22.9 | 0.175 | – |
| 595A_16 | Porcellanite-rich pelagic clay | 0.072 | 0.018 | 7.11 | 76 | 1.18 | 64.6 | 0.11 | – |
| 595A_18 | Altered basalt | −0.685 | 0.02 | 0.186 | – | 5.76 | 9.41 | 0.02 | – |
| 595A_19 | Altered basalt | −0.494 | 0.016 | 0.154 | – | 6.16 | 9.22 | 0.017 | – |
| 595B_21 | Altered basalt | −0.316 | 0.015 | 0.515 | – | 5.53 | 17.7 | 0.029 | – |
| | | −0.381 | 0.016 | | | | | | |
| 595A_23 | Altered basalt | −0.278 | 0.013 | 0.352 | – | – | 17.1 | 0.021 | – |
| | | −0.257 | 0.017 | | | | | | |
| 595A_24 | Altered basalt | −0.691 | 0.017 | 0.217 | – | 5.16 | 17.2 | 0.013 | – |
| 595B_25 | Altered basalt | −0.571 | 0.014 | 0.327 | – | – | 18.1 | 0.018 | – |
| | | −0.565 | 0.016 | | | | | | |

| | | | | | | | | | |
|---|---|---|---|---|---|---|---|---|---|
| 595B_28 | Altered basalt | −0.657 | 0.019 | 0.298 | – | – | 18.7 | 0.016 | – |
| | | −0.577 | 0.012 | | | | | | |
| 595B_31 | Altered basalt | −0.597 | 0.015 | 0.187 | – | – | 17.6 | 0.011 | – |
| 595B_34 | Altered basalt | −0.314 | 0.016 | 0.316 | – | 4.55 | 19.9 | 0.016 | – |
| 595B_37 | Altered basalt | −0.432 | 0.015 | 0.161 | – | 6.09 | 12 | 0.013 | – |
| | | −0.424 | 0.017 | | | | | | |
| *Pfulwe, Zermatt* | | | | | | | | | |
| PF18-20 | AOC-type eclogite | −0.742 | 0.019 | 0.148 | 53.2 | 11.5 | 13.7 | 0.011 | – |
| PF18-26 | AOC-type eclogite | −0.825 | 0.014 | 0.293 | 40.1 | 15.8 | 26.9 | 0.011 | – |
| PF18-25a | AOC-type eclogite | −0.919 | 0.018 | 0.0382 | 53.7 | 4.17 | 46.3 | 0.0008 | – |
| PF18-25c | AOC-type eclogite | −1.012 | 0.017 | 0.161 | 46.6 | 0.776 | 51.7 | 0.003 | – |
| *Trockener Steg, Zermatt* | | | | | | | | | |
| Z16TB31a | Grt-schist (clastic metasediment) | −0.149 | 0.014 | 0.635 | 66.7 | 1.79 | 99.7 | 0.006 | – |
| Z16TB31b | Grt-schist (clastic metasediment) | −0.142 | 0.014 | 0.735 | 67.8 | 1.61 | 115 | 0.006 | – |
| Z18TB20 | Grt-schist (clastic metasediment) | −0.634 | 0.017 | 0.97 | 55.5 | 3.04 | 50.1 | 0.019 | – |
| *Lago di Cignana* | | | | | | | | | |
| C13a | Mn-rich pelagic metasediment | −1.456 | 0.017 | 0.393 | 76.6 | 1.33 | 32.2 | 0.012 | – |
| C13b | Mn-rich pelagic metasediment | −0.256 | 0.021 | 0.0288 | 78.8 | 1.97 | 41.1 | 0.0007 | – |
| C11 | Mn-rich pelagic metasediment | −1.500 | 0.018 | 0.0768 | 84.7 | 1.2 | 27.5 | 0.003 | – |
| *Schistes Lustrés Complex, Corsica* | | | | | | | | | |
| COS3 | Mn-rich pelagic metasediment | −0.546 | 0.024 | 0.0145 | 83.6 | 1.06 | 30.8 | 0.0005 | – |
| COS2 | Mn-rich pelagic metasediment | −0.612 | 0.015 | 0.0609 | 81.5 | 1.33 | 36.4 | 0.002 | – |
| COS7 | Clastic metasediment | −0.445 | 0.019 | 0.105 | 62.5 | 2.64 | 75.4 | 0.001 | – |
| *Ata, Tonga* | | | | | | | | | |
| T28A1 | Basalt | −0.099 | 0.013 | 0.672 | 50.5 | 7.18 | 6.33 | 0.106 | 349 |
| | | −0.089 | 0.017 | | | | | | |
| | | −0.073 | 0.015 | | | | | | |
| T29A2 | Basalt | −0.218 | 0.021 | 0.594 | 50.5 | 6.61 | 8.25 | 0.072 | 364 |
| T30A3 | Basaltic andesite | −0.161 | 0.013 | 0.677 | 52.7 | 4.97 | 7.59 | 0.089 | 495 |
| | | −0.149 | 0.016 | | | | | | |
| | | −0.140 | 0.017 | | | | | | |

| | | | | | | | | | |
|---|---|---|---|---|---|---|---|---|---|
| T32A5 | Basalt | −0.157 | 0.012 | 0.482 | 50.7 | 7.36 | 6.77 | 0.071 | 411 |
| | | −0.160 | 0.017 | | | | | | |
| T33A6 | Basalt | −0.183 | 0.017 | 0.75 | 50.3 | 7.2 | 6.81 | 0.11 | 450 |
| T35A8-2 | Basalt | −0.209 | 0.016 | 0.606 | 50 | 5.97 | 8.5 | 0.071 | 375 |
| T36A9 | Basalt | −0.213 | 0.021 | 0.711 | 50 | 6.49 | 8.42 | 0.084 | 388 |
| T37A10 | Basalt | −0.213 | 0.02 | 0.593 | 50.1 | 6.64 | 8.23 | 0.072 | 365 |
| T38A11 | Basalt | −0.329 | 0.018 | 0.673 | 50.7 | 6.23 | 8.66 | 0.078 | 395 |
| | | −0.235 | 0.02 | | | | | | |
| | | −0.219 | 0.016 | | | | | | |
| T39A12 | Basalt | −0.194 | 0.013 | 0.53 | 51 | 6.19 | 7.98 | 0.066 | 431 |
| | | −0.192 | 0.016 | | | | | | |
| | | −0.260 | 0.015 | | | | | | |
| T40A13 | Basalt | −0.195 | 0.015 | 0.606 | 51 | 6.13 | 7.99 | 0.076 | 434 |
| T41A14 | Basalt | −0.178 | 0.018 | 0.643 | 51.6 | 5.86 | 8.11 | 0.079 | 474 |
| T42A15 | Basalt | −0.161 | 0.017 | 0.701 | 51.7 | 5.89 | 8.53 | 0.082 | 416 |
| *Kao, Tonga* | | | | | | | | | |
| T15K1 | Basaltic andesite | −0.059 | 0.015 | 1.06 | 53.3 | 5.6 | 5.83 | 0.181 | 621 |
| | | −0.042 | 0.015 | | | | | | |
| T16K2 | Basaltic andesite | −0.111 | 0.014 | 0.972 | 53.4 | 5.44 | 6.57 | 0.148 | 590 |
| | | −0.081 | 0.018 | | | | | | |
| T17K3 | Basaltic andesite | −0.112 | 0.013 | 0.971 | 53.5 | 5.46 | 6.47 | 0.15 | 598 |
| | | −0.048 | 0.017 | | | | | | |
| | | −0.116 | 0.018 | | | | | | |
| *Late, Tonga* | | | | | | | | | |
| T21L2 | Basaltic andesite | −0.136 | 0.015 | 0.813 | 53.5 | 4.43 | 4.57 | 0.178 | 648 |
| | | −0.129 | 0.016 | | | | | | |
| | | −0.188 | 0.02 | | | | | | |
| T23L4 | Basaltic andesite | −0.156 | 0.014 | 1.12 | 56.2 | 3.3 | 6.65 | 0.168 | 617 |
| | | −0.114 | 0.021 | | | | | | |
| T25L6 | Basaltic andesite | −0.155 | 0.014 | 0.817 | 53.5 | 4.41 | 4.58 | 0.178 | 603 |
| | | −0.090 | 0.016 | | | | | | |
| | | −0.144 | 0.014 | | | | | | |

| | | | | | | | | | |
|---|---|---|---|---|---|---|---|---|---|
| T26L7 | Basaltic andesite | −0.099 | 0.013 | 0.796 | 53.4 | 4.24 | 4.85 | 0.164 | 589 |
| | | −0.097 | 0.018 | | | | | | |
| | | −0.124 | 0.015 | | | | | | |
| T27L8 | Basaltic andesite | −0.142 | 0.014 | 1.16 | 56.3 | 3.34 | 6.64 | 0.174 | 630 |
| | | −0.114 | 0.02 | | | | | | |
| *Tofua, Tonga* | | | | | | | | | |
| T2TF2 | Basaltic andesite | −0.021 | 0.019 | 0.872 | 52.9 | 5.76 | 4.28 | 0.204 | 814 |
| | | −0.016 | 0.018 | | | | | | |
| T4TF4 | Basaltic andesite | −0.083 | 0.017 | 1.18 | 55.5 | 4.45 | 5.45 | 0.217 | 835 |
| T7TF7 | Basaltic andesite | −0.105 | 0.015 | 0.957 | 53.6 | 4.76 | 5.11 | 0.187 | 797 |
| | | −0.068 | 0.017 | | | | | | |
| T9TF9 | Basaltic andesite | −0.075 | 0.014 | 0.954 | 53.9 | 4.79 | 5.15 | 0.185 | 793 |
| | | −0.034 | 0.016 | | | | | | |
| T12TF12 | Basaltic andesite | −0.116 | 0.013 | 1.36 | 53.6 | 4.76 | 5.09 | 0.268 | 821 |
| | | −0.044 | 0.016 | | | | | | |
| T14TF14 | Basaltic andesite | −0.052 | 0.017 | 1.18 | 53.8 | 4.79 | 5.07 | 0.232 | 815 |

## Results

Major to trace element, and Mo isotope data of analyzed samples are presented in Table 2 and S-5 to S-9. Molybdenum isotope ratios were averaged for data presentation and interpretation for samples that were analyzed multiple times.

### Sediments and oceanic crust

Pelagic sediments are enriched in Mo (4–103 $\mu g \cdot g^{-1}$) compared to the average upper continental crust (UCC) Mo concentration of 1.1 $\mu g \cdot g^{-1}$ (Table 2; Rudnick and Gao, 2014). Selected trace elements like Mo, Co, Ni, and Cu, which typically show an enrichment from seawater by adsorption onto Fe-Mn-oxides (Hein et al., 2003) are highly enriched in these pelagic sediments. This is indicated by higher SCo-1 normalized Mo/Ti (19–84), Co/Ti (8–39), Ni/Ti (3–35), and Cu/Ti (6–50) ratios (Fig. 3). This reference material is a geochemically well-characterized fine-grained silty marine shale with minor input of authigenic phases from seawater. Normalization by SCo-1 and aqueous immobile Ti thus enables the identification of authigenic element enrichment in investigated (meta)sediments (see Table S-10 for SCo-1 values used for normalization). Molybdenum concentration shows a moderate covariation with MnO (Fig. 4a) and a vertical trend in the sedimentary column starting with high concentrations in the top pelagic clays (up to 103 $\mu g \cdot g^{-1}$) and decreasing towards the bottom porcellanite-rich layers (down to 4.0 µg·g$^{-1}$). Molybdenum isotope compositions show significant variations along the sediment sequence with the lightest values observed at the near-surface samples (down to −0.47‰) and heaviest isotopic compositions for porcellanite and chert bearing clays (up to 0.19‰; Table 2). These trends are most pronounced by comparing the Mo/Mn ratio with stratigraphic depth and $\delta^{98/95}$Mo (Fig. 4b, c). Variably altered basalts (AOC) extracted from 70 to 119 m below seafloor (mbsf) at this site have Mo concentrations of 0.15–0.51 µg·g$^{-1}$ (Table 2) that are mostly lower than average MORB (0.46 µg·g$^{-1}$; Gale et al., 2013). These samples are less variable in Mo isotopic composition, ranging from −0.69‰ to −0.27‰ being lighter than N-MORB (−0.24 to −0.12‰, excluding the three heaviest MORB samples; Bezard et al., 2016) and AOC from ODP site 801 (−0.12 to 0.86‰; Freymuth et al., 2015; Fig. 5).

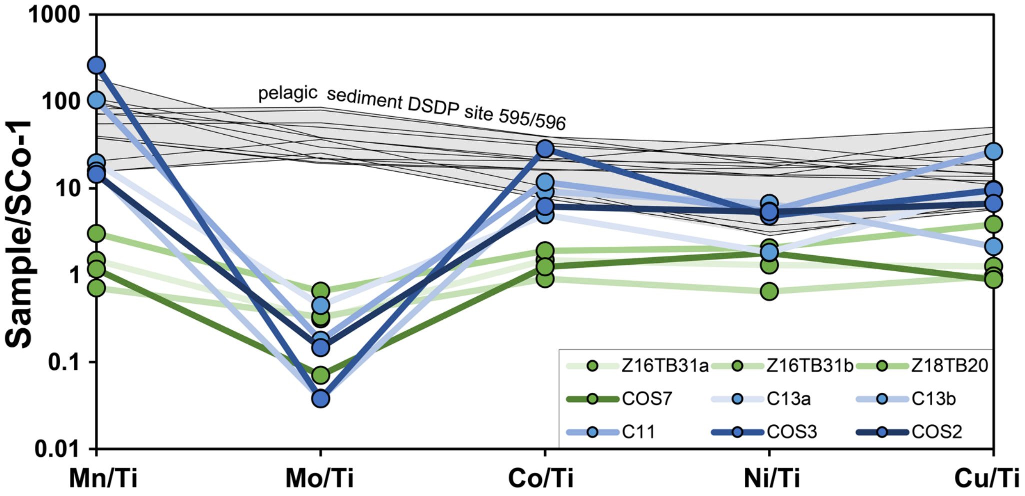

***Figure 3.*** *Plot of reference material SCo-1 and Ti-normalized concentrations of pelagic sediments and metasediments (see Table 1 for sample types) for elements, which are commonly enriched in deep-sea Mn-oxides (Hein et al., 2003). A significant decrease in Mo/Ti is observed for metasediments compared to pelagic sediments (DSDP site 595/596). SCo-1 values are preferred values from GeoRem (Jochum et al., 2005).*

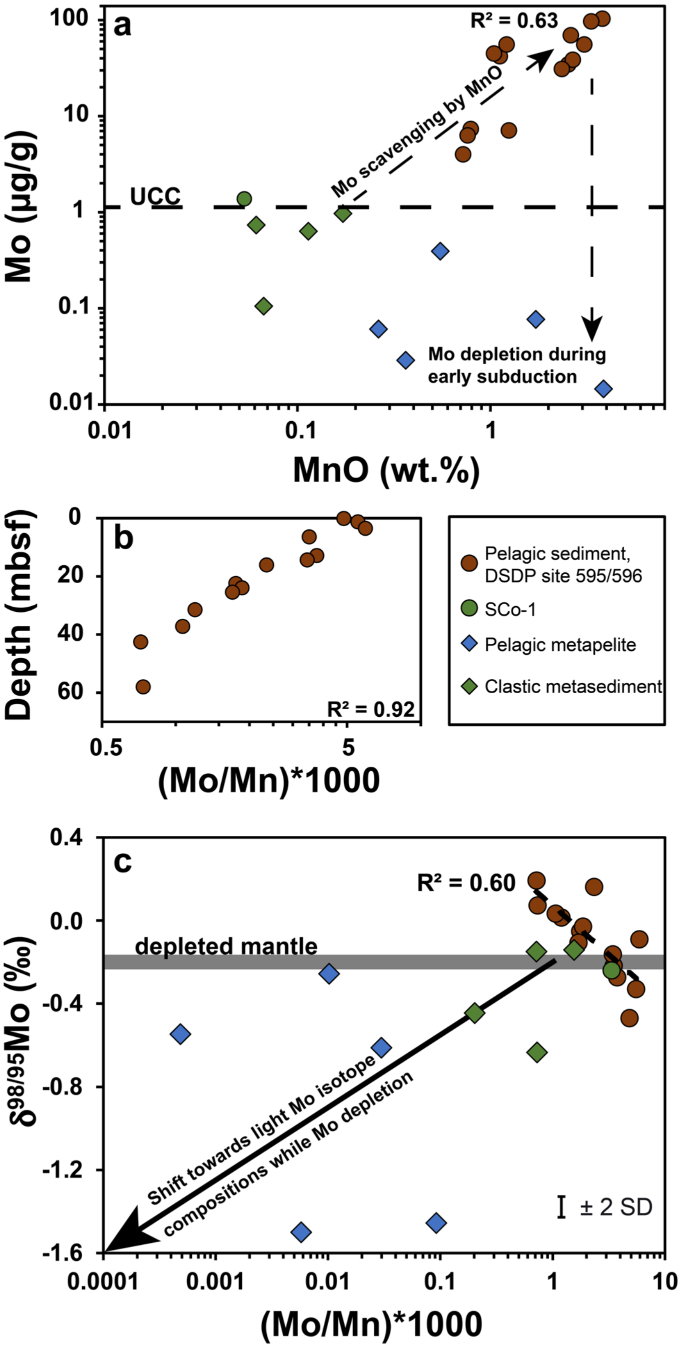

***Figure 4.*** *Covariation plots. (a) Mo vs. MnO showing a contrasting behavior of pelagic sediments vs. metasediments and suggesting a rapid loss of Mo during the early subduction in the forearc (see text); (b) depth (m below seafloor) vs. Mo/Mn of drill core pelagic sediments and (c)* $\delta^{98/95}$*Mo vs. Mo/Mn of analyzed pelagic sediments show a diagenetic effect causing Mo loss and isotope fractionation towards heavier Mo, while early subduction overprint lowers* $\delta^{98/95}$*Mo and Mo/Mn in metasediments (see text). Depleted mantle value from McCoy-West et al. (2019). UCC value from Rudnick and Gao (2014). SCo-1 values are preferred values from GeoRem (Jochum et al., 2005). 2 SD = Long-term reproducibility (2 standard deviations).*

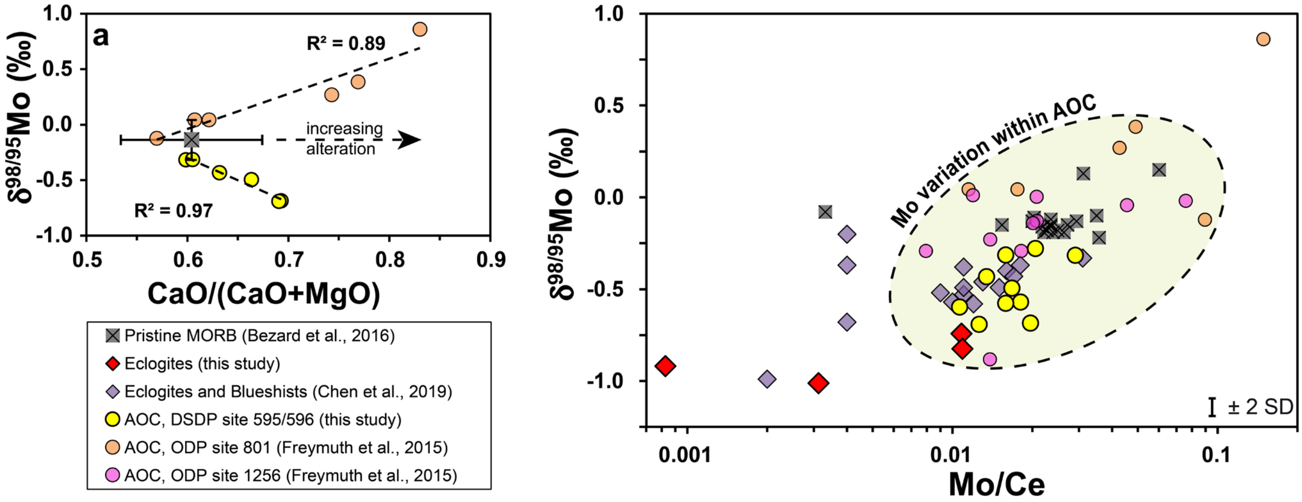

***Figure 5.*** *Plots of (a) $\delta^{98/95}$Mo vs. CaO/(CaO + MgO) showing contrasting behaviors of Mo isotope fractionation during seafloor basalt alteration (see text). CaO and MgO contents of AOC from OPD site 801 are from Kelley et al. (2003). Error bars of average MORB indicate 2 standard deviations of the dataset from Bezard et al. (2016). 2SD reproducibility is smaller than the point size; (b) $\delta^{98/95}$Mo vs. Mo/Ce of analyzed eclogites and AOC compared with previously published data. Note the large overall variation in Mo/Ce and $\delta^{98/95}$Mo of AOC (excluding one isotopically heavy outlier of Freymuth et al. (2015)), which partly overlaps with eclogites. However, even lower Mo/Ce and $\delta^{98/95}$Mo in eclogites can be explained by Mo loss and rutile formation during subduction metamorphism (see text). 2 SD = Long-term reproducibility (2 standard deviations).*

## Metamorphic rocks

$SiO_2$, $Al_2O_3$, and $TiO_2$ as well as HFSE and REE in AOC-type eclogites do not show a large deviation from average MORB composition. Alkali and earth alkali elements as well as LILE, however, show a much larger variability due to combined effects of seafloor alteration and metamorphic modification (Fig. S-2). Molybdenum concentrations (0.038 to 0.29 $\mu g \cdot g^{-1}$) and Mo/Ce ratios (0.0008 to 0.011) are lower compared to average MORB (Mo = 0.46 $\mu g \cdot g^{-1}$, Mo/Ce = 0.031; Gale et al., 2013) and lower $\delta^{98/95}$Mo (−0.74 to −1.01‰) are observed compared to MORB (Fig. 5b; Table 2).

Metasediments are divided into a) pelagic metapelites: C13a, C13b, C11, COS3 and COS2 and b) clastic metasediments: Z16TB31a, Z16TB31b, Z18TB20 and COS7 (Table 1) based on the following major and trace element systematics. Major element concentrations of clastic metasedimentary rocks from the Zermatt-Saas zone and Alpine Corsica are close to that of SCo-1, while pelagic metasediments from Lago di Cignana and Alpine Corsica are enriched in MnO compared to SCo-1 (Fig. S-3). Pelagic metasediments show high $SiO_2$ (from 76.8 to 84.7 wt%) and lower $TiO_2$ and $Al_2O_3$ contents compared to SCo-1. All metasediments display lower Mo concentrations and Mo/Ti ratios than SCo-1 (Fig. 3). Higher SCo-1 normalized Co/Ti, Ni/Ti, and Cu/Ti ratios of 5–28, 2–7 and 2–27 are observed in pelagic metasediments compared to clastic metasediments with ratios of 1–2, 1–2, and 1–4, respectively (Fig. 3). For these elements, pelagic metasediments are similarly enriched compared to non-subducted pelagic sediments from DSDP 595/596 (Fig. 3). Furthermore, Mo negatively covaries with MnO in analyzed metasediments displaying a contrasting behavior to non-subducted pelagic sediments (Fig. 4a) indicating a decoupling of these elements during subduction. In addition, metasediments exhibit anomalously low $\delta^{98/95}$Mo ratios (down to −1.50‰; Table 2).

## Tongan arc lavas

Molybdenum concentrations within Tongan arc volcanic rocks range from 0.48 to 1.36 $\mu g \cdot g^{-1}$ (Table 2), overlapping with the average UCC Mo concentration of 1.1 $\mu g \cdot g^{-1}$ (Rudnick and Gao, 2014). The Mo isotopic range of Kao, Late, and Tofua lavas (−0.15 to −0.02‰) exceeds that of the depleted mantle (−0.20 ± 0.02‰; McCoy-West et al., 2019) and is lighter than the average upper continental crust (+0.05 to +0.15‰; Freymuth et al., 2015; Voegelin et al., 2014; Willbold and Elliott, 2017; Yang et al., 2017). Ata lavas display a larger variation (−0.26 to −0.09‰) with some samples being lighter than the depleted mantle.

The average $\delta^{98/95}$Mo of Tongan arc lavas is −0.14 ± 0.13‰ (2SD, n = 27) (Table 2). This is similar to the arc lavas from the Solomon Arc with average Mo isotopic compositions of $\delta^{98/95}$Mo = −0.10 ± 0.39‰ (2SD, n = 6; König et al., 2016). Tongan arc lavas are isotopically lighter than the wet magmatic systems of Kos (0.21 ± 0.13‰; 2SD, n = 10), the Mariana arc (without isotopically light Agrigan island; 0.06 ± 0.07‰; 2SD, n = 10), the Lesser Antilles (0.00 ± 0.26‰; 2SD, n = 10), the Izu arc (−0.03 ± 0.16‰; 2SD, n = 16) and Banda arc (without isotopically light Serua island and one sample from Teon island; 0.11 ± 0.16‰; 2SD, n = 21) (Freymuth et al., 2016; Freymuth et al., 2015; Villalobos-Orchard et al., 2020; Voegelin et al., 2014; Wille et al., 2018). Tongan arc lavas are isotopically heavier compared to Cyprus (−0.26 ± 0.26‰; 2SD, n = 7), Papua New Guinea (−0.45 ± 0.97‰; 2SD, n = 8) and young Martinique arc lavas (−0.34 ± 0.45‰; 2SD, n = 10) with moderate to significant subducted sediment components (Gaschnig et al., 2017; König et al., 2016).

$SiO_2$ and MgO contents within Tongan arc lavas range from 50.0 to 56.3 wt% and 7.36 to 3.30 wt%, respectively, and show moderate covariation with Mo concentration and Mo/Ce, while there is no covariation with $\delta^{98/95}$Mo (Fig. 6; $SiO_2$ not shown). Compared to the depleted mantle, analyzed arc lavas display a higher Mo/Ce ratio that strongly covaries with slab-derived fluid indices, such as Ba/Th and Pb/Ce, with highest values observed in Tofua, followed by Late and Kao, and then Ata (Fig. 7a,b). $\delta^{98/95}$Mo moderately covaries with Ba/Th in Tongan arc lavas (Fig. 7c), and negatively with La/Sm that indicates the degree of mantle depletion (Fig. 8). Furthermore, variably good covariation can be observed between $\delta^{98/95}$Mo and Mo/Ce with As/Ce, Sb/Ce, and Cs/Th in studied arc lavas (Fig. 9; Cs/Th not shown).

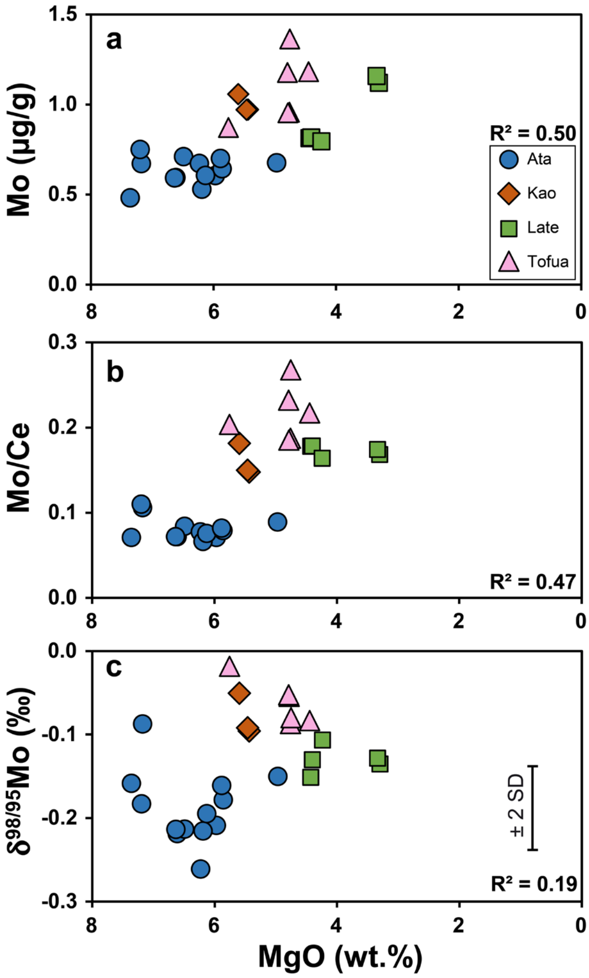

***Figure 6.*** *Mo concentration, Mo/Ce and $\delta^{98/95}$Mo of Tongan arc lavas as a function of MgO. 2 SD = Long-term reproducibility (2 standard deviations).*

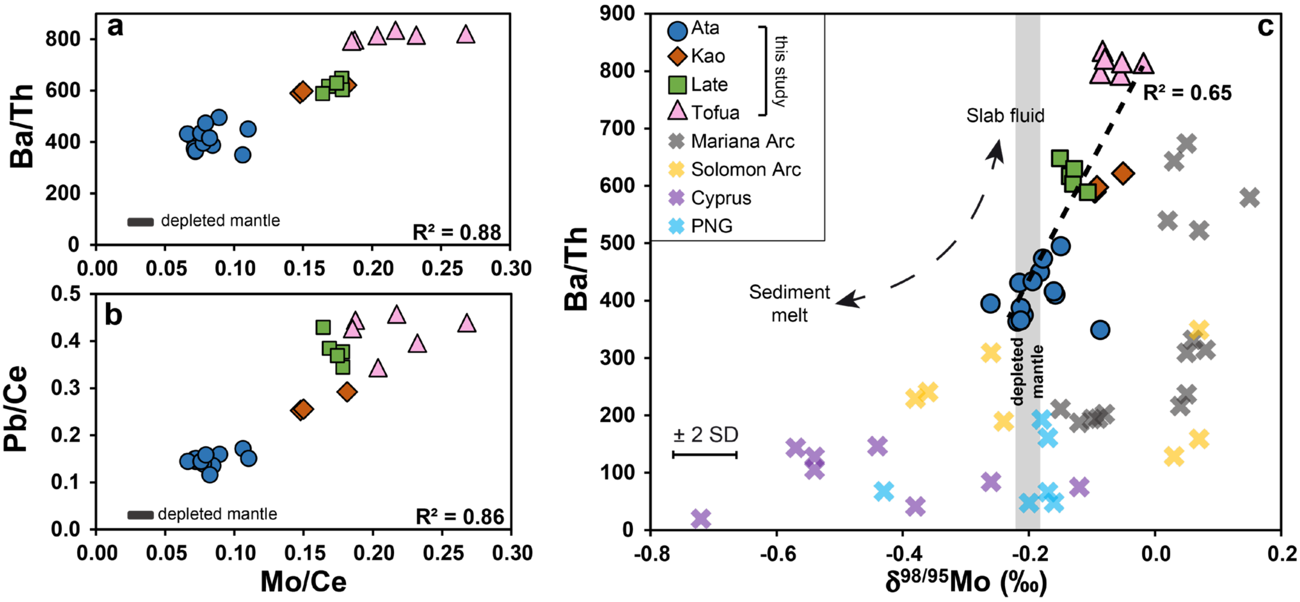

***Figure 7.*** *Plots of: (a) Ba/Th vs. Mo/Ce and (b) Pb/Ce vs. Mo/Ce of studied arc lavas show increasing relative fluid amounts between Ata and central Tongan volcanoes with accompanied increasing Mo/Ce; (c) Ba/Th vs. $\delta^{98/95}$Mo of studied arc lavas being in line with the global trend (Freymuth et al., 2015; König et al., 2016). Depleted mantle values from Salters and Stracke (2004) and McCoy-West et al. (2019). 2 SD = Long-term reproducibility (2 standard deviations).*

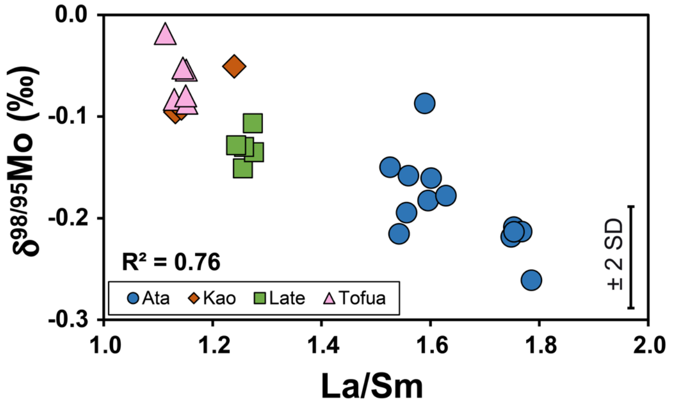

*Figure 8.* Covariation diagram of $\delta^{98/95}$Mo vs. La/Sm of analyzed arc lavas shows heavier isotope signatures with increased relative mantle depletions. 2 SD = Long-term reproducibility (2 standard deviations).

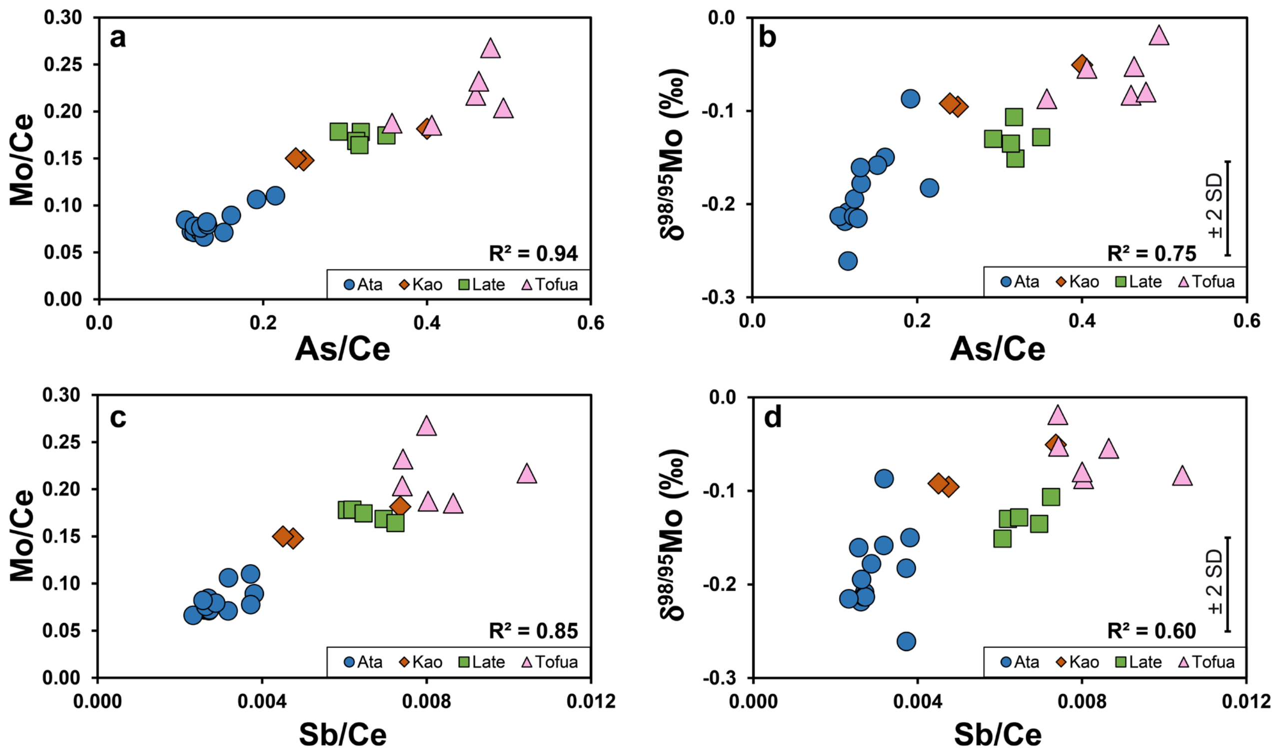

*Figure 9.* Covariation plot of analyzed arc lavas with: (a) Mo/Ce vs. As/Ce; (b) $\delta^{98/95}$Mo vs. As/Ce; (c) Mo/Ce vs. Sb/Ce; (d) $\delta^{98/95}$Mo vs. Sb/Ce. 2 SD = Long-term reproducibility (2 standard deviations).

# Discussion

## Controls on the Mo isotopic compositions of oceanic sediments and AOC subducting at the Tongan trench (DSDP site 595/596)

Overall higher Mo/Ti ratios in all DSDP 595 sediments relative to SCo-1 and moderate covariation of Mo with MnO confirm an authigenic Mo enrichment from seawater on Mn-oxyhydroxides (Fig. 3, Fig. 4a). Furthermore, the ~70 m thin pelagic sediment section of DSDP site 595/596 hosts more Mo than 6000 m of Pacific mafic oceanic crust (cf. Freymuth et al., 2015), indicating that sediments dominate the Mo budget entering the Tongan subduction zone. Adsorption of molybdate onto Mn-oxyhydroxides is associated with isotope fractionation of −3‰ $\Delta^{98/95}Mo_{(MnO\text{-}seawater)}$ (Barling et al., 2001; Barling and Anbar, 2004; Siebert et al., 2003). Molybdenum isotopic compositions of Fe-Mn crusts indicate an isotopically homogeneous Mo oceanic reservoir of 2.1‰ $\delta^{98/95}$Mo for the last 60 Ma and likely during most of the Phanerozoic (Kendall et al., 2017; Siebert et al., 2003). Consequently, due to the abundant presence of Mn-oxides dominating the Mo sedimentary budget at DSDP site 595/596 we suggest an initial $\delta^{98/95}$Mo of circa −0.9‰ for the pelagic sediments at the sediment-water interface at the time of sediment deposition. Decreasing Mo/Mn and higher $\delta^{98/95}$Mo of sediments with core depth and depositional age (Fig. 4b,c) potentially record an additional early diagenetic process resulting in Mo loss and fractionation likely related to the aging of Mn-oxyhydroxides during sediment deposition and compaction, which causes a higher structural order and lower reactivity of the Mn-phases (e.g., Eitel et al., 2018).

Menard et al., 1987 found that alteration of the mafic oceanic crust (70–119 mbsf) of DSDP site 595/596 occurred at low temperature and oxidizing conditions corresponding to the lower temperature (well below 100 °C) oxidation stage 5 of Johnson and Hall (1978). The penetration of seawater into the basalt causes the oxidation of ferrous iron and the generation of $H^+$ (Seyfried et al., 1978), which subsequently increases the dissolution of primary minerals in the basalt. These minerals release $Ca^{2+}$ and $Mg^{2+}$, which can lead to the formation of carbonate veins (Alt, 2003; Fisher, 1998). Carbonate veins found in AOC formed at low temperature for our study site (13–23 °C) and ODP site 801 (11–45 °C; Gillis and Coogan, 2011). As carbonate veins are associated with other alteration minerals in analyzed AOC samples, we use CaO/(CaO + MgO) to assess the degree of alteration. Lower $\delta^{98/95}$Mo values down to −0.69‰ with increasing degree of alteration are observed in analyzed AOC samples, suggesting a seafloor alteration control on the Mo isotopic signature (Fig. 5a). Likely, the formation of secondary minerals that formed during seafloor alteration preferentially adsorb isotopically light Mo from pore water. Depending on weathering kinetics, controlled by e.g. pore fluid residence time, composition and temperature, the pore fluid Mo reservoir is likely a variable mixture of isotopically heavy Mo derived from seawater and Mo derived from basalt weathering. Lower Mo/Ce ratios in our AOC samples indicate a net loss of Mo from MORB during alteration with rate of Mo incorporation during secondary mineral formation unable to counter-balance the Mo loss. We propose that the preferential incorporation of isotopically light Mo in this scenario is leading to isotopically lighter Mo values compared to unaltered MORB. On the other hand, higher Mo/Ce values therefore indicate a net gain of Mo during MORB alteration which is likely seawater derived, isotopically heavy Mo. The latter scenario is observed for AOC samples from ODP site 801 (subducting at the Mariana trench), which show heavier Mo isotope signatures and higher Mo/Ce ratios with increasing seafloor alteration (Freymuth et al., 2015; Fig. 5a, b). This implies that Mo enrichment and depletion during MORB alteration can lead to heavier and lighter $\delta^{98/95}$Mo compared to the depleted mantle, respectively. Thus, different reaction kinetics might play a role on the Mo concentration and isotopic signature during seafloor alteration, producing isotopically more heterogeneous AOC than previously anticipated. This shows that the respective subduction input likely provides a unique context for each arc system and may critically complement the investigation of the subduction output (in arc lavas).

## Controls on the Mo isotopic compositions of subducted oceanic crust and sediments

Clastic metasediments and, to a greater extent, pelagic metasediments have experienced a significant loss of (isotopically heavy) Mo well before entering the subarc region (Fig. 3, Fig. 4a, c). Molybdenum bound to Mn-oxide is easily mobilized, which can be already seen during early sediment deposition and diagenesis (Fig. 4b, c). The significant Mo loss in the metapelites compared to the non-subducted sediment samples from DSDP site 595/596 indicates a high mobility of Mo during early subduction especially when associated to oxyhydroxide phases. Relative to the MnO content, the metasediments are Mo depleted and retain low $\delta^{98/95}$Mo (Fig. 4c). Metapelites from Lago di Cignana represent the deepest subducted rocks of our sample set and exhibit the lightest Mo isotopic values. However, Lago di Cignana sample C13b shows higher $\delta^{98/95}$Mo in the range to that of the Corsica samples, which have experienced lower peak-pressures. Rather, the observed Mo systematics in metasediments are governed by their respective mineralogy (i.e. clastic vs. pelagic metasediments) before reaching peak P-T conditions. It may be concluded that significant Mo loss and isotope fractionation towards low $\delta^{98/95}$Mo in metasediments and especially in Mn-rich metapelites occurs already in the forearc. Therefore, it is likely that the significance of pelagic sedimentary Mo budget in subarc regions is relatively small. Fluids effervescing from mud volcanoes at the Mariana forearc show high Mo concentrations (up to ~0.6 $\mu g \cdot g^{-1}$) together with elevated Mn concentrations (Hulme et al., 2010). The authors have argued that microbially mediated changing redox conditions within the subducted sediments lead to the dissolution of metalliferous oxyhydroxides and to the mobilization of Mo during early subduction down to depth of 25 km below seafloor with estimated temperatures exceeding 200 °C (Hulme et al., 2010). The occurrence of small sulfides within the pelagic metasediments (Table 1) supports the hypothesis that sulfides formed during reducing conditions might have scavenged a small fraction of isotopically light Mo from the pore-fluid, leading to overall lighter bulk rock Mo isotopic composition (Nägler et al., 2011; Tossell, 2005). This is supported by the higher mobility of Mo compared to Co, Cu, and Ni as illustrated in lower Mo/Ti ratios relative to Co/Ti, Cu/Ti and Ni/Ti in pelagic, Mn-rich metapelites relative to their non-subducted counterparts at DSDP site 595/596 (Fig. 3) and by a negative covariation between $\delta^{98/95}$Mo and chalcophile Cu of $R^2 = 0.80$ (not shown). Molybdenum concentrations in clastic metasediments tend to be less affected during early subduction, indicating that the Mo host phase has a significant effect on Mo mobility in the sedimentary pile prior to and upon early subduction.

An additional process to sulfide growth that might cause Mo isotope fractionation in metasediments is the isotopically light Mo-incorporation into metamorphic rutile. This has already been proposed for basaltic eclogites (Chen et al., 2019). The formation of rutile could be simultaneous to release of Mo from other minerals such as sulfides by pressure solution processes (Large et al., 2007). In contrast to chalcophile element systematics that are controlled by recrystallized sulfides (König et al., 2021), the preferential incorporation of Mo into rutile can therefore either inherit the bulk rock Mo budget and isotopic signature or additionally fractionate Mo isotopes during external fluid flow (Chen et al., 2019). Besides the oxygen fugacity and salinity of the subduction zone fluids, rutile dominantly controls the Mo mobility (Bali et al., 2012) and is present in most analyzed metamorphic rocks (Table 1). Due to the variable $TiO_2$ content in non-subducted pelagic sediments (0.05–0.9 wt%; Table S-5) and generally low contents in pelagic metapelites (average 0.2 wt%; Table S-9), the effect of rutile is smaller compared to mafic eclogites, which have higher modal abundances of rutile. Further Mo isotopic analyses on single sulfides and rutile of metasediments are required to quantify the different isotope fractionation processes.

In a plot of $\delta^{98/95}$Mo vs. Mo/Ce (Fig. 5b) the range defined by our AOC samples coincides with our eclogite samples PF18–20 and PF18–26 and most of the mafic eclogites and blueschist samples analyzed by Chen et al. (2019), whereas some samples herein display even lower Mo/Ce, indicating that these Mo signatures could have been dominantly influenced by seafloor alteration processes. Furthermore, these eclogites cover peak metamorphic conditions between 1.7–2.5 GPa and 550–670 °C corresponding to forearc depths (Angiboust et al., 2009; Chen et al., 2019, and references therein; Fig. 2) suggesting that in some situations a large fraction of slab-Mo is already lost before entering subarc regions. As rutile is the dominant host of Mo in mafic eclogites (Chen et al., 2019; Zack et al., 2002) with ~85% of bulk Mo for PF18-20 and PF18-26 and ~54% for PF18-25a, this implies that most of the Mo is isotopically light well before entering subarc regions. Cerium is mainly hosted in allanite/epidote that is stable during progressive subduction zone metamorphism (Hermann, 2002). Therefore, bulk Mo/Ce and Mo isotope signatures will remain unmodified from upper blueschist-facies conditions (~400 °C, 45 km depth) onwards. Consequently, the lower Mo/Ce ratios in these eclogites imply that most Mo was lost prior to rutile crystallization. However, eclogite samples PF18-25a and

PF18-25c show $\delta^{98/95}$Mo down to −1.01‰ and lower Mo/Ce ratios, down to 0.0008, and are therefore outside the $\delta^{98/95}$Mo vs. Mo/Ce field defined by AOC samples investigated so far (Fig. 5b). This is line with several eclogite (and one blueschist) samples analyzed by Chen et al. (2019) and indicates a larger loss of Mo accompanied by an additional Mo isotope fractionation during subduction (Fig. 5b). Chen et al. (2019) interpreted low Mo/Ce ratios to be the result of selective mobilization of Mo relative to Ce during the interaction with fluids derived from the underlying serpentinized mantle. This does not apply for our investigated samples, as serpentine is stable in the adjacent ultramafic rocks (see also Fig. 2) and no evidence exists for a massive external fluid input. Indeed, these samples still display pristine pillow textures despite the eclogite-facies overprint (Fig. S-1), providing evidence for minimal deformation and external fluid input during subduction. Therefore, we interpret the low $\delta^{98/95}$Mo and Mo/Ce ratios in our mafic eclogites as a result of extensive seafloor alteration but do not want to exclude the potential of a superimposed Mo mobilization and fractionation process during subduction metamorphism within the forearc.

In summary, slab-released Mo, transported by aqueous fluids into the forearc mantle, may be isotopically heavy compared to residual eclogites. Metasediments record lighter Mo isotopic compositions when compared to their respective protoliths. Before entering subarc regions, most of the remaining eclogitic Mo is isotopically light and locked in rutile.

## Controls on the Mo isotopic compositions of Tongan arc lavas

Molybdenum concentrations increase with increasing $SiO_2$ and decreasing MgO contents (Fig. 6a; $SiO_2$ not shown); however, this relationship is likely not related to its incompatible behavior during fractional crystallization as indicated by increasing Mo/Ce ratios with decreasing MgO (Fig. 6b; Mo and Ce being of very similar compatibility during mantle melting). As degrees of mantle melting for studied Tongan arc islands are well above 10%, (e.g., Beier et al., 2017; Myeong et al., 2020), the observed Mo/Ce ratios cannot be explained through low-degree partial melting of 2–3% (Wang and Becker, 2018) (Fig. 6b). Also, the heavier Mo isotopic composition of Tongan arc lavas compared to depleted mantle cannot be explained by fractional crystallization of hydrous phases (Voegelin et al., 2014), since no clear relationship between indices of magmatic differentiation, such as MgO and $SiO_2$ concentration, and $\delta^{98/95}$Mo can be observed (Fig. 6c; $SiO_2$ not shown). The highest $\delta^{98/95}$Mo values are observed in arc lavas from Tofua, where volatile loss at shallow levels in the crust and temperatures above 950 °C, precludes the stabilization of amphibole (Caulfield et al., 2012). This indicates inhibited hydrous differentiation consistent with a complete absence of hydrous phases (Caulfield et al., 2012).

Elevated ratios of Ba/Th, Pb/Ce and Mo/Ce of Tongan arc lavas likely show an addition of Ba, Pb, and Mo, relative to their respective fluid-immobile denominators (Fig. 7a, b). Most pronounced fluid addition is thus seen in Tofua lavas, followed by Late and Kao. This coincides with $\delta^{98/95}$Mo ratios significantly heavier than mantle for these islands (Fig. 7c). Ata lavas on the other hand, show both lowest fluid-induced element ratios and $\delta^{98/95}$Mo that are (mostly) within uncertainty of mantle values. Overall, observed positive covariations between fluid parameters, relative Mo enrichments, and $\delta^{98/95}$Mo suggest slab-derived fluid enrichment of isotopically heavy Mo into the Tongan subarc mantle (Fig. 7). This is in agreement with results for arc lavas from the Mariana arc (Freymuth et al., 2015), Solomon Islands (König et al., 2016) and Izu arc (Villalobos-Orchard et al., 2020), where heavier Mo isotopic compositions than mantle have been linked to pronounced slab-derived aqueous fluid-enrichment. In comparison to other arc settings, arc lavas from Tofua show the highest Ba/Th ratios relative to a given $\delta^{98/95}$Mo (Fig. 7c). This is in part because slab-derived fluid effects are more notable relative to a highly depleted mantle wedge source (see also Fig. 8), as also observed based on radiogenic isotope systematics in Izu arc lavas (Villalobos-Orchard et al., 2020).

## The Mo subduction recycling conundrum

There is clear evidence that the shift in Mo isotopic composition in arc lavas is related to the addition of a subduction component (Fig. 7). However, the heavy Mo isotopic signature of Tongan arc lavas is difficult to explain via a simple aqueous fluid addition from the subducted slab at subarc depth (> 100 km). Large proportions of primary Mo hosted in the subducting sediment and altered oceanic crust are likely lost to the hanging wall mantle at forearc depths. This Mo mobilization likely depends on the stability of the Mo host phases during early subduction metamorphism. Furthermore, when rutile forms in forearc regions at around 1–1.5 GPa it incorporates most of the remaining and preferentially isotopically light Mo in subducted oceanic crust and sediments well before entering subarc regions. Based on coupled Pb and Mo isotope systematics, the deep, unaltered oceanic crust has been proposed as dominant source for slab-derived Mo in Mariana arc lavas (Freymuth et al., 2015). Because the solubility of rutile is very low in common subduction zone fluids (Audétat and Keppler, 2005) and Mo is highly compatible in rutile (Bali et al., 2012), rutile-bound Mo is unavailable for incorporation into slab dehydration fluid. Consequently, slab-derived aqueous fluids released at sub arc depth can be expected to transport negligible Mo. A process to mobilize rutile-bound Mo is partial melting of subducted AOC and metasediments at subarc depth, which would then provide an isotopically light Mo slab component of arc magmas. Such a model is in line with extremely low $\delta^{98/95}$Mo observed in Cyprus basalts and boninites, which was interpreted to be the result of sediment melt contribution of isotopically fractionated material (König et al., 2016). Furthermore, the Cyprus basalts and boninites display low Mo/Ce (and Ba/Th) suggesting that the subducted material already lost Mo prior to slab melting (König et al., 2016). The light $\delta^{98/95}$Mo, down to −0.26‰, and low Mo/Ce in Ata lavas might represent a signal from sediment melts. However, a clear geochemical identification of slab derived melt input into the subarc mantle remains elusive likely due to the lower degree of mantle depletion below Ata compared to Cyprus and $\delta^{98/95}$Mo close to the depleted mantle value. Therefore, we argue that the subarc slab does not represent a simple, single-stage Mo source to account for the isotopically heavy fluid-rich signatures of Kao, Late, and Tofua arc lavas. Instead, a multi stage Mo-recycling process involving the forearc mantle is required.

## A possible solution to the Mo subduction recycling conundrum for the Tongan subduction zone

Our new data from high-pressure rocks suggest that Mo mobility and isotope fractionation occurs during prograde subduction in the forearc region. The preferential incorporation of light Mo in eclogites and metasediments suggests that the Mo fluid flux infiltrating the forearc mantle wedge is isotopically heavy. This may lead to forearc serpentines with higher Mo/Ce ratios and higher $\delta^{98/95}$Mo compared to the overall Mo isotope composition of the subducted material. A potential contribution of the metasomatized forearc to subarc source regions (cf. Savov et al., 2005) of the Tongan arc islands could thus explain the observed Mo isotope systematics in Tongan arc lavas. Although forearc serpentines have not been measured for Mo concentration and isotope ratios so far, it is well known that serpentinization of the forearc mantle associated with shallow slab-derived fluid influx leads to an increase in bulk rock fluid mobile element concentrations, such as B, As, Cs, Sb, and Li (e.g., Savov et al., 2007). This hypothesis can be tested by comparing $\delta^{98/95}$Mo and Mo/Ce ratios with these shallow slab-derived fluid mobile elements. Moderate to strong covariation is observed between As/Ce, Sb/Ce, and Cs/Th against $\delta^{98/95}$Mo as well as Mo/Ce (Fig. 9; Cs/Th not shown). This indicates that the isotopically heavy slab-derived fluid signature in Tongan arc lavas might be derived from the metasomatized forearc mantle. The enrichment of these elements is associated with slab-derived fluid interaction with the overlying mantle in forearc regions at 200–600 °C (e.g., Cannaò and Malaspina, 2018 and references therein), which leads to a serpentinized forearc mantle reservoir with a distinctive geochemical fingerprint (e.g., Savov et al., 2007). The incorporation of such a forearc geochemical signature into arc lavas requires more complex models of arc magma genesis.

Tonarini et al. (2011) proposed a multi-stage subduction model, where early stage fluids released during shallow metamorphic dehydration of the slab variably metasomatize the overlying mantle wedge. Subsequent basal erosion transports the hanging wall serpentinized mantle material to subarc regions, where hydrous mineral breakdown conditions are likely reached along the slab surface geotherm (Fig. 2). The model was suggested based on compositions of arc lavas from the South Sandwich Islands, subducting marine sediments and dredged frontal arc peridotites. By analogy, B isotope compositions and mass balance calculations showed that high $\delta^{11}B$ in the arc lavas can only be explained by subduction/basal erosion of the forearc mantle wedge followed by the release of previously incorporated B at higher temperatures (Tonarini et al., 2011). This alternative process is suitable to explain the increasing contents of B and other fluid-mobile elements and also increasing $\delta^{11}B$ in the subarc mantle wedge (Tonarini et al., 2011).

There is thus significant reasoning that similar processes might act in the Tongan subduction zone. Geophysical data indicate serpentinization of ~30% of the Tongan forearc mantle (Contreras-Reyes et al., 2011), providing evidence for extensive interaction of the forearc mantle with slab-derived aqueous fluids. Furthermore, the absence of serpentine mud volcanoes at the Tongan trench indicates a rapid tectonic erosion of the forearc hanging wall, as the mantle is removed too quickly before being completely altered to serpentinite (Clift and Vannucchi, 2004; Contreras-Reyes et al., 2011). We therefore propose that Mo recycling at the Tongan arc might follow a similar multi-stage subduction recycling process as suggested by Tonarini et al. (2011) for the South Sandwich Islands based on B (Fig. 10). Besides simple downdrag of serpentinized portions in a compressive regime, a more complex recycling process could involve the influence of slab rollback. Indeed, the Tongan subduction zone retreated by about 1800 km during the last 90 My due to slab rollback (Schellart et al., 2006) with the development of a magmatically active back-arc basin spreading. Such a fast rollback may result in the migration of the wedge asthenospheric mantle along with the retreating subduction interface to eventually reach a position beneath earlier serpentinized lithospheric mantle portions. This would lead to the dehydration of serpentinites that have been previously enriched in fluid-mobile elements such as Mo, As, Sb, and Cs. Partial melts derived from the hot mantle wedge may then incorporate these fluids with a heavy Mo isotope signature en route to the arc crust where magmas evolve and eventually erupt. Hence, we propose multi-stage dehydration and the addition of forearc geochemical signatures to explain the Mo systematics of Tongan arc lavas. Our findings suggest that the subduction zone dynamics (accretion vs. erosion) and slab motion (rollback) have to be taken into account when investigating subduction zone recycling of Mo and other slab components to the source of arc magmas.

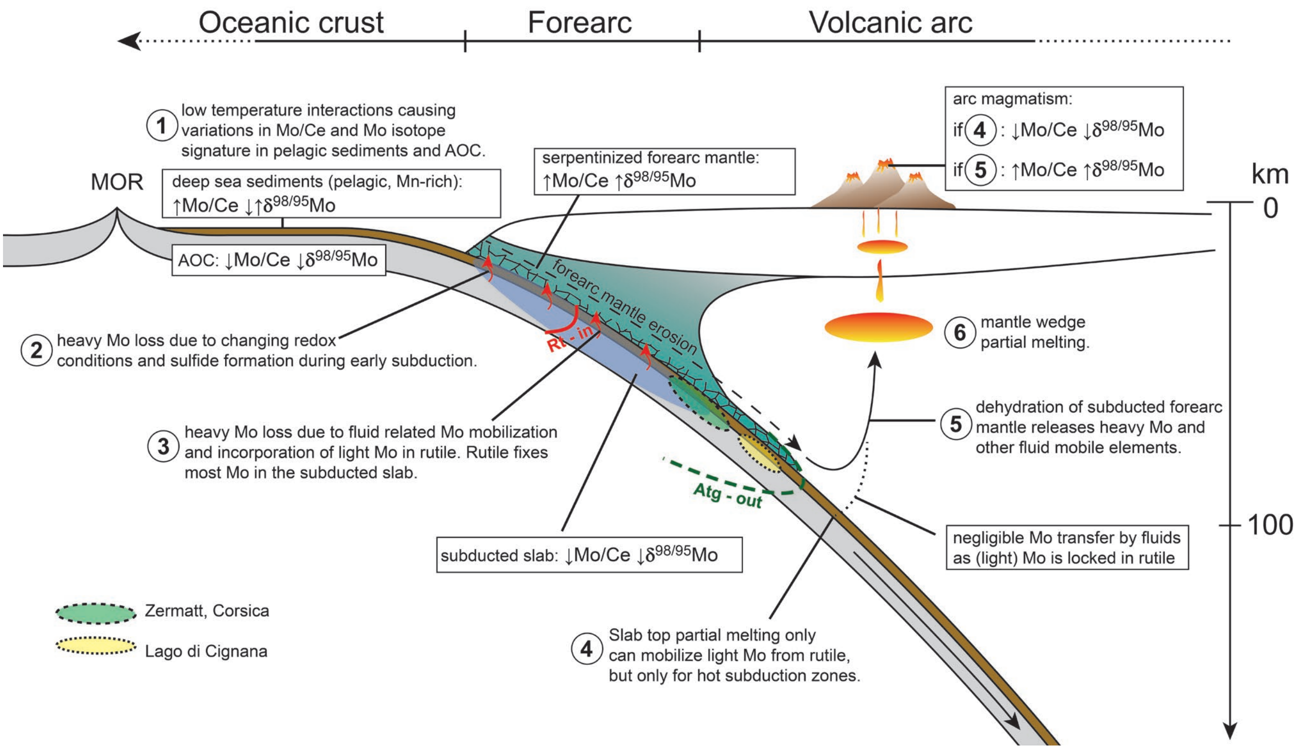

***Figure 10.*** *Illustration of the main processes in the Tongan subduction zone and the approximate peak P-T positions of studied metamorphic rocks. Furthermore, the Mo/Ce and Mo isotope ratios (compared to mantle) of the important Mo reservoirs are shown. Dehydration and loss of heavy Mo due to isotope fractionation during secondary mineral formation (2,3) leads to serpentinization of the overlying forearc mantle and enriches it in heavy Mo. Subsequent erosion and possibly slab rollback transports enriched forearc mantle into greater depths leading to antigorite dehydration and liberation of fluids with heavy Mo (5). Due to fluid induced melting in the mantle wedge, fluid-derived Mo is finally recycled into arc magmatism.*

## Conclusion

Based on a comparison of input to output geochemical and Mo isotope data at the Tongan subduction zone together with metamorphosed analogs of subducted oceanic crust and marine sediments we conclude:

1. Molybdenum mobility and isotope fractionation in subducting sediments are strongly dependent on the Mo host phase (Mn-oxide vs. silicate vs. rutile). Furthermore, changing redox conditions during early subduction lead to Mn-oxide dissolution and significant Mo mobilization. These redox changes result in potential sulfide formation and incorporation of light Mo into sulfides.
2. Low-temperature seawater alteration of the oceanic crust can lower Mo/Ce and shift Mo isotopic signature to smaller values and may at least partially explain Mo signatures that are then found in mafic eclogites. Our data contrast those reported for AOC at ODP site 801 (Freymuth et al., 2015), revealing that the processes of mafic oceanic crust alteration are likely diverse. Importantly, the combined data set suggests that AOC encompasses a large range of Mo concentrations and isotopic compositions, eventually available for subduction.

3. Comparison of AOC and pelagic sediment from DSDP site 595/596 with their subducted counterparts reveals significant Mo loss and isotopic fractionation already in the forearc – likely leading to higher Mo/Ce and $\delta^{98/95}$Mo in the serpentinized hanging wall mantle of the forearc. In mafic eclogites, the largest fraction of Mo is bound in rutile forming in forearc regions, thus locking this Mo at sub-solidus conditions down to subarc depths, implying negligible Mo mobilization by slab-derived fluids to the subarc mantle. At higher temperatures, this isotopically light Mo can be remobilized by partial slab melting.
4. Tongan arc lavas show higher $\delta^{98/95}$Mo than the ambient mantle. Positive covariations with fluid proxies link this Mo signature to the influx of isotopically heavy fluids from the slab. Such an isotopically heavy, slab-derived fluid signature is most pronounced where the highest degrees of mantle rock melt depletion occurred. Low Mo/Ce and $\delta^{98/95}$Mo in the subducted slab cannot directly explain slab-derived fluid Mo in Tongan arc lavas. The integration of the earlier metasomatized forearc mantle to subarc regions provides a suitable alternative process to explain observed variations in arc lavas by releasing previously incorporated isotopically heavy Mo. The recycling of the forearc mantle in subduction zones is supported by correlations of Mo/Ce and $\delta^{98/95}$Mo with fluid-mobile elements that are commonly enriched in the forearc mantle. This process possibly highlights that subduction erosion and slab rollback are important for Mo and possibly other element recycling in subduction zone settings.

## Acknowledgements

This work was funded by the Swiss National Science Foundation, Switzerland (Grant 182508) to M.W. S.K. and C.R. acknowledge ERC Starting Grant 636808 to S.K. ($O_2$RIGIN). The MC-ICP-MS at the Institute of Geological Sciences, University of Bern used in this study was acquired within the framework of the NCCR project PlanetS (Grant nr. 1NF40-141881). S.K. thanks the Tongan Geological Services for logistical support during the sampling campaign. This research used further samples provided by the International Ocean Discovery Program (IODP) to S.K. and M.W. We are grateful to Nathalie Zumbrunn, Thomas Bovay, Elias Kempf, and Diana Roos for providing samples and data from Zermatt and A. Vitale-Brovarone with assistance in fieldwork in Corsica. David Janssen is acknowledged for discussions that contributed to this manuscript. We also wish to thank Alex McCoy-West and 2 anonymous reviewers for constructive reviews, as well as Mirjam Schaller and Balz Kamber for editorial handling.

## References

Albut, G., Babechuk, M.G., Kleinhanns, I.C., Benger, M., Beukes, N.J., Steinhilber, B., Smith, A.J.B., Kruger, S.J., Schoenberg, R., 2018. Modern rather than Mesoarchaean oxidative weathering responsible for the heavy stable Cr isotopic signatures of the 2.95 Ga old Ijzermijn iron formation (South Africa). Geochim. Cosmochim. Acta 228, 157–189. https://doi.org/10.1016/j.gca.2018.02.034.

Alt, J. C. (2003), Stable isotopic composition of upper oceanic crust formed at a fast spreading ridge, ODP Site 801, Geochem. Geophys. Geosyst., 4, 8908. https://doi.org/10.1029/2002GC000400.

Angiboust, S., Agard, P., Jolivet, L., Beyssac, O., 2009. The Zermatt-Saas ophiolite: the largest (60-km wide) and deepest (c. 70–80 km) continuous slice of oceanic lithosphere detached from a subduction zone? Terra Nov. 21, 171–180. https://doi.org/10.1111/j.1365-3121.2009.00870.x.

Asael, D., Tissot, F.L.H., Reinhard, C.T., Rouxel, O., Dauphas, N., Lyons, T.W., Ponzevera, E., Liorzou, C., Chéron, S., 2013. Coupled molybdenum, iron and uranium stable isotopes as oceanic paleoredox proxies during the Paleoproterozoic Shunga Event. Chem. Geol. 362, 193–210. https://doi.org/10.1016/j.chemgeo.2013.08.003.

Audétat, A., Keppler, H., 2005. Solubility of rutile in subduction zone fluids, as determined by experiments in the hydrothermal diamond anvil cell. Earth Planet. Sci. Lett. 232, 393–402. https://doi.org/10.1016/j.epsl.2005.01.028.

Babechuk, M.G., Kamber, B.S., Greig, A., Canil, D., Kodolányi, J., 2009. The behaviour of tungsten during mantle melting revisited with implications for planetary differentiation time scales. Geochim. Cosmochim. Acta 74, 1448–1470. https://doi.org/10.1016/j.gca.2009.11.018.

Bali, E., Keppler, H., Audetat, A., 2012. The mobility of W and Mo in subduction zone fluids and the Mo-W-Th-U systematics of island arc magmas. Earth Planet. Sci. Lett. 351–352, 195–207. https://doi.org/10.1016/j.epsl.2012.07.032.

Ballance, P.F., Scholl, D.W., Vallier, T.L., Stevenson, A.J., Ryan, H., Herzer, R.H., 1989. Subduction of a Late Cretaceous Seamount of the Louisville Ridge at the Tonga Trench: a model of normal and accelerated tectonic erosion. Tectonics 8, 953–962. https://doi.org/10.1029/TC008i005p00953.

Barling, J., Anbar, A.D., 2004. Molybdenum isotope fractionation during adsorption by manganese oxides. Earth Planet. Sci. Lett. 217, 315–329. https://doi.org/10.1016/S0012-821X(03)00608-3.

Barling, J., Arnold, G.L., Anbar, A.D., 2001. Natural mass-dependent variations in the isotopic composition of molybdenum. Earth Planet. Sci. Lett. 193, 447–457. https://doi.org/10.1016/S0012-821X(01)00514-3.

Beier, C., Turner, S.P., Haase, K.M., Pearce, J.A., Münker, C., Regelous, M., 2017. Trace element and isotope geochemistry of the northern and central tongan islands with an emphasis on the genesis of high Nb/Ta signatures at the northern volcanoes of Tafahi and Niuatoputapu. J. Petrol. 58, 1073–1106. https://doi.org/10.1093/petrology/egx047.

Bevis, M., Taylor, F.W., Schutz, B.E., Recy, J., Isacks, B.L., Helu, S., Singh, R., Kendrick, E., Stowell, J., Taylor, B., Calmantli, S., 1995. Geodetic observations of very rapid convergence and back-arc extension at the Tonga arc. Nature 374, 249–251. https://doi.org/10.1038/374249a0.

Bezard, R., Fischer-Gödde, M., Hamelin, C., Brennecka, G.A., Kleine, T., 2016. The effects of magmatic processes and crustal recycling on the molybdenum stable isotopic composition of Mid-Ocean Ridge Basalts. Earth Planet. Sci. Lett. 453, 171–181. https://doi.org/10.1016/j.epsl.2016.07.056.

Burkhardt, C., Hin, R.C., Kleine, T., Bourdon, B., 2014. Evidence for Mo isotope fractionation in the solar nebula and during planetary differentiation. Earth Planet. Sci. Lett. 391, 201–211. https://doi.org/10.1016/j.epsl.2014.01.037.

Cannào, E., Malaspina, N., 2018. Oceanic to continental subduction: implications for the geochemical and redox evolution of the supra-subduction mantle. Geosphere 14, 2311–2336. https://doi.org/10.1130/GES01597.1.

Casalini, M., Avanzinelli, R., Tommasini, S., Elliott, T., Conticelli, S., 2019. Ce/Mo and molybdenum isotope systematics in subduction-related orogenic potassic magmas of Central-Southern Italy. Geochem. Geophys. Geosyst. 20, 2753–2768. https://doi.org/10.1029/2019GC008193.

Caulfield, J.T., Turner, S.P., Smith, I.E.M., Cooper, L.B., Jenner, G.A., 2012. Magma Evolution in the Primitive, Intra-oceanic Tonga Arc: Petrogenesis of Basaltic Andesites at Tofua Volcano. J. Petrol. 53, 1197–1230. https://doi.org/10.1093/petrology/egs013.

Chen, S., Hin, R.C., John, T., Brooker, R., Bryan, B., Niu, Y., Elliott, T., 2019. Molybdenum systematics of subducted crust record reactive fluid flow from underlying slab serpentine dehydration. Nat. Commun. 10 https://doi.org/10.1038/s41467-019-12696-3.

Clift, P., Vannucchi, P., 2004. Controls on tectonic accretion versus erosion in subduction zones: Implications for the origin and recycling of the continental crust. Rev. Geophys. 42 https://doi.org/10.1029/2003RG000127.

Contreras-Reyes, E., Grevemeyer, I., Watts, A.B., Flueh, E.R., Peirce, C., Moeller, S., Papenberg, C., 2011. Deep seismic structure of the Tonga subduction zone: implications for mantle hydration, tectonic erosion, and arc magmatism. J. Geophys. Res. Solid Earth 116. https://doi.org/10.1029/2011JB008434.

Eggins, S.M., Woodhead, J.D., Kinsley, L.P.J., Mortimer, G.E., Sylvester, P., McCulloch, M.T., Hergt, J.M., Handler, M.R., 1997. A simple method for the precise determination of ≥ 40 trace elements in geological samples by ICPMS using enriched isotope internal standardisation. Chem. Geol. 134, 311–326. https://doi.org/10.1016/S0009-2541(96)00100-3.

Eitel, E.M., Zhao, S., Tang, Y., Taillefert, M., 2018. Effect of manganese oxide aging and structure transformation on the kinetics of thiol oxidation. Environ. Sci. Technol. 52, 13202–13211. https://doi.org/10.1021/acs.est.8b03993.

Escrig, S., Bézos, A., Goldstein, S.L., Langmuir, C.H., Michael, P.J., 2009. Mantle source variations beneath the eastern lau spreading center and the nature of subduction components in the lau basin-tonga arc system. Geochem. Geophys. Geosyst. 10 https://doi.org/10.1029/2008GC002281.

Ewart, A., Collerson, K.D., Regelous, M., Wendt, J.I., Niu, Y., 1998. Geochemical evolution within the Tonga-Kermadec-Lau arc-back-arc systems: the role of varying mantle wedge composition in space and time. J. Petrol. Oxford Acad. https://doi.org/10.1093/PETROJ/39.3.331.

Fisher, A.T., 1998. Permeability within basaltic oceanic crust. Rev. Geophys. 36, 143–182. https://doi.org/10.1029/97RG02916.

Freymuth, H., Vils, F., Willbold, M., Taylor, R.N., Elliott, T., 2015. Molybdenum mobility and isotopic fractionation during subduction at the Mariana arc. Earth Planet. Sci. Lett. 432, 176–186. https://doi.org/10.1016/j.epsl.2015.10.006.

Freymuth, H., Elliott, T., van Soest, M., Skora, S., 2016. Tracing subducted black shales in the Lesser Antilles arc using molybdenum isotope ratios. Geology 44, 987–990. https://doi.org/10.1130/G38344.1.

Gale, A., Dalton, C.A., Langmuir, C.H., Su, Y., Schilling, J.G., 2013. The mean composition of ocean ridge basalts. Geochem. Geophys. Geosyst. 14, 489–518. https://doi.org/10.1029/2012GC004334.

Garbe-Schönberg, D., Müller, S., 2014. Nano-particulate pressed powder tablets for LAICP-MS. In: Journal of Analytical Atomic Spectrometry. Royal Society of Chemistry, pp. 990–1000. https://doi.org/10.1039/c4ja00007b.

Gaschnig, R.M., Reinhard, C.T., Planavsky, N.J., Wang, X., Asael, D., Chauvel, C., 2017. The molybdenum isotope system as a tracer of slab input in subduction zones: an example from Martinique, Lesser Antilles Arc. Geochem. Geophys. Geosyst. 18, 4674–4689. https://doi.org/10.1002/2017GC007085.

Gillis, K.M., Coogan, L.A., 2011. Secular variation in carbon uptake into the ocean crust. Earth Planet. Sci. Lett. 302, 385–392. https://doi.org/10.1016/j.epsl.2010.12.030.

Goldberg, T., Gordon, G., Izon, G., Archer, C., Pearce, C.R., McManus, J., Anbar, A.D., Rehkämper, M., 2013. Resolution of inter-laboratory discrepancies in Mo isotope data: an intercalibration. J. Anal. At. Spectrom. 28, 724–735. https://doi.org/10.1039/c3ja30375f.

Gordon, G.W., Lyons, T.W., Arnold, G.L., Roe, J., Sageman, B.B., Anbar, A.D., 2009. When do black shales tell molybdenum isotope tales? Geology 37, 535–538. https://doi.org/10.1130/G25186A.1.

Govindaraju, K., 1989. 1989 Compilation of working values and sample description for 272 geostandards. Geostand. Newslett. 13, 1–113. https://doi.org/10.1111/j.1751-908X.1989.tb00476.x.

Greber, N.D., Siebert, C., Nägler, T.F., Pettke, T., 2012. δ98/95Mo values and molybdenum concentration data for NIST SRM 610, 612 and 3134: towards a common protocol for reporting Mo data. Geostand. Geoanal. Res. 36, 291–300. https://doi.org/10.1111/j.1751-908X.2012.00160.x.

Greber, N.D., Puchtel, I.S., Nägler, T.F., Mezger, K., 2015. Komatiites constrain molybdenum isotope composition of the Earth's mantle. Earth Planet. Sci. Lett. 421, 129–138. https://doi.org/10.1016/j.epsl.2015.03.051.

Groppo, C., Beltrando, M., Compagnoni, R., 2009. The P-T path of the ultra-high pressure Lago Di Cignana and adjoining high-pressure meta-ophiolitic units: insights into the evolution of the subducting Tethyan slab. J. Metamorph. Geol. 27, 207–231. https:// doi.org/10.1111/j.1525-1314.2009.00814.x.

Guillong, M., Meier, D., Allan, M., Heinrich, C., Yardley, B., 2008. SILLS: a MATLAB based program for the reduction of laser ablation ICP-MS data of homogeneous materials and inclusions. Miner. Assoc. Can. Short Course 40.

Hein, J.R., Koschinsky, A., Halliday, A.N., 2003. Global occurrence of tellurium-rich ferromanganese crusts and a model for the enrichment of tellurium. Geochim. Cosmochim. Acta 67, 1117–1127. https://doi.org/10.1016/s0016-7037(02)01279-6.

Hermann, J., 2002. Allanite: Thorium and light rare earth element carrier in subducted crust. Chem. Geol. 192, 289–306. https://doi.org/10.1016/S0009-2541(02)00222-X.

Hermann, J., Spandler, C., Hack, A., Korsakov, A.V., 2006. Aqueous fluids and hydrous melts in high-pressure and ultra-high pressure rocks: implications for element transfer in subduction zones. Lithos 92, 399–417. https://doi.org/10.1016/j.lithos.2006.03.055.

Hulme, S.M., Wheat, C.G., Fryer, P., Mottl, M.J., 2010. Pore water chemistry of the Mariana serpentinite mud volcanoes: a window to the seismogenic zone. Geochem. Geophys. Geosyst. 11 https://doi.org/10.1029/2009GC002674.

Jochum, K.P., Nohl, U., Herwig, K., Lammel, E., Stoll, B., Hofmann, A.W., 2005. GeoReM: a new geochemical database for reference materials and isotopic standards. Geostand. Geoanal. Res. 29, 333–338. https://doi.org/10.1111/j.1751-908x.2005.tb00904.x.

Johnson, H.P., Hall, J.M., 1978. A detailed rock magnetic and opaque mineralogy study of the basalts from the Nazca Plate. Geophys. J. Int. 52, 45–64. https://doi.org/10.1111/j.1365-246X.1978.tb04221.x.

Kelley, K.A., Plank, T., Ludden, J., Staudigel, H., 2003. Composition of altered oceanic crust at ODP Sites 801 and 1149. Geochem. Geophys. Geosyst. 4 https://doi.org/10.1029/2002GC000435.

Kendall, B., Dahl, T.W., Anbar, A.D., 2017. Good Golly, Why Moly? The stable isotope geochemistry of molybdenum. In: Non-traditional Stable Isotopes. Walter de Gruyter GmbH, pp. 683–732. https://doi.org/10.2138/rmg.2017.82.16.

König, S., Münker, C., Schuth, S., Garbe-Schönberg, D., 2008. Mobility of tungsten in subduction zones. Earth Planet. Sci. Lett. 274, 82–92. https://doi.org/10.1016/j.epsl.2008.07.002.

König, S., Münker, C., Schuth, S., Luguet, A., Hoffmann, J.E., Kuduon, J., 2010. Boninites as windows into trace element mobility in subduction zones. Geochim. Cosmochim. Acta 74, 684–704. https://doi.org/10.1016/j.gca.2009.10.011.

König, S., Wille, M., Voegelin, A., Schoenberg, R., 2016. Molybdenum isotope systematics in subduction zones. Earth Planet. Sci. Lett. 447, 95–102. https://doi.org/10.1016/j.epsl.2016.04.033.

König, S., Rosca, C., Kurzawa, T., Varas-Reus, M.I., Dragovic, B., Schoenberg, R., John, T., 2021. Selenium isotope evidence for pulsed flow of oxidative slab fluids. Geochem. Perspect. Lett. 17, 27–32. https://doi.org/10.7185/geochemlet.2110.

Large, R.R., Maslennikov, V.V., Robert, F., Danyushevsky, L.V., Chang, Z., 2007. Multistage sedimentary and metamorphic origin of pyrite and gold in the Giant Sukhoi log deposit, Lena Gold Province, Russia. Econ. Geol. 102, 1233–1267. https://doi.org/10.2113/gsecongeo.102.7.1233.

Leeman, W.P., Tonarini, S., Turner, S., 2017. Boron isotope variations in Tonga-Kermadec-New Zealand arc lavas: implications for the origin of subduction components and mantle influences. Geochem. Geophys. Geosyst. 18, 1126–1162. https://doi.org/10.1002/2016GC006523.

Liang, Y.H., Halliday, A.N., Siebert, C., Fitton, J.G., Burton, K.W., Wang, K.L., Harvey, J., 2017. Molybdenum isotope fractionation in the mantle. Geochim. Cosmochim. Acta 199, 91–111. https://doi.org/10.1016/j.gca.2016.11.023.

McCoy-West, A.J., Chowdhury, P., Burton, K.W., Sossi, P., Nowell, G.M., Fitton, J.G., Kerr, A.C., Cawood, P.A., Williams, H.M., 2019. Extensive crustal extraction in Earth's early history inferred from molybdenum isotopes. Nat. Geosci. 12, 946–951. https://doi.org/10.1038/s41561-019-0451-2.

Menard, H.W., Natland, J., Jordan, T.H., Orcutt, J.A., et al., 1987. Site 595: Coring and Downhole Seismic Experiments in the Southwest Pacific Near the Tonga Trench., Initial Reports DSDP, Leg 91, Wellington to Papeete. US Govt. Printing Office; UK distributors, IPOD Committee, NERC, Swindon. https://doi.org/10.2973/dsdp.proc.91.102.1987.

Myeong, B., Kim, J., Kim, J.H., Jang, Y.D., 2020. Petrogenesis of subduction-related lavas from the southern Tonga arc. J. Asian Earth Sci. 188, 104089. https://doi.org/10.1016/j.jseaes.2019.104089.

Nägler, T.F., Neubert, N., Böttcher, M.E., Dellwig, O., Schnetger, B., 2011. Molybdenum isotope fractionation in pelagic euxinia: evidence from the modern Black and Baltic Seas. Chem. Geol. 289, 1–11. https://doi.org/10.1016/j.chemgeo.2011.07.001.

Peters, D., Pettke, T., 2017. Evaluation of major to ultra trace element bulk rock chemical analysis of nanoparticulate pressed powder pellets by LA-ICP-MS. Geostand. Geoanal. Res. 41, 5–28. https://doi.org/10.1111/ggr.12125.

Pettke, T., Oberli, F., Audétat, A., Guillong, M., Simon, A.C., Hanley, J.J., Klemm, L.M., 2012. Recent developments in element concentration and isotope ratio analysis of individual fluid inclusions by laser ablation single and multiple collector ICP-MS. Ore Geol. Rev. https://doi.org/10.1016/j.oregeorev.2011.11.001.

Plank, T., 2005. Constraints from Thorium/Lanthanum on sediment recycling at subduction zones and the evolution of the continents. J. Petrol. 46, 921–944. https://doi.org/10.1093/petrology/egi005.

Reinecke, T., 1991. Very-high-pressure metamorphism and uplift of coesite-bearing metasediments from the Zermatt-Saas zone, Western Alps. Eur. J. Mineral. 3, 7–18. https://doi.org/10.1127/ejm/3/1/0007.

Rudnick, R.L., Gao, S., 2014. Composition of the continental crust. In: Treatise on Geochemistry, Second ed. Elsevier Inc, pp. 1–51. https://doi.org/10.1016/B978-0-08-095975-7.00301-6.

Salters, V. J. M., and Stracke, A. (2004), Composition of the depleted mantle, Geochem. Geophys. Geosyst., 5, Q05B07. https://doi.org/10.1029/2003GC000597.

Savov, I.P., Ryan, J.G., D'Antonio, M., Kelley, K., Mattie, P., 2005. Geochemistry of serpentinized peridotites from the Mariana Forearc Conical Seamount, ODP Leg 125: implications for the elemental recycling at subduction zones. Geochem. Geophys. Geosyst. 6 https://doi.org/10.1029/2004GC000777.

Savov, I.P., Ryan, J.G., D'Antonio, M., Fryer, P., 2007. Shallow slab fluid release across and along the Mariana arc-basin system: insights from geochemistry of serpentinized peridotites from the Mariana fore arc. J. Geophys. Res. Solid Earth 112. https://doi.org/10.1029/2006JB004749.

Schellart, W.P., Lister, G.S., Toy, V.G., 2006. A Late Cretaceous and Cenozoic reconstruction of the Southwest Pacific region: tectonics controlled by subduction and slab rollback processes. Earth Sci. Rev. 76, 191–233. https://doi.org/10.1016/j.earscirev.2006.01.002.

Schuth, S., König, S., Münker, C., 2011. Subduction zone dynamics in the SW Pacific plate boundary region constrained from high-precision Pb isotope data. Earth Planet. Sci. Lett. 311, 328–338. https://doi.org/10.1016/j.epsl.2011.09.006.

Seyfried, W.E., Shanks, W.C., Dibble, W.E., 1978. Clay mineral formation in DSDP Leg 34 basalt. Earth Planet. Sci. Lett. 41, 265–276. https://doi.org/10.1016/0012-821X(78)90183-8.

Siebert, C., Nägler, T.F., Kramers, J.D., 2001. Determination of molybdenum isotope fractionation by double-spike multicollector inductively coupled plasma mass spectrometry. Geochem. Geophys. Geosyst. 2 https://doi.org/10.1029/2000GC000124.

Siebert, C., Nägler, T.F., von Blanckenburg, F., Kramers, J.D., 2003. Molybdenum isotope records as a potential new proxy for paleoceanography. Earth Planet. Sci. Lett. 211, 159–171. https://doi.org/10.1016/S0012-821X(03)00189-4.

Skora, S., Freymuth, H., Blundy, J., Elliott, T., Guillong, M., 2017. An experimental study of the behaviour of cerium/molybdenum ratios during subduction: implications for tracing the slab component in the Lesser Antilles and Mariana Arc. Geochim. Cosmochim. Acta 212, 133–155. https://doi.org/10.1016/j.gca.2017.05.025.

Syracuse, E.M., van Keken, P.E., Abers, G.A., Suetsugu, D., Bina, C., Inoue, T., Wiens, D., Jellinek, M., 2010. The global range of subduction zone thermal models. Phys. Earth Planet. Inter. 183, 73–90. https://doi.org/10.1016/j.pepi.2010.02.004.

Tonarini, S., Leeman, W.P., Leat, P.T., 2011. Subduction erosion of forearc mantle wedge implicated in the genesis of the South Sandwich Island (SSI) arc: evidence from boron isotope systematics. Earth Planet. Sci. Lett. 301, 275–284. https://doi.org/10.1016/j.epsl.2010.11.008.

Tossell, J.A., 2005. Calculating the partitioning of the isotopes of Mo between oxidic and sulfidic species in aqueous solution. Geochim. Cosmochim. Acta 69, 2981–2993. https://doi.org/10.1016/j.gca.2005.01.016.

Turner, S., Hawkesworth, C., Rogers, N., Bartlett, J., Worthington, T., Hergt, J., Pearce, J., Smith, I., 1997. 238U-230Th disequilibria, magma petrogenesis, and flux rates beneath the depleted Tonga-Kermadec island arc. Geochim. Cosmochim. Acta 61, 4855–4884. https://doi.org/10.1016/S0016-7037(97)00281-0.

Ulmer, P., Trommsdorff, V., 1995. Serpentine stability to mantle depths and subduction related magmatism. Science 268, 858–861. https://doi.org/10.1126/science.268.5212.858.

Ulrich, T., Kamber, B.S., Woodhead, J.D., Spencer, L.A., 2010. Long-term observations of isotope ratio accuracy and reproducibility using quadrupole ICP-MS. Geostand. Geoanal. Res. 34, 161–174. https://doi.org/10.1111/j.1751-908X.2010.00046.x.

Villalobos-Orchard, J., Freymuth, H., O'Driscoll, B., Elliott, T., Williams, H., Casalini, M., Willbold, M., 2020. Molybdenum isotope ratios in Izu arc basalts: the control of subduction zone fluids on compositional variations in arc volcanic systems. Geochim. Cosmochim. Acta 288, 68–82. https://doi.org/10.1016/j.gca.2020.07.043.

Vitale-Brovarone, A., Groppo, C., Hetényi, G., Compagnoni, R., Malavielle, J., 2011. Coexistence of lawsonite-bearing eclogite and blueschist: phase equilibria modelling of Alpine Corsica metabasalts and petrological evolution of subducting slabs. J. Metamorph. Geol. 29, 583–600. https://doi.org/10.1111/j.1525-1314.2011.00931.x.

Voegelin, A.R., Pettke, T., Greber, N.D., von Niederhäusern, B., Nägler, T.F., 2014. Magma differentiation fractionates Mo isotope ratios: evidence from the Kos Plateau Tuff (Aegean Arc). Lithos 190–191, 440–448. https://doi.org/10.1016/j.lithos.2013.12.016.

Wang, Z., Becker, H., 2018. Molybdenum partitioning behavior and content in the depleted mantle: insights from Balmuccia and Baldissero mantle tectonites (Ivrea Zone, Italian Alps). Chem. Geol. 499, 138–150. https://doi.org/10.1016/j.chemgeo.2018.09.023.

Wei, S.S., Wiens, D.A., van Keken, P.E., Cai, C., 2017. Slab temperature controls on the Tonga double seismic zone and slab mantle dehydration. Sci. Adv. 3, e1601755. https://doi.org/10.1126/sciadv.1601755.

Weis, D., Kieffer, B., Maerschalk, C., Barling, J., De Jong, J., Williams, G.A., Hanano, D., Pretorius, W., Mattielli, N., Scoates, J.S., Goolaerts, A., Friedman, R.M., Mahoney, J. B., 2006. High-precision isotopic characterization of USGS reference materials by TIMS and MC-ICP-MS. Geochem. Geophys. Geosys. 7. https://doi.org/10.1029/2006GC001283.

Willbold, M., Elliott, T., 2017. Molybdenum isotope variations in magmatic rocks. Chem. Geol. 449, 253–268. https://doi.org/10.1016/j.chemgeo.2016.12.011.

Willbold, M., Hibbert, K., Lai, Y.-J., Freymuth, H., Hin, R.C., Coath, C., Vils, F., Elliott, T., 2016. High-precision mass-dependent molybdenum isotope variations in magmatic rocks determined by double-spike MC-ICP-MS. Geostand. Geoanal. Res. 40, 389–403. https://doi.org/10.1111/j.1751-908X.2015.00388.x.

Wille, M., Nebel, O., Van Kranendonk, M.J., Schoenberg, R., Kleinhanns, I.C., Ellwood, M.J., 2013. Mo-Cr isotope evidence for a reducing Archean atmosphere in 3.46-2.76Ga black shales from the Pilbara, Western Australia. Chem. Geol. 340, 68–76. https://doi.org/10.1016/j.chemgeo.2012.12.018.

Wille, M., Nebel, O., Pettke, T., Vroon, P.Z., König, S., Schoenberg, R., 2018. Molybdenum isotope variations in calc-alkaline lavas from the Banda arc, Indonesia: assessing the effect of crystal fractionation in creating isotopically heavy continental crust. Chem. Geol. 485, 1–13. https://doi.org/10.1016/j.chemgeo.2018.02.037.

Yang, J., Siebert, C., Barling, J., Savage, P., Liang, Y.H., Halliday, A.N., 2015. Absence of molybdenum isotope fractionation during magmatic differentiation at Hekla volcano, Iceland. Geochim. Cosmochim. Acta 162, 126–136. https://doi.org/10.1016/j.gca.2015.04.011.

Yang, J., Barling, J., Siebert, C., Fietzke, J., Stephens, E., Halliday, A.N., 2017. The molybdenum isotopic compositions of I-, S- and A-type granitic suites. Geochim. Cosmochim. Acta 205, 168–186. https://doi.org/10.1016/j.gca.2017.01.027.

Zack, T., Kronz, A., Foley, S.F., Rivers, T., 2002. Trace element abundances in rutiles from eclogites and associated garnet mica schists. Chem. Geol. 184, 97–122. https://doi.org/10.1016/S0009-2541(01)00357-6.

Zhang, Y., Yuan, C., Sun, M., Li, J., Long, X., Jiang, Y., Huang, Z., 2020. Molybdenum and boron isotopic evidence for carbon-recycling via carbonate dissolution in subduction zones. Geochim. Cosmochim. Acta 278, 340–352. https://doi.org/10.1016/j.gca.2019.12.013.

Zhao, P.-P., Li, J., Zhang, L., Wang, Z.-B., Kong, D.-X., Ma, J.-L., Wei, G.-J., Xu, J.-F., 2016. Molybdenum mass fractions and isotopic compositions of international geological reference materials. Geostand. Geoanal. Res. 40, 217–226. https://doi.org/10.1111/j.1751-908X.2015.00373.x.

Zhou, L., Kyte, F.T., 1992. Sedimentation history of the South Pacific pelagic clay province over the last 85 million years Inferred from the geochemistry of Deep Sea Drilling Project Hole 596, Paleoceanography, 7( 4), 441– 465, https://doi.org/10.1029/92PA01063.

# Supplementary Material

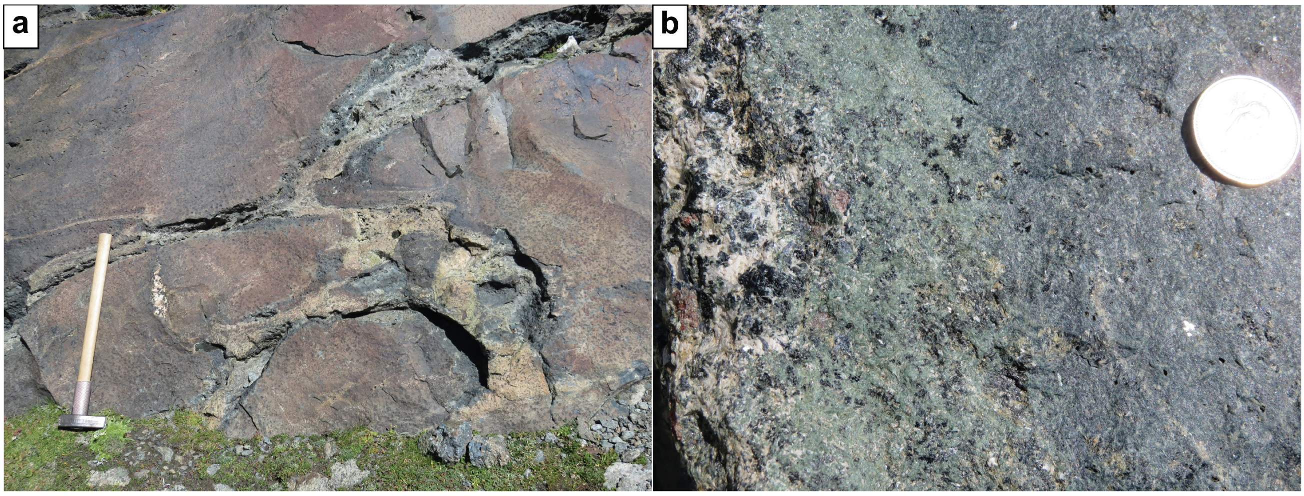

***Figure S-1.*** *Outcrop photo of collected eclogite samples: (a) PF18-25a (less altered pillow core) & PF18-25c (more altered pillow rim). Pristine pillow and inter-pillow basalt textures are preserved; (b) Glaucophane-rich eclogites PF18-20 (less altered, right in image) & PF18-26 (strongly altered, left in image).*

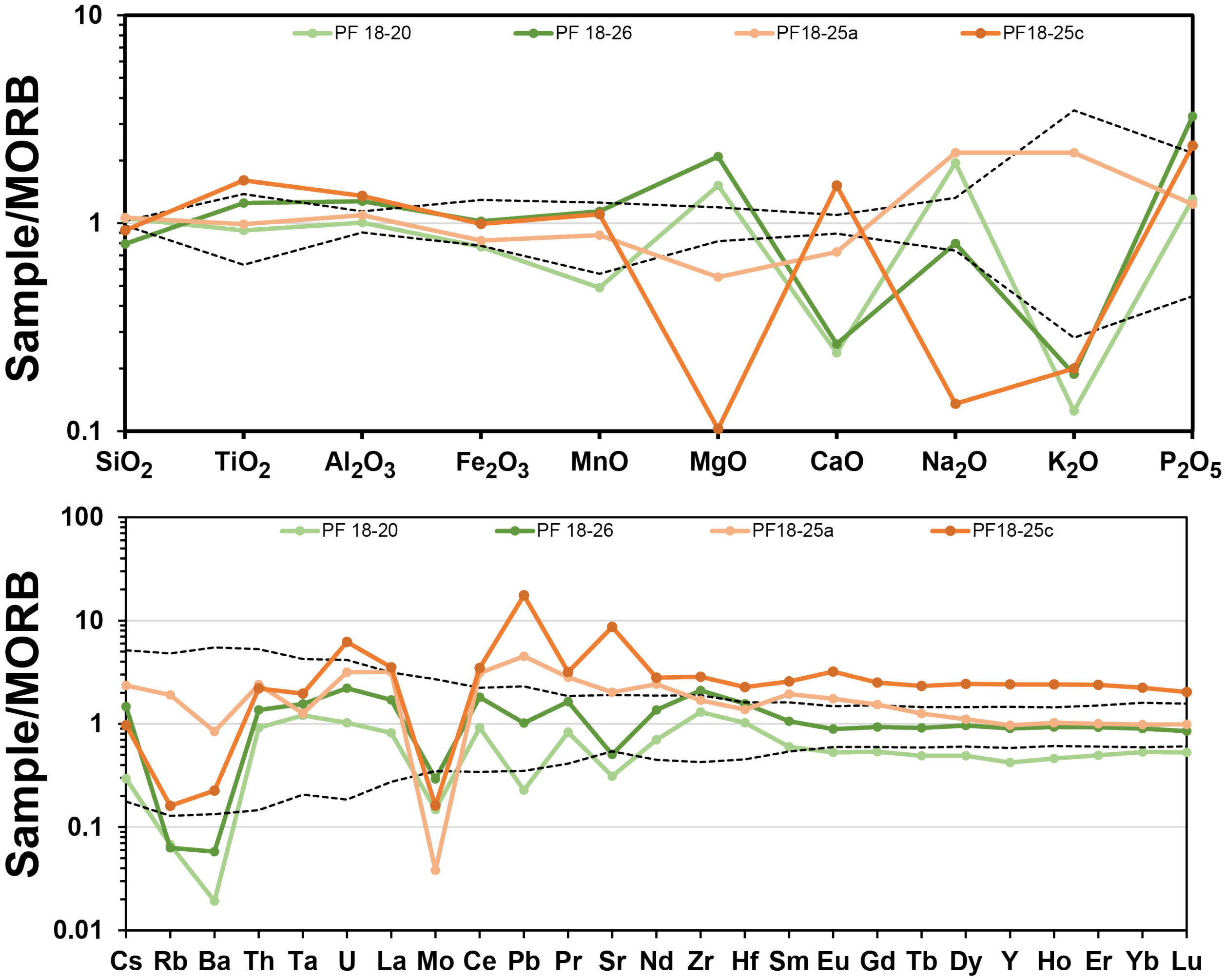

***Figure S-2.*** *MORB-normalized element concentration diagrams of analyzed eclogite samples: a) major element oxide concentration and b) minor and trace element concentration. Average MORB from Gale et al. (2013). Dashed lines indicate the 95% confidence interval of the ALL MORB mean dataset from Gale et al. (2013).*

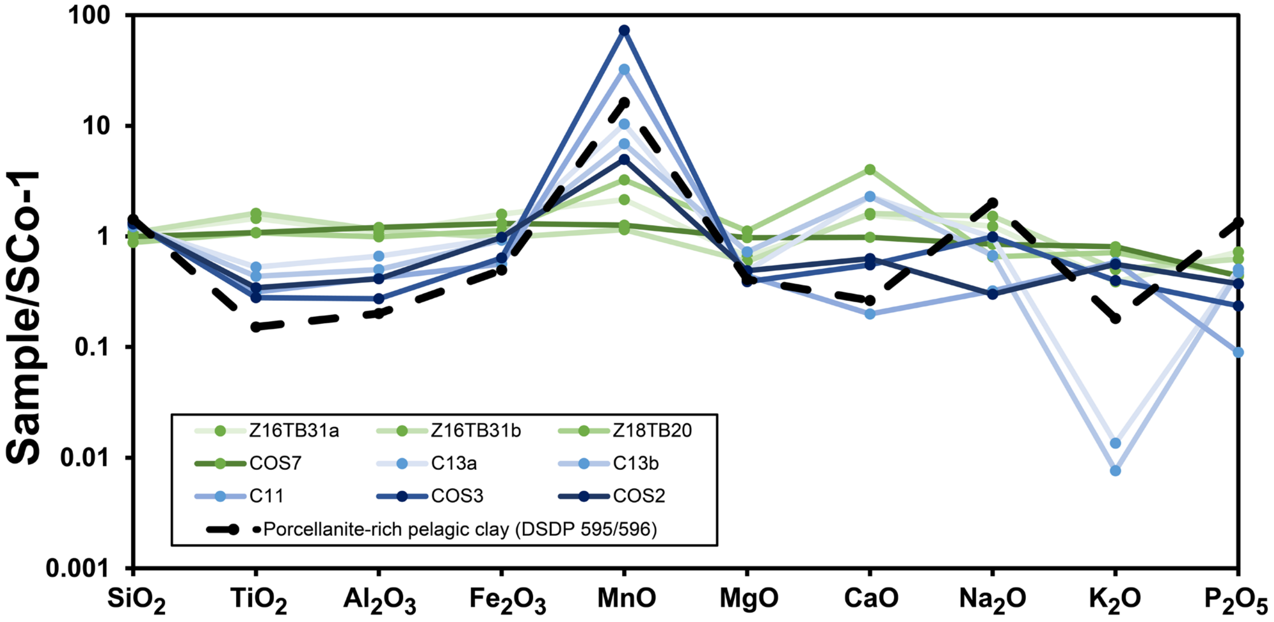

***Figure S-3.*** *Reference material (SCo-1) -normalized major element concentrations of analyzed metasediments and average porcellanite-rich pelagic clay from DSDP site 595/596. Note the elevated MnO concentrations in pelagic (meta)sediments. SCo-1 values are preferred values from GeoRem (Jochum et al., 2005).*

***Table S-1.*** *Measured certified reference material $\delta^{98/95}$Mo relative to NIST SRM 3134 (‰). 2 SD = 2 standard deviations*

| | NOD-A-1 | NOD-P-1 | BHVO-2 | AGV-2 | W-2a |
|---|---|---|---|---|---|
| 4/18/2019 | −0.609 | −0.856 | | | |
| 5/14/2019 | −0.658 | −0.876 | | | |
| 7/31/2019 | | | −0.090 | −0.218 | −0.066 |
| 8/16/2019 | | −0.877 | −0.059 | −0.188 | −0.057 |
| 9/5/2019 | | | −0.065 | −0.160 | −0.021 |
| 1/21/2020 | | | −0.063 | −0.161 | −0.066 |
| 1/21/2020 | | | −0.099 | | |
| 1/25/2020 | | | −0.049 | −0.195 | −0.042 |
| 6/13/2020 | | | −0.121 | −0.197 | −0.083 |
| Average | −0.63 | −0.87 | −0.08 | −0.19 | −0.06 |
| 2 SD | 0.05 | 0.02 | 0.05 | 0.04 | 0.04 |

***Table S-2.*** *Reference material reproducibility during the measurement of trace elements in arc lavas with solution ICP-MS*

| | W-2a | | | BIR-1a | | | BIR-1a | | | BHVO-2 | | | BHVO-2 | | |
|---|---|---|---|---|---|---|---|---|---|---|---|---|---|---|---|
| Element | measured (ppb) | literature (ppb)* | RSD (%) | measured (ppb) | literature (ppb)* | RSD (%) | measured (ppb) | literature (ppb)* | RSD (%) | measured (ppb) | literature (ppb)* | RSD (%) | measured (ppb) | literature (ppb)* | RSD (%) |
| As | 1260 | 1260 | 0.9 | 70.9 | 70 | 0.9 | 107 | 70 | 29.6 | 931 | 700 | 20.0 | 1100 | 700 | 31.4 |
| Sb | 800 | 800 | 0.3 | 502 | 433.3 | 10.4 | 438 | 433.3 | 0.8 | 109 | 89.99 | 13.4 | 86.1 | 89.99 | 3.1 |
| Cs | 888 | 888 | 0.4 | 4.81 | 5.681 | 11.7 | 4.98 | 5.681 | 9.3 | 96.9 | 96.67 | 0.1 | 102 | 96.67 | 3.9 |
| Ba | 169681 | 169680 | 0.4 | 6523 | 6464 | 0.6 | 6437 | 6464 | 0.3 | 131981 | 131300 | 0.4 | 128795 | 131300 | 1.4 |
| La | 10521 | 10521 | 0.2 | 597 | 599.7 | 0.3 | 594 | 599.7 | 0.7 | 15310 | 15190 | 0.6 | 14973 | 15190 | 1.0 |
| Ce | 23217 | 23216 | 0.4 | 1893 | 1901 | 0.3 | 1878 | 1901 | 0.9 | 38009 | 37760 | 0.5 | 37260 | 37760 | 0.9 |
| Sm | 3266 | 3266 | 0.6 | 1091 | 1099 | 0.5 | 1089 | 1099 | 0.7 | 6100 | 6059 | 0.5 | 6069 | 6059 | 0.1 |
| Pb | 7528 | 7528 | 0.0 | 3068 | 2958 | 2.6 | 2712 | 2958 | 6.1 | 1586 | 1530 | 2.5 | 1404 | 1530 | 6.1 |
| Th | 2105 | 2104 | 2.6 | 29 | 29.72 | 2.4 | 28 | 29.72 | 3.3 | 1234 | 1179 | 3.2 | 1163 | 1179 | 1.0 |

*= values after Babechuk et al. (2009)

***Table S-3.*** *Reference material reproducibility during the measurement of trace elements in pelagic sediments & altered oceanic crust (DSDP 595/596) with solution ICP-MS*

| | W-2a | | | BIR-1a | | | BIR-1a | | | BHVO-2 | | |
|---|---|---|---|---|---|---|---|---|---|---|---|---|
| Element | measured (ppb) | literature (ppb)* | RSD (%) | measured (ppb) | literature (ppb)* | RSD (%) | measured (ppb) | literature (ppb)* | RSD (%) | measured (ppb) | literature (ppb)* | RSD (%) |
| Co | 44526 | 44526 | 0.3 | 53417 | 52800 | 0.8 | 53228 | 52800 | 0.6 | 45408 | 45300 | 0.2 |
| Ni | 69997 | 69993 | 0.9 | 170045 | 166100 | 1.7 | 170441 | 166100 | 1.8 | 117482 | 117900 | 0.3 |
| Cu | 103011 | 103000 | 1.3 | 120132 | 116200 | 2.4 | 119649 | 116200 | 2.1 | 123264 | 125500 | 1.3 |
| Ce | 23217 | 23216 | 0.6 | 1891 | 1901 | 0.4 | 1893 | 1901 | 0.3 | 37528 | 37760 | 0.4 |

*= values after Babechuk et al. (2009)

***Table S-4.*** *Reference material reproducibility during the measurement of major and trace elements in metamorphic rocks with LA-ICP-MS. FeO = $Fe_2O_3$ total. Values for element-oxides are in wt%. All other values (trace elements) are in µg/g. SD = standard deviation. RSD = relative standard deviation.*

| Element | Mean (n=12) | 1 SD | RSD (%) | Reference OKUM | Measured − Reference (%) | Comment |
|---|---|---|---|---|---|---|
| $SiO_2$ | 47.99 | 1.39 | 2.9 | 44.55 | 7.7 | |
| $TiO_2$ | 0.36 | 0.01 | 2.1 | 0.35 | 2.8 | |
| $Al_2O_3$ | 8.07 | 0.14 | 1.7 | 7.70 | 4.7 | |
| FeO | 10.88 | 0.27 | 2.5 | 11.75 | −7.4 | |
| MnO | 0.17 | 0.002 | 1.3 | 0.18 | −8.2 | |
| MgO | 22.89 | 0.49 | 2.2 | 21.43 | 6.8 | |
| CaO | 8.15 | 0.16 | 1.9 | 7.71 | 5.7 | |
| $Na_2O$ | 1.21 | 0.02 | 1.6 | 1.10 | 10.6 | |
| $K_2O$ | 0.048 | 0.002 | 3.7 | 0.040 | 18.0 | |
| $P_2O_5$ | 0.023 | 0.003 | 12.2 | 0.020 | 18.5 | |
| Co | 89 | 2.2 | 2.5 | 88 | 1.8 | |
| Ni | 829 | 27.5 | 3.3 | 887 | −6.6 | |
| Cu | 49 | 7.8 | 16.0 | 42 | 16.7 | heterogeneous |
| Rb | 0.81 | 0.04 | 5.2 | 0.75 | 8.4 | |
| Sr | 15.8 | 0.6 | 3.9 | 15.6 | 1.0 | |
| Y | 8.4 | 0.3 | 3.6 | 8.8 | −4.6 | |
| Zr | 16.0 | 2.6 | 16.3 | 14.9 | 7.7 | heterogeneous |
| Nb | 0.33 | 0.01 | 2.8 | 0.32 | 4.6 | |
| Cs | 0.18 | 0.01 | 6.0 | 0.16 | 10.1 | |
| Ba | 6.9 | 0.7 | 9.5 | 6.0 | 15.1 | |
| La | 0.42 | 0.02 | 4.0 | 0.39 | 9.9 | |
| Ce | 1.28 | 0.04 | 3.1 | 1.23 | 4.8 | |
| Pr | 0.24 | 0.01 | 5.5 | 0.22 | 7.7 | |
| Nd | 1.48 | 0.06 | 4.4 | 1.45 | 1.9 | |
| Sm | 0.70 | 0.03 | 4.5 | 0.70 | −0.3 | |
| Eu | 0.29 | 0.01 | 3.1 | 0.28 | 3.8 | |
| Gd | 1.09 | 0.06 | 5.5 | 1.14 | −4.8 | |
| Tb | 0.21 | 0.01 | 3.5 | 0.21 | −1.5 | |
| Dy | 1.46 | 0.07 | 4.5 | 1.46 | 0.0 | |
| Ho | 0.31 | 0.01 | 4.3 | 0.32 | −2.9 | |

| | | | | | |
|---|---|---|---|---|---|
| Er | 0.97 | 0.03 | 3.5 | 1.01 | −3.5 |
| Yb | 0.92 | 0.04 | 3.8 | 0.91 | 0.6 |
| Lu | 0.13 | 0.01 | 5.8 | 0.14 | −5.1 |
| Hf | 0.48 | 0.04 | 9.2 | 0.48 | 1.5 |
| Ta | 0.018 | 0.002 | 12.1 | 0.018 | 3.5 |
| Pb | 0.22 | 0.02 | 8.0 | 0.21 | 5.1 |
| Th | 0.029 | 0.006 | 19.1 | 0.027 | 8.3 |
| U | 0.010 | 0.002 | 19.3 | 0.011 | −3.5 |

***Table S-5.*** *Whole-rock XRF and ICP-MS results for pelagic sediments DSDP 595/596*

| Sample | Depth (mbsf) | Type | $SiO_2$ (wt%) | $TiO_2$ (wt%) | $Al_2O_3$ (wt%) | $Fe_2O_3$ (wt%) | MnO (wt%) | MgO (wt%) | CaO (wt%) | $Na_2O$ (wt%) | $K_2O$ (wt%) | $P_2O_5$ (wt%) | Co (µg/g) | Ni (µg/g) | Cu (µg/g) |
|---|---|---|---|---|---|---|---|---|---|---|---|---|---|---|---|
| 595A_1 | 0.10 | Pelagic clay | 44.3 | 0.903 | 15.4 | 10.2 | 1.12 | 2.74 | 2.40 | 5.33 | 2.15 | 0.265 | 111 | 115 | 223 |
| 595A_2A | 1.25 | Pelagic clay | 39.3 | 0.799 | 13.8 | 8.56 | 1.04 | 2.60 | 1.98 | 5.03 | 2.17 | 0.215 | 114 | 129 | 219 |
| 595A_3 | 3.50 | Pelagic clay | 42.5 | 0.746 | 15.3 | 8.48 | 1.21 | 2.04 | 1.80 | 5.65 | 2.93 | 0.238 | 124 | 86.0 | 220 |
| 595A_4 | 6.45 | Pelagic clay | 36.4 | 0.601 | 11.7 | 10.1 | 3.81 | 2.91 | 4.10 | 4.71 | 1.92 | 0.873 | 373 | 443 | 378 |
| 595A_5 | 12.90 | Pelagic clay | 37.8 | 0.611 | 12.4 | 6.49 | 3.33 | 3.12 | 5.57 | 5.15 | 2.19 | 1.33 | 373 | 754 | 453 |
| 595A_6 | 14.39 | Pelagic clay | 38.7 | 0.599 | 12.4 | 6.43 | 2.61 | 2.82 | 6.28 | 4.57 | 2.48 | 1.53 | 318 | 516 | 282 |
| 595A_7 | 16.11 | Pelagic clay | 44.9 | 0.556 | 13.6 | 7.31 | 3.06 | 3.00 | 2.27 | 4.46 | 3.15 | 0.508 | 264 | 489 | 333 |
| 595A_8 | 22.50 | Pelagic clay | 43.3 | 0.859 | 13.0 | 7.74 | 2.53 | 3.10 | 2.28 | 4.77 | 2.72 | 0.397 | 225 | 469 | 446 |
| 595A_9 | 24.00 | Pelagic clay | 44.9 | 0.870 | 13.0 | 8.16 | 2.67 | 3.15 | 2.38 | 4.75 | 2.71 | 0.419 | 224 | 488 | 502 |
| 595A_10 | 25.50 | Pelagic clay | 45.4 | 0.806 | 13.4 | 7.29 | 2.35 | 3.25 | 2.53 | 4.62 | 2.43 | 0.459 | 202 | 541 | 635 |
| 595A_11 | 31.54 | Porcellanite-rich pelagic clay | 82.4 | 0.095 | 2.74 | 2.65 | 0.791 | 1.05 | 0.704 | 1.64 | 0.529 | 0.272 | 33.7 | 66.4 | 175 |
| 595A_12 | 37.27 | Porcellanite-rich pelagic clay | 69.3 | 0.105 | 2.97 | 2.82 | 0.763 | 1.18 | 0.711 | 1.77 | 0.531 | 0.252 | 34.9 | 58.2 | 144 |
| 595A_13 | 42.58 | Porcellanite-rich pelagic clay | 83.9 | 0.052 | 1.55 | 1.98 | 0.717 | 0.694 | 0.401 | 1.34 | 0.261 | 0.220 | 17.0 | 72.3 | 111 |
| 595A_16 | 58.00 | Porcellanite-rich pelagic clay | 76.0 | 0.152 | 3.40 | 3.20 | 1.25 | 1.18 | 0.871 | 2.32 | 0.736 | 0.267 | 53.0 | 125 | 166 |

***Table S-6.*** *Whole-rock XRF and ICP-MS results for Tongan arc lavas*

| Sample | Location | Type | $SiO_2$ (wt%) | MgO (wt%) | Ba (μg/g) | Pb (μg/g) | Th (μg/g) | As (μg/g) | Sb (μg/g) | Cs (μg/g) | Sm (μg/g) | La (μg/g) |
|---|---|---|---|---|---|---|---|---|---|---|---|---|
| T28A1 | Ata | Basalt | 50.5 | 7.18 | 106 | 1.08 | 0.305 | 1.21 | 0.0201 | 0.0761 | 1.61 | 2.56 |
| T29A2 | Ata | Basalt | 50.5 | 6.61 | 132 | 1.19 | 0.363 | 0.928 | 0.0216 | 0.193 | 1.93 | 3.38 |
| T30A3 | Ata | Basaltic andesite | 52.7 | 4.97 | 138 | 1.21 | 0.280 | 1.22 | 0.0289 | 0.138 | 1.95 | 2.98 |
| T32A5 | Ata | Basalt | 50.7 | 7.36 | 111 | 1.01 | 0.270 | 1.03 | 0.0215 | 0.172 | 1.70 | 2.65 |
| T33A6 | Ata | Basalt | 50.3 | 7.20 | 111 | 1.03 | 0.248 | 1.46 | 0.0253 | 0.174 | 1.68 | 2.69 |
| T35A8-2 | Ata | Basalt | 50.0 | 5.97 | 139 | 1.27 | 0.370 | 0.984 | 0.0230 | 0.216 | 1.96 | 3.43 |
| T36A9 | Ata | Basalt | 50.0 | 6.49 | 133 | 1.14 | 0.344 | 0.888 | 0.0226 | 0.194 | 1.93 | 3.40 |
| T37A10 | Ata | Basalt | 50.1 | 6.64 | 129 | 1.24 | 0.354 | 1.01 | 0.0224 | 0.198 | 1.91 | 3.34 |
| T38A11 | Ata | Basalt | 50.7 | 6.23 | 142 | 1.20 | 0.360 | 1.01 | 0.0322 | 0.182 | 1.98 | 3.53 |
| T39A12 | Ata | Basalt | 51.0 | 6.19 | 129 | 1.15 | 0.298 | 1.02 | 0.0185 | 0.186 | 2.02 | 3.11 |
| T40A13 | Ata | Basalt | 51.0 | 6.13 | 131 | 1.16 | 0.301 | 0.99 | 0.0210 | 0.176 | 2.00 | 3.11 |
| T41A14 | Ata | Basalt | 51.6 | 5.86 | 139 | 1.28 | 0.293 | 1.07 | 0.0233 | 0.209 | 1.95 | 3.18 |
| T42A15 | Ata | Basalt | 51.7 | 5.89 | 140 | 0.99 | 0.335 | 1.12 | 0.0218 | 0.078 | 2.09 | 3.35 |
| T15K1 | Kao | Basaltic andesite | 53.3 | 5.60 | 131 | 1.70 | 0.212 | 2.33 | 0.0429 | 0.215 | 1.75 | 2.17 |
| T16K2 | Kao | Basaltic andesite | 53.4 | 5.44 | 117 | 1.66 | 0.198 | 1.64 | 0.0312 | 0.138 | 2.05 | 2.32 |
| T17K3 | Kao | Basaltic andesite | 53.5 | 5.46 | 117 | 1.65 | 0.195 | 1.55 | 0.0292 | 0.215 | 2.01 | 2.30 |
| T21L2 | Late | Basaltic andesite | 53.5 | 4.43 | 92.0 | 1.72 | 0.142 | 1.46 | 0.0277 | 0.187 | 1.38 | 1.73 |
| T23L4 | Late | Basaltic andesite | 56.2 | 3.30 | 133 | 2.56 | 0.216 | 2.09 | 0.0463 | 0.262 | 1.97 | 2.51 |
| T25L6 | Late | Basaltic andesite | 53.5 | 4.41 | 89.4 | 1.58 | 0.148 | 1.34 | 0.0284 | 0.201 | 1.38 | 1.74 |

| | | | | | | | | | | | | |
|---|---|---|---|---|---|---|---|---|---|---|---|---|
| T26L7 | Late | Basaltic andesite | 53.4 | 4.24 | 93.8 | 2.08 | 0.159 | 1.54 | 0.0351 | 0.218 | 1.45 | 1.84 |
| T27L8 | Late | Basaltic andesite | 56.3 | 3.34 | 131 | 2.45 | 0.209 | 2.33 | 0.0430 | 0.274 | 2.01 | 2.50 |
| T2TF2 | Tofua | Basaltic andesite | 52.9 | 5.76 | 114 | 1.47 | 0.140 | 2.11 | 0.0317 | 0.231 | 1.42 | 1.58 |
| T4TF4 | Tofua | Basaltic andesite | 55.5 | 4.45 | 159 | 2.49 | 0.191 | 2.50 | 0.0569 | 0.332 | 1.77 | 2.00 |
| T7TF7 | Tofua | Basaltic andesite | 53.6 | 4.76 | 136 | 2.27 | 0.171 | 1.83 | 0.0410 | 0.273 | 1.63 | 1.88 |
| T9TF9 | Tofua | Basaltic andesite | 53.9 | 4.79 | 137 | 2.19 | 0.173 | 2.09 | 0.0445 | 0.288 | 1.64 | 1.89 |
| T12TF12 | Tofua | Basaltic andesite | 53.6 | 4.76 | 136 | 2.23 | 0.166 | 2.43 | 0.0407 | 0.208 | 1.62 | 1.86 |
| T14TF14 | Tofua | Basaltic andesite | 53.8 | 4.79 | 135 | 2.01 | 0.165 | 2.35 | 0.0377 | 0.274 | 1.62 | 1.86 |

***Table S-7.*** *Whole-rock XRF results for altered oceanic crust DSDP 595/596*

| Sample | Depth (mbsf) | Type | MgO (wt.%) | CaO (wt.%) |
|---|---|---|---|---|
| 595A_18 | 70.5 | Altered basalt | 5.76 | 13.0 |
| 595A_19 | 71.85 | Altered basalt | 6.16 | 12.1 |
| 595B_21 | 73.6 | Altered basalt | 5.53 | 8.24 |
| 595A_23 | 80.16 | Altered basalt | - | - |
| 595A_24 | 81.64 | Altered basalt | 5.16 | 11.5 |
| 595B_25 | 82.1 | Altered basalt | - | - |
| 595B_28 | 82.15 | Altered basalt | - | - |
| 595B_31 | 97.45 | Altered basalt | - | - |
| 595B_34 | 107.85 | Altered basalt | 4.55 | 6.97 |
| 595B_37 | 118.63 | Altered basalt | 6.09 | 10.5 |

***Table S-8.*** *Whole-rock LA-ICP-MS results for AOC-type eclogites. FeO = $Fe_2O_3$ total.*

| Sample | PF18-20 | PF18-26 | PF18-25a | PF18-25c |
|---|---|---|---|---|
| Location | Zermatt | Zermatt | Zermatt | Zermatt |
| Type | AOC-type eclogite | AOC-type eclogite | AOC-type eclogite | AOC-type eclogite |
| $SiO_2$ (wt%) | 53.2 | 40.1 | 53.7 | 46.6 |
| $TiO_2$ (wt%) | 1.55 | 2.10 | 1.66 | 2.70 |
| $Al_2O_3$ (wt%) | 14.8 | 18.8 | 16.1 | 19.9 |
| FeO (wt%) | 8.02 | 10.7 | 8.61 | 10.3 |
| MnO (wt%) | 0.0922 | 0.212 | 0.161 | 0.203 |
| MgO (wt%) | 11.5 | 15.8 | 4.17 | 0.78 |
| CaO (wt%) | 2.71 | 2.99 | 8.27 | 17.3 |
| $Na_2O$ (wt%) | 5.44 | 2.23 | 6.08 | 0.378 |
| $K_2O$ (wt%) | 0.0230 | 0.0303 | 0.349 | 0.0320 |
| $P_2O_5$ (wt%) | 0.245 | 0.603 | 0.227 | 0.433 |
| Rb (µg/g) | 0.194 | 0.181 | 5.48 | 0.463 |
| Sr (µg/g) | 40.0 | 65.3 | 261 | 1120 |
| Y (µg/g) | 15.5 | 33.2 | 35.6 | 88.7 |
| Zr (µg/g) | 152 | 245 | 197 | 334 |
| Cs (µg/g) | 0.0123 | 0.0473 | 0.0825 | 0.0331 |

| | | | | |
|---|---|---|---|---|
| Ba (µg/g) | 0.558 | 1.69 | 24.6 | 6.60 |
| La (µg/g) | 4.26 | 8.88 | 16.5 | 18.4 |
| Ce (µg/g) | 13.7 | 26.9 | 46.3 | 51.7 |
| Pr (µg/g) | 1.86 | 3.67 | 6.34 | 7.09 |
| Nd (µg/g) | 8.43 | 16.4 | 29.1 | 33.7 |
| Sm (µg/g) | 2.29 | 4.04 | 7.41 | 9.82 |
| Eu (µg/g) | 0.724 | 1.21 | 2.38 | 4.35 |
| Tb (µg/g) | 0.438 | 0.818 | 1.13 | 2.09 |
| Gd (µg/g) | 2.67 | 4.63 | 7.67 | 12.5 |
| Dy (µg/g) | 2.98 | 5.86 | 6.73 | 14.8 |
| Ho (µg/g) | 0.594 | 1.19 | 1.31 | 3.08 |
| Er (µg/g) | 1.88 | 3.50 | 3.80 | 9.05 |
| Yb (µg/g) | 1.94 | 3.26 | 3.56 | 8.10 |
| Lu (µg/g) | 0.281 | 0.454 | 0.524 | 1.075 |
| Hf (µg/g) | 2.86 | 4.36 | 3.83 | 6.33 |
| Ta (µg/g) | 0.411 | 0.530 | 0.429 | 0.667 |
| Pb (µg/g) | 0.134 | 0.577 | 2.57 | 10.0 |
| Th (µg/g) | 0.368 | 0.547 | 0.971 | 0.889 |
| U (µg/g) | 0.122 | 0.263 | 0.375 | 0.737 |

***Table S-9.*** *Whole-rock LA-ICP-MS results for metasediments. FeO = $Fe_2O_3$ total.*

| Sample | Z16TB31a | Z16TB31b | Z18TB20 | C13a | C13b | C11 | COS3 | COS2 | COS7 |
|---|---|---|---|---|---|---|---|---|---|
| Location | Zermatt | Zermatt | Zermatt | Lago di Cignana | Lago di Cignana | Lago di Cignana | Corsica | Corsica | Corsica |
| Type | Grt -schist | Grt -schist | Grt -schist | Mn-rich pelagic metapelite | Mn-rich pelagic metapelite | Mn-rich pelagic metapelite | Mn-rich pelagic metapelite | Pelagic metapelite | Clastic metasediment |
| $SiO_2$ (wt%) | 66.7 | 67.8 | 55.5 | 76.6 | 78.8 | 84.7 | 83.6 | 81.5 | 62.5 |
| $TiO_2$ (wt%) | 0.917 | 1.02 | 0.679 | 0.332 | 0.275 | 0.198 | 0.176 | 0.216 | 0.681 |
| $Al_2O_3$ (wt%) | 14.6 | 15.7 | 13.6 | 9.08 | 6.87 | 5.79 | 3.75 | 5.66 | 16.5 |
| FeO (wt%) | 8.13 | 5.00 | 5.78 | 4.95 | 4.75 | 2.89 | 3.28 | 5.03 | 6.72 |
| MnO (wt%) | 0.114 | 0.061 | 0.172 | 0.550 | 0.364 | 1.72 | 3.86 | 0.263 | 0.0669 |
| MgO (wt%) | 1.79 | 1.61 | 3.04 | 1.33 | 1.97 | 1.20 | 1.06 | 1.33 | 2.64 |
| CaO (wt%) | 4.10 | 4.22 | 10.5 | 6.00 | 6.01 | 0.52 | 1.45 | 1.65 | 2.57 |
| $Na_2O$ (wt%) | 1.11 | 1.37 | 0.588 | 0.879 | 0.604 | 0.290 | 0.893 | 0.270 | 0.763 |
| $K_2O$ (wt%) | 1.07 | 1.39 | 1.98 | 0.037 | 0.021 | 1.61 | 1.10 | 1.55 | 2.24 |
| $P_2O_5$ (wt%) | 0.152 | 0.131 | 0.094 | 0.106 | 0.0994 | 0.0188 | 0.0495 | 0.0785 | 0.0922 |
| Co (µg/g) | 23.3 | 15.8 | 22.0 | 28.03 | 42.8 | 39.6 | 85.4 | 22.8 | 14.5 |
| Ni (µg/g) | 51.2 | 28.4 | 60.1 | 26.08 | 78.4 | 46.3 | 36.1 | 49.7 | 52.5 |
| Cu (µg/g) | 53.3 | 46 | 120 | 148 | 26.9 | 242 | 77.1 | 66.5 | 27.9 |
| Ce (µg/g) | 99.7 | 115 | 50.11 | 32.2 | 41.07 | 27.5 | 30.78 | 36.4 | 75.4 |

***Table S-10.*** *GeoRem preferred values for SCo-1 used for normalization (Jochum et al., 2005).*

| | $SiO_2$ (wt%) | $TiO_2$ (wt%) | $Al_2O_3$ (wt%) | $Fe_2O_3$ (wt%) | MnO (wt%) | MgO (wt%) | CaO (wt%) | $Na_2O$ (wt%) | K2O (wt%) | $P_2O_5$ (wt%) | Mo (µg/g) | Co (µg/g) | Ni (µg/g) | Cu (µg/g) |
|---|---|---|---|---|---|---|---|---|---|---|---|---|---|---|
| SCo-1 | 62.8 | 0.63 | 13.7 | 5.13 | 0.053 | 2.72 | 2.62 | 0.9 | 2.77 | 0.21 | 1.38 | 10.75 | 27 | 29 |

# 2

# Molybdenum isotopes in plume-influenced MORBs reveal recycling of ancient anoxic sediments

**Manuscript published in Geochemical Perspectives Letters**

Ahmad Q., Wille M., Rosca C., Labidi J., Schmid T., Mezger K., and König S. (2022)

Geochemical Perspectives Letters, 23, 43-48.

# Abstract

Under modern oxidizing Earth surface conditions, dehydrated subducted slabs show Mo isotope compositions as low as $\delta^{98/95}$Mo = −1.5 ‰, compared to the depleted mantle $\delta^{98/95}$Mo = −0.2 ‰. Such light Mo isotope compositions reflect the redox-dependent aqueous mobility of isotopically heavy Mo associated with slab dehydration. Here we analyzed basaltic glasses from the South-Mid Atlantic Ridge, whose parental melts are influenced by the enriched Discovery and Shona mantle plumes. We report increasingly higher $\delta^{98/95}$Mo of up to −0.1 ‰ from the most depleted samples towards those tapping more enriched mantle sources. $\delta^{98/95}$Mo values correlate with radiogenic Sr and Nd isotopes, which indicates the recycling of Proterozoic sediments with a Mo isotopic composition that was not affected by subduction-related, oxic dehydration. We propose that the Mo isotope signatures were retained during subduction and reflect anoxic conditions during deep-sea sedimentation in the mid-Proterozoic. Finally, Mo isotope fractionation between different terrestrial reservoirs likely depends on the slab redox budget, and therefore on the timing of subduction with regard to Earth's surface oxygenation.

# Introduction

The quantification of element and isotope fractionation in subduction zones plays an important role in understanding (re)cycling mechanisms between the Earth's surface and its interior over geologic time scales. Element and isotope fractionation in this setting can be controlled by the prevailing redox conditions of the subducted material. As aerobic conditions prevail at the Earth's surface today, deep-sea sediments and altered oceanic crust (AOC) are largely oxidized and influence the redox budget of the subducting slab (e.g., Evans, 2012). It is still unclear whether the redox budget of slabs is directly correlated with the oxygenation of Earth's atmosphere and oceans, and whether the redox state of the Earth's surface influences the behavior of redox-sensitive elements in subduction zone settings through Earth's history.

A particularly suitable element to study the relationship between oxidized and reduced geochemical reservoirs is the redox-sensitive element Mo. The mobility of Mo from the subducted material is controlled by the redox state of slab-derived aqueous fluids and hydrous melts (Bali et al., 2012; Skora et al., 2017). Significant Mo mobilization and isotope fractionation has been observed during the subduction of oxidized lithologies, leaving behind a Mo depleted and isotopically light residual slab (e.g., Freymuth et al., 2015; König et al., 2016; Chen et al., 2019; Ahmad et al., 2021). Under reducing conditions, only limited Mo mobility is expected to occur in subducted lithologies (Bali et al., 2012; Skora et al., 2017) thus preserving pre-subducted Mo signatures of the surface. This redox dependent mobilization of Mo during subduction metamorphism potentially allows reconstructing the redox budget of ancient subduction zones through Mo isotope compositions of mantle-derived material enriched by ancient recycled crustal components.

This study investigates Mo isotope systematics in a well-characterized basaltic sample suite from the South Mid-Atlantic ridge (S-MAR) that shows evidence for interaction with the enriched Shona and Discovery mantle plumes (see Supplementary Information for further details, Fig. S-1). Previous studies on these samples suggested the recycling of ancient oceanic crust and sediments in their mantle source with an age between 1 and 2 Ga based on radiogenic isotopes, and the absence of mass independent fractionation of S isotopes (Douglass et al., 1999; Andres et al., 2002; Labidi et al., 2013). These basalts additionally feature increasingly heavier S and Se isotope compositions with indicators of mantle source enrichment, and are interpreted to reflect subduction recycling of reduced sediments from a redox stratified Proterozoic ocean (Labidi et al., 2013; Yierpan et al., 2020).

## Results

The $\delta^{98/95}$Mo signatures of S-MAR basaltic glass samples range between −0.24 ‰ and −0.10 ‰. These $\delta^{98/95}$Mo values show correlations with $^{87}$Sr/$^{86}$Sr as well as $^{143}$Nd/$^{144}$Nd, $^{176}$Hf/$^{177}$Hf, and $\delta^{82}$/$^{76}$Se (Figs. 1, S-4a,b). The correlations indicate that Mo isotopes trace mantle source enrichment. The range in $\delta^{98/95}$Mo of the samples is similar to that of MORBs (and seamounts) from the East Pacific Rise (EPR), the Pacific-Antarctic ridge (PAR), and the Mohns Knipovich ridge (MKR; Figs. 1, S-2). However, the samples from the S-MAR show a much larger variability in $^{87}$Sr/$^{86}$Sr and $^{143}$Nd/$^{144}$Nd and more systematic source enrichments (Figs. 1, S-2, S-4a,b).

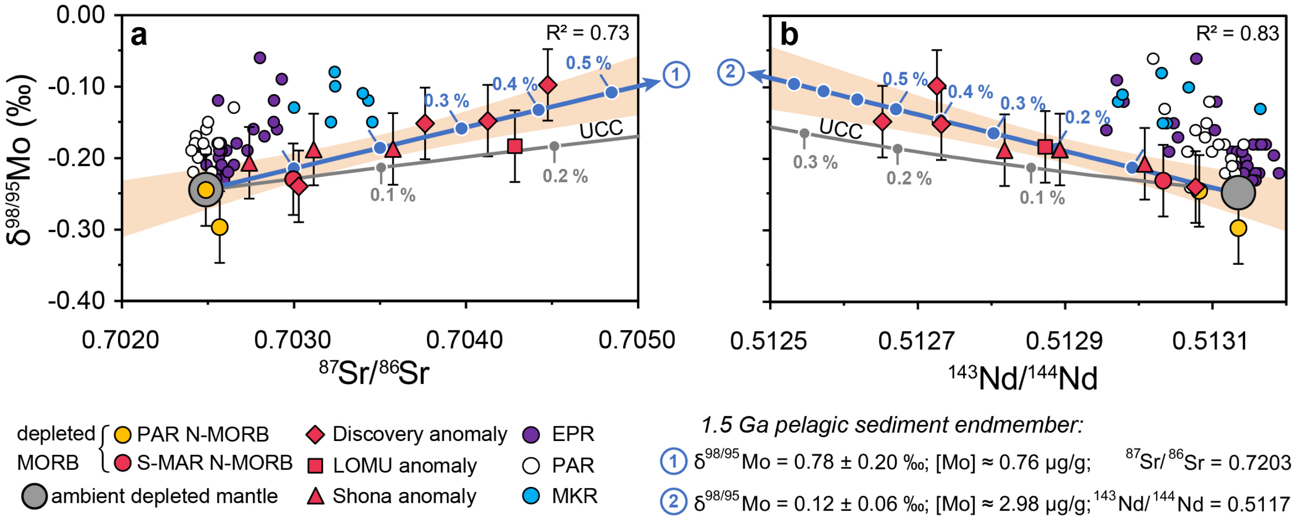

***Figure 1.*** *Covariation diagram of MORBs. (a) $\delta^{98/95}$Mo vs. $^{87}$Sr/$^{86}$Sr; (b) $\delta^{98/95}$Mo vs. $^{143}$Nd/$^{144}$Nd. Mixing of a 1.5 Ga old pelagic sediment end member (best fit parameters from linear regression) with the ambient depleted mantle (see Table S-2 for mixing parameters). Mixing with upper continental crust (UCC) is plotted for comparison. External reproducibility on each isotope value is considered for regression, and the shaded area indicates a 95 % CI error envelope. PAR samples are excluded from the regression. Error bars indicate 2 SD external reproducibility.*

***Table 1.*** *Average Mo isotope composition of MORBs from the S-MAR and PAR together with radiogenic isotope data (Douglass et al., 1999) and Se isotope compositions (Yierpan et al., 2020). Individual measurements are listed in Table S-1.*

| Sample | Type | $\delta^{98/95}$Mo (‰)$^A$ | *n* | $\delta^{82/76}$Se (‰)$^B$ | $^{87}$Sr/$^{86}$Sr | $^{143}$Nd/$^{144}$Nd |
|---|---|---|---|---|---|---|
| *Southern Mid-Atlantic ridge* | | | | | | |
| EW9309 40D-1g | Depleted N-MORB | −0.231 | 3 | −0.18 | 0.702997 | 0.513033 |
| EW9309 33D-1g | Discovery influenced MORB (North) | −0.098 | 3 | −0.03 | 0.704475 | 0.512726 |
| EW9309 28D-1g | Discovery influenced MORB (North) | −0.239 | 2 | −0.14 | 0.703028 | 0.513077 |
| EW9309 2D-1g | Discovery influenced MORB (South) | −0.148 | 2 | −0.08 | 0.704127 | 0.512652 |
| EW9309 4D-3g | Discovery influenced MORB (South) | −0.152 | 3 | −0.04 | 0.703762 | 0.512732 |
| EW9309 9D-3g | LOMU MORB | −0.183 | 2 | −0.03 | 0.704284 | 0.512873 |
| EW9309 15D-1g | Shona influenced MORB | −0.207 | 2 | −0.13 | 0.702741 | 0.513008 |
| EW9309 21D-1g | Shona influenced MORB | −0.188 | 2 | −0.12 | 0.703115 | 0.512818 |
| EW9309 22D-3g | Shona influenced MORB | −0.187 | 2 | −0.08 | 0.703576 | 0.512893 |
| *Pacific-Antarctic ridge* | | | | | | |
| PAC2 DR3 3-1 | Depleted N-MORB | −0.245 | 3 | −0.15 | 0.702488 | 0.513082 |
| PAC1 CV-02g | Depleted N-MORB | −0.297 | 3 | −0.23 | 0.702568 | 0.513135 |

[A] The external reproducibility (2 SD) is 0.05 ‰ (see Supplementary Information for further details on the analytical method).

[B] The external reproducibility (2 SD) is 0.08 ‰, except for EW9309 2D-1g and EW9309 9D-3g, for which it is 0.04 ‰ (Yierpan et al., 2020).

# Discussion

## Origin of enriched mantle component.

Combined element and isotope systematics of S-MAR samples strongly suggest that secondary mantle melting processes (such as sulfide melt segregation and fractional crystallization), or seawater alteration, are unlikely the causes for the observed Mo isotope variations. This is because all these processes would have obliterated any correlation between Mo isotope composition and radiogenic isotopes (see Supplementary Information for further discussion). Low degree melting of mantle plume material has been suggested to affect the geochemical signatures of investigated samples (le Roux et al., 2002a), and might have affected their $\delta^{98/95}$Mo (e.g., Chen et al., 2022). We argue that this process did not result in a first order modification of the enriched source signatures of our samples. Their distinct radiogenic isotope compositions, their covariation with stable Se and S signatures, and trace element systematics are independent of partial melting variations, suggesting the plume source was enriched prior to low degree mantle melting (le Roux et al., 2002a; Labidi et al., 2013; Yierpan et al., 2020). Moreover, the absence of a covariation of $\delta^{98/95}$Mo and Pb isotopes (Fig. S-4c,d) does not support the influence of an ancient low degree melt (Chen et al., 2022). Rather, a recycled sediment component can explain the Pb isotope signature of LOMU-affinity samples (cf. Douglass et al., 1999; Andres et al., 2002). In addition, mantle melting degrees of 2.5 % (le Roux et al., 2002a) cannot explain the observed variations of $\delta^{98/95}$Mo indicating that heavy Mo is likely a characteristic primary signature of the enriched plume material (see Supplementary Information for further details). Previous studies attributed this source enrichment to the influence of a recycled component, such as delaminated subcontinental lithospheric mantle, lower continental crust, or subducted sediment (±AOC) (Douglass et al., 1999; Andres et al., 2002; le Roux et al., 2002b). In line with previous investigations showing covariations between other redox-sensitive stable Se-S isotope systematics and radiogenic isotopes (Labidi et al., 2013; Yierpan et al., 2020), we suggest that a sediment contribution to the S-MAR mantle source is the most likely scenario for the observed heavy Mo isotope enrichment in our samples (see Supplementary Information for further discussion). This sedimentary source was previously inferred to have a mid-Proterozoic age (1 to 2 Ga; Douglass et al., 1999; Andres et al., 2002; Labidi et al., 2013; Yierpan et al., 2020).

## Mobility of Mo during subduction: the role of $fO_2$

Recycled Proterozoic sediments that enriched the S-MAR mantle source with isotopically heavy Mo are in stark contrast to inferred, isotopically light Mo in dehydration residues of subducted Phanerozoic metasediments (Ahmad et al., 2021). The trend towards higher observed (co-) variations of $\delta^{98/95}$Mo with increasing degrees of mantle source enrichment within the S-MAR suite therefore implies recycling of a sedimentary $\delta^{98/95}$Mo or even a total Mo budget unaffected by dehydration and melting during subduction. This may be reconciled with experimental studies showing the immobility of Mo in low $fO_2$-bearing slab fluids and hydrous slab melts (Bali et al., 2012; Skora et al., 2017; Chowdhury et al., 2022). These experiments were conducted at subduction zone P-T and at reducing conditions, and showed that $Mo^{4+}$ is immobile in fluids in the presence of rutile (Bali et al., 2012) and mobilization of Mo is inefficient in melts due to increased partitioning of $Mo^{4+}$ relative to $Mo^{6+}$ into the residual phases such as sulfides or rutile (Skora et al., 2017; Chowdhury et al., 2022). These findings are also consistent with the subduction of organic matter (OM)-rich black shales in the Lesser Antilles Arc, where lavas south of Martinique exhibit high $\delta^{98/95}$Mo along with lower Mo/Ce (Freymuth et al., 2016; Gaschnig et al., 2017), suggesting the minute contribution of unfractionated slab-derived Mo to the mantle sources relative to melts originating from more oxidizing sediments. Therefore, significant loss of heavy Mo during subduction metamorphism did not occur in the enriched mantle source component. This would have resulted in a preferential loss of more incompatible (isotopically heavy) $Mo^{6+}$ during melting and dehydration (e.g., Chen et al., 2019; McCoy-West et al., 2019) and would shift $\delta^{98/95}$Mo of the residual subducted material towards lighter values. The interpretation is in line with the $fO_2$-sensitive stable isotope systematics of S and Se (Table 1), which indicate negligible mobilization and isotope fractionation during subduction (Labidi et al., 2013; Yierpan et al., 2020). It is noteworthy that in some cases, that do not apply here, sediments may also buffer subduction zone fluids towards oxidizing conditions, such as Fe- and Mn-rich (meta)sediments that show a high metamorphic $fO_2$ (Ague et al., 2022 and references therein). Yet, our S-MAR data can be attributed to an immobile behavior of Mo with unchanged $\delta^{98/95}$Mo under reducing conditions, which is in sharp contrast with the mobility of Mo under oxidizing conditions where prograde subduction metamorphism can cause Mo mobilization and alter the primary slab Mo isotope signature.

## Recycled sediments from an anoxic deep ocean

The $\delta^{98/95}$Mo-$^{87}$Sr/$^{86}$Sr-$^{143}$Nd/$^{144}$Nd covariations (Fig. 1) in the S-MAR data combined with the previously established model of the linear $\delta^{34}$S-$\delta^{82}$Se-$^{87}$Sr/$^{86}$Sr(-$^{143}$Nd/$^{144}$Nd) relationship (Labidi et al., 2013; Yierpan et al., 2020) allows extrapolation of $\delta^{98/95}$Mo and [Mo] to constrain the nature of the recycled sediment. Extrapolation of the linear regression to a model composition of 1.5 Ga old sediment ($^{87}$Sr/$^{86}$Sr = 0.7203, $^{143}$Nd/$^{144}$Nd = 0.5117; Fig. 1, see Table S-2 for details) yields two vastly different end member Mo signatures with $\delta^{98/95}$Mo of 0.78 ± 0.20 ‰ and 0.12 ± 0.06 ‰, and [Mo] of ~0.76 µg/g and 2.98 µg/g, respectively (see blue mixing lines in Fig. 1). This indicates that the linear extrapolation might not sufficiently constrain the Mo composition of the recycled sediment source. Considering the present day $^{87}$Sr/$^{86}$Sr and $^{143}$Nd/$^{144}$Nd model composition of 1.5 Ga old subducted sediment, the isotopic variations of the samples represent only a small fraction of the mixing space between the ambient depleted mantle and recycled sediment. Therefore, for given radiogenic Nd and Sr signatures of the sedimentary component, different $\delta^{98/95}$Mo and [Mo] combinations can potentially result in a minimum least squares error between the mixing model and the S-MAR data. As both variables cannot be independently constrained, a misfit function (see Supplementary Information for details) was applied to calculate the sedimentary $\delta^{98/95}$Mo and [Mo] that represent the measured $\delta^{98/95}$Mo-$^{87}$Sr/$^{86}$Sr-$^{143}$Nd/$^{144}$Nd covariation best (Fig. 2).

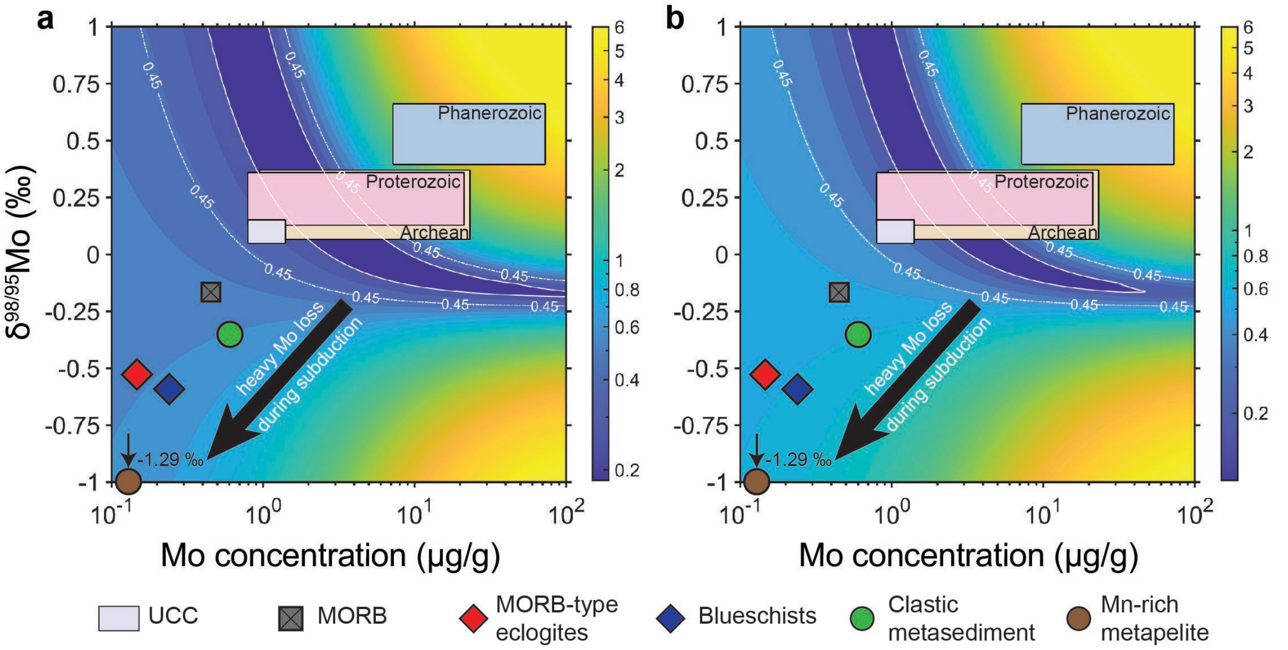

***Figure 2.*** *Least squares error ($\Delta^{98/95}$Mo in ‰; up to 6 ‰) between calculated mixing lines and analyzed samples. Variables are the $\delta^{98/95}$Mo and [Mo] values derived from (a) the $\delta^{98/95}$Mo vs. $^{87}$Sr/$^{86}$Sr and (b) the $\delta^{98/95}$Mo vs. $^{143}$Nd/$^{144}$Nd relationship (Fig. 1). Literature values for potential (concentration averaged) recycled lithologies, and anoxic sediments sorted by age intervals are shown for comparison. See Table S-2 and Supplementary Information for references, mixing parameters, and further details.*

Least squares errors for variable $\delta^{98/95}$Mo and [Mo] values for a given 1.5 Ga old sediment with $^{143}$Nd/$^{144}$Nd and $^{87}$Sr/$^{86}$Sr end member values (blue field in Fig. 2) show a similar pattern for both radiogenic isotope systems, which indicates that a mid-Proterozoic pelagic sediment is likely to be a valid end member. Best fits with minimum errors overlap with the lower 1σ of Proterozoic OM-rich sediment data from the literature (Ye et al., 2021; Table S-2) and can also be achieved with a recycled sediment contribution close to that of the UCC (~0.05 to 0.15 ‰; Willbold and Elliott, 2017 and references therein) with slightly higher $\delta^{98/95}$Mo and/or [Mo] values. This points towards a minor authigenic Mo enrichment from seawater or a residual enrichment of Mo (e.g., Kendall et al., 2017) and implies that $\delta^{98/95}$Mo has not been affected by oxic conditions during slab dehydration due to subduction of reducing lithologies (Fig. 2).

These findings support the notion that the deep ocean remained anoxic until the beginning of the Phanerozoic (e.g., Poulton and Canfield, 2011; Stolper and Keller, 2018). The extent of the biological pump in the Proterozoic ocean, where primary productivity in the oxygenated surface ocean was dominated by cyanobacteria, was lower compared to modern oceans and higher primary surface productivity was restricted to marine environments close to continents (Laakso and Schrag, 2019).

This limited the OM flux to the Proterozoic deep ocean and therefore authigenic Mo accumulation from seawater. However, deep ocean anoxic conditions increased OM preservation and burial efficiency (Burdige, 2007). Furthermore, under anoxic conditions with an overall low concentration of dissolved $SO_4^{2-}$ and $MoO_4^{2-}$, neither a significant Mo enrichment from seawater into the sediment nor a significant Mo mobilization during fluid alteration is expected (Lyons et al., 2014). The overall lower OM input to the deep ocean and smaller oceanic Mo reservoir can therefore explain the small authigenic heavy Mo contribution to the recycled mid-Proterozoic deep-sea sediment (Fig. 2). With respect to the much shorter ocean residence time of Mo relative to the average lifetime of an oceanic crust, the S-MAR enriched end member is likely representative for overall reducing conditions during subduction and an average subducted sedimentary Mo signature, which provides a context of deep ocean redox conditions.

## Implications for the sedimentary Mo subduction cycle

Due to the anoxic conditions in the Proterozoic deep ocean, oxidized species of major and minor elements like Fe, S, and Mn, were absent in deep-sea sediments, thus lowering their redox budget/oxidizing capacity compared to present day marine lithologies (e.g., Evans, 2012; Ague et al., 2022). This may also explain the preserved $\delta^{98/95}$Mo of a reduced Proterozoic sediment component recycled into the S-MAR mantle source, in contrast to Neoproterozoic, deep mantle recycling of low $\delta^{98/95}$Mo into mantle plume sources (see also Ma et al., 2022). This is in line with Samoan OIBs, where $\delta^{98/95}$Mo signatures are interpreted as a mixture of isotopically heavy terrigenous sediments ($\delta^{98/95}$Mo ≈ UCC) and isotopically light dehydrated mafic oceanic crust, which reflect the influence of a distinct pool of mid-Proterozoic recycled ocean crust (Gaschnig et al., 2021). Altogether, this indicates that changing Earth surface redox conditions have influenced the $fO_2$ conditions during subduction and the mobility of sedimentary Mo (and by analogy that of other redox-sensitive elements) and hence, the Mo isotope budget between different Earth (silicate) reservoirs. This emphasizes the time- and condition-related variations in Mo mobility during subduction on our planet (Fig. 3). We therefore conclude that the Mo isotope signature of plume-influenced volcanic rocks can be used to reconcile the redox conditions during ancient surface deposition of deep-sea sediments (cf. Gaschnig et al., 2021) as well as during subduction-related prograde metamorphism and the inception of modern subduction.

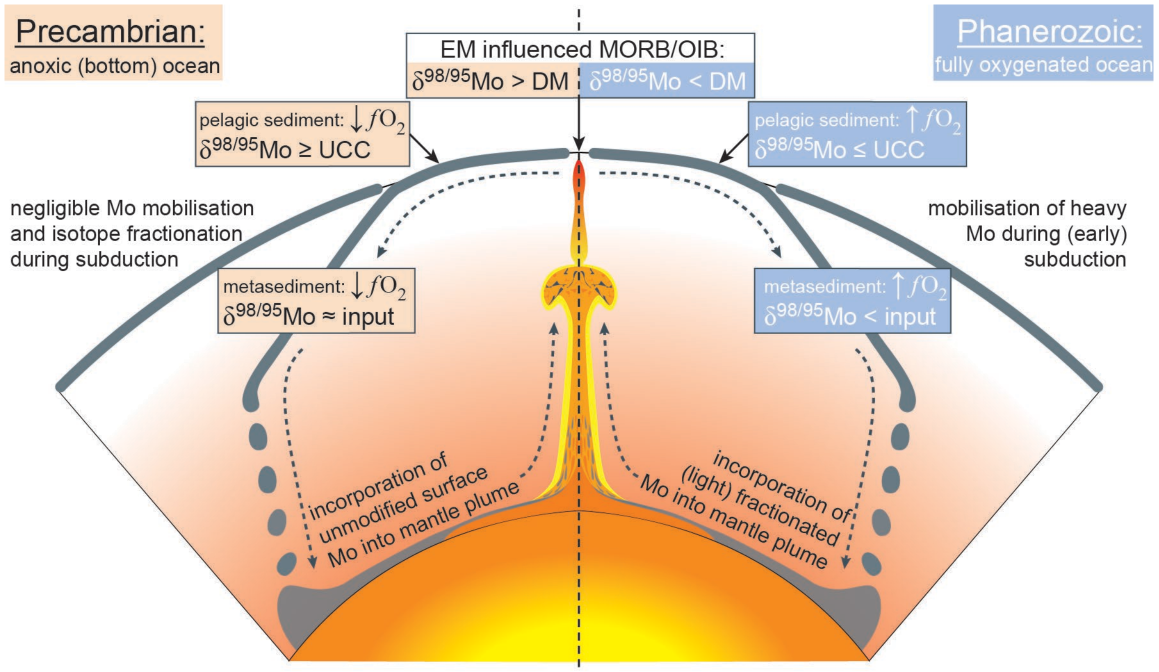

***Figure 3.*** *Illustration of the subducted sedimentary Mo cycle during the Precambrian (left) and Phanerozoic (right). Ddeep-sea sediments carry variable redox budgets influencing Mo mobility and hence isotope fractionation during subduction over Earth's history (see text). UCC, upper continental crust; DM, depleted mantle; EM, enriched mantle.*

## Acknowledgements

This work was funded by the Swiss National Science Foundation, Switzerland (Grant number 182508) to MW. The MC-ICP-MS at the Institute of Geological Sciences, University of Bern used in this study was acquired within the framework of the NCCR project PlanetS (Grant nr. 1NF40-141881) funded by the Swiss National Science Foundation. SK and CR acknowledge ERC Starting Grant 636808 (project O2RIGIN). SK also acknowledges Ramón y Cajal contract RYC2020-030014-I. Jörg Hermann and Paolo Sossi are acknowledged for discussions that contributed to this manuscript. We also wish to thank Alex McCoy-West and two anonymous reviewers for constructive reviews, as well as Helen Williams for editorial handling.

## References

Ague, J.J., Tassara, S., Holycross, M.E., Li, J.-L., Cottrell, E., Schwarzenbach, E.M., Fassoulas, C., John, T. (2022) Slab-derived devolatilization fluids oxidized by subducted metasedimentary rocks. Nature Geoscience 15, 320–326. https://doi.org/10.1038/s41561-022-00904-7

Ahmad, Q., Wille, M., König, S., Rosca, C., Hensel, A., Pettke, T., Hermann, J. (2021) The Molybdenum isotope subduction recycling conundrum: A case study from the Tongan subduction zone, Western Alps and Alpine Corsica. Chemical Geology 576, 120231. https://doi.org/10.1016/j.chemgeo.2021.120231

Andres, M., Blichert-Toft, J., Schilling, J.-G. (2002) Hafnium isotopes in basalts from the southern Mid-Atlantic Ridge from 40°S to 55°S: Discovery and Shona plume–ridge interactions and the role of recycled sediments. Geochemistry, Geophysics, Geosystems 3, 1–25. https://doi.org/10.1029/2002GC000324

Bali, E., Keppler, H., Audetat, A. (2012) The mobility of W and Mo in subduction zone fluids and the Mo–W–Th–U systematics of island arc magmas. Earth and Planetary Science Letters 351–352, 195–207. https://doi.org/10.1016/j.epsl.2012.07.032

Burdige, D.J. (2007) Preservation of Organic Matter in Marine Sediments: Controls, Mechanisms, and an Imbalance in Sediment Organic Carbon Budgets? Chemical Reviews 107, 467–485. https://doi.org/10.1021/cr050347q

Chen, S., Hin, R.C., John, T., Brooker, R., Bryan, B., Niu, Y., Elliott, T. (2019) Molybdenum systematics of subducted crust record reactive fluid flow from underlying slab serpentine dehydration. Nature Communications 10, 4773. https://doi.org/10.1038/s41467-019-12696-3

Chen, S., Sun, P., Niu, Y., Guo, P., Elliott, T., Hin, R.C. (2022) Molybdenum isotope systematics of lavas from the East Pacific Rise: Constraints on the source of enriched mid-ocean ridge basalt. Earth and Planetary Science Letters 578, 117283. https://doi.org/10.1016/j.epsl.2021.117283

Chowdhury, P., Dasgupta, R., Phelps, P.R., Costin, G., Lee, C.-T. A. (2022) Oxygen fugacity range of subducting crust inferred from fractionation of trace elements during fluid-present slab melting in the presence of anhydrite versus sulfide. Geochimica et Cosmochimica Acta 325, 214–231. https://doi.org/10.1016/j.gca.2022.02.030

Douglass, J., Schilling, J.-G., Fontignie, D. (1999) Plume-ridge interactions of the Discovery and Shona mantle plumes with the southern Mid-Atlantic Ridge (40°-55°S). Journal of Geophysical Research: Solid Earth 104, 2941–2962. https://doi.org/10.1029/98JB02642

Evans, K.A. (2012) The redox budget of subduction zones. Earth-Science Reviews 113, 11–32. https://doi.org/10.1016/j.earscirev.2012.03.003

Freymuth, H., Vils, F., Willbold, M., Taylor, R.N., Elliott, T. (2015) Molybdenum mobility and isotopic fractionation during subduction at the Mariana arc. Earth and Planetary Science Letters 432, 176–186. https://doi.org/10.1016/j.epsl.2015.10.006

Freymuth, H., Elliott, T., van Soest, M., Skora, S. (2016) Tracing subducted black shales in the Lesser Antilles arc using molybdenum isotope ratios. Geology 44, 987–990. https://doi.org/10.1130/G38344.1

Gaschnig, R.M., Reinhard, C.T., Planavsky, N.J., Wang, X., Asael, D., Chauvel, C. (2017) The Molybdenum Isotope System as a Tracer of Slab Input in Subduction Zones: An Example From Martinique, Lesser Antilles Arc. Geochemistry, Geophysics, Geosystems 18, 4674–4689. https://doi.org/10.1002/2017GC007085

Gaschnig, R.M., Reinhard, C.T., Planavsky, N.J., Wang, X., Asael, D., Jackson, M.G. (2021) The impact of primary processes and secondary alteration on the stable isotope composition of ocean island basalts. Chemical Geology 581, 120416. https://doi.org/10.1016/j.chemgeo.2021.120416

Kendall, B., Dahl, T.W., Anbar, A.D. (2017) The stable isotope geochemistry of molybdenum. Reviews in Mineralogy and Geochemistry 82, 683–732. https://doi.org/10.2138/rmg.2017.82.16

König, S., Wille, M., Voegelin, A., Schoenberg, R. (2016) Molybdenum isotope systematics in subduction zones. Earth and Planetary Science Letters 447, 95–102. https://doi.org/10.1016/j.epsl.2016.04.033

Laakso, T.A., Schrag, D.P. (2019) A small marine biosphere in the Proterozoic. Geobiology 17, 161–171. https://doi.org/10.1111/gbi.12323

Labidi, J., Cartigny, P., Moreira, M. (2013) Non-chondritic sulphur isotope composition of the terrestrial mantle. Nature 501, 208–211. https://doi.org/10.1038/nature12490

le Roux, P., le Roex, A., Schilling, J.G. (2002a) MORB melting processes beneath the southern Mid-Atlantic Ridge (40–55°S): a role for mantle plume-derived pyroxenite. Contributions to Mineralogy and Petrology 144, 206–229. https://doi.org/10.1007/s00410-002-0376-3

le Roux, P.J., le Roex, A.P., Schilling, J.G., Shimizu, N., Perkins, W.W., Pearce, N.J.G. (2002b) Mantle heterogeneity beneath the southern Mid-Atlantic Ridge: trace element evidence for contamination of ambient asthenospheric mantle. Earth and Planetary Science Letters 203, 479–498. https://doi.org/10.1016/S0012-821X(02)00832-4

Lyons, T.W., Reinhard, C.T., Planavsky, N.J. (2014) The rise of oxygen in Earth's early ocean and atmosphere. Nature 506, 307–315. https://doi.org/10.1038/nature13068

Ma, L., Xu, Y.G., Li, J., Chen, L.-H., Liu, J.-Q., Li, H.-Y., Huang, X.-L., Ma, Q., Hong, L.-B., Wang, Y. (2022) Molybdenum isotopic constraints on the origin of EM1-type continental intraplate basalts. Geochimica et Cosmochimica Acta 317, 255–268. https://doi.org/10.1016/j.gca.2021.11.013

McCoy-West, A.J., Chowdhury, P., Burton, K.W., Sossi, P., Nowell, G.M., Fitton, J.G., Kerr, A.C., Cawood, P.A., Williams, H.M. (2019) Extensive crustal extraction in Earth's early history inferred from molybdenum isotopes. Nature Geoscience 12, 946–951. https://doi.org/10.1038/s41561-019-0451-2

Poulton, S.W., Canfield, D.E. (2011) Ferruginous Conditions: A Dominant Feature of the Ocean through Earth's History. Elements 7, 107–112. https://doi.org/10.2113/GSELEMENTS.7.2.107

Skora, S., Freymuth, H., Blundy, J., Elliott, T., Guillong, M. (2017) An experimental study of the behaviour of cerium/molybdenum ratios during subduction: Implications for tracing the slab component in the Lesser Antilles and Mariana Arc. Geochimica et Cosmochimica Acta 212, 133–155. https://doi.org/10.1016/j.gca.2017.05.025

Stolper, D.A., Keller, C.B. (2018) A record of deep-ocean dissolved O2 from the oxidation state of iron in submarine basalts. Nature 553, 323–327. https://doi.org/10.1038/nature25009

Willbold, M., Elliott, T. (2017) Molybdenum isotope variations in magmatic rocks. Chemical Geology 449, 253–268. https://doi.org/10.1016/j.chemgeo.2016.12.011

Ye, Y., Zhang, S., Wang, H., Wang, X., Tan, C., Li, M., Wu, C., Canfield, D.E. (2021) Black shale Mo isotope record reveals dynamic ocean redox during the Mesoproterozoic Era. Geochemical Perspectives Letters 18, 16–21. https://doi.org/10.7185/geochemlet.2118

Yierpan, A., König, S., Labidi, J., Schoenberg, R. (2020) Recycled selenium in hot spot–influenced lavas records ocean-atmosphere oxygenation. Science Advances 6, abb6179. https://doi.org/10.1126/sciadv.abb6179

# Supplementary Material

## Geochemical Background of the Samples

The studied samples are fresh basaltic glasses that were dredged from the South-Mid Atlantic Ridge (S-MAR) during the RV Maurice Ewing cruise EW93-09 (Douglass et al., 1995, 1999). All samples were well-characterized in terms of radiogenic isotopes (Sr, Nd, Hf, and Pb) (Douglass et al., 1999; Andres et al., 2002), S isotopes (Labidi et al., 2013), Se isotopes (Yierpan et al., 2020), noble gases (Moreira et al., 1995; Sarda et al., 2000), and major and trace element abundances (le Roux et al., 2002a, 2002b, 2002c; Kelley et al., 2013). This makes the selected sample suite ideal for investigating their Mo isotope signature.

The most prominent feature in the S-MAR is the localized interaction between the ambient asthenospheric mantle and the Discovery and Shona mantle plumes (Fig. S-1). A variety of recycled components have been suggested to be incorporated in these mantle plumes based on radiogenic and stable isotope systematics (Fig. S-2; see references above).

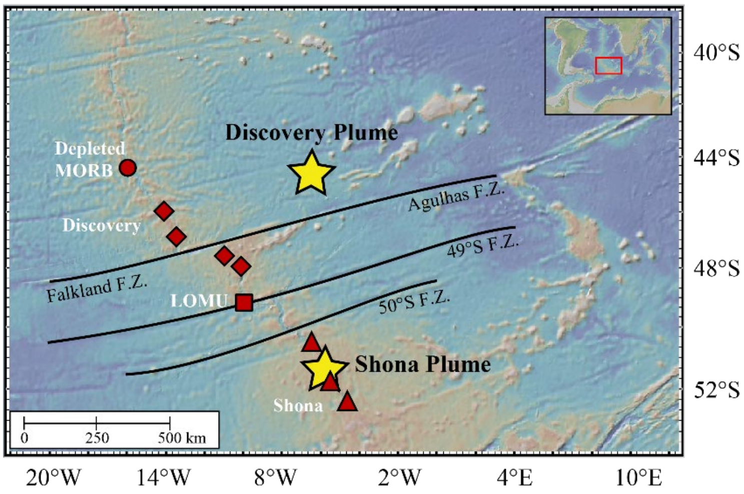

***Figure S-1.*** *Sample locations along the S-MAR together with the Discovery and Shona plume, as well as tectonic fracture zones (F.Z.). Figure made with GeoMapApp (www.geomapapp.org).*

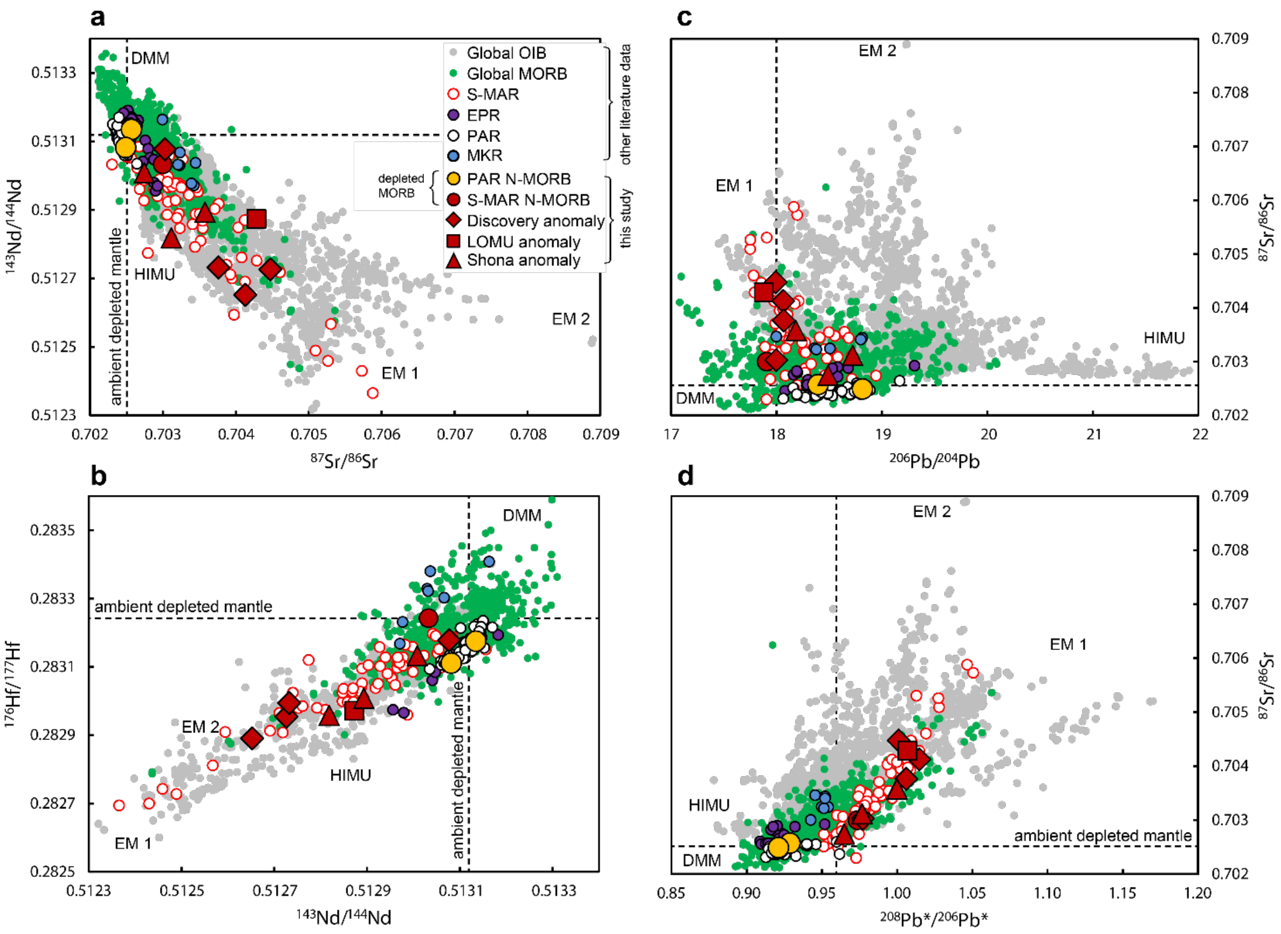

***Figure S-2.*** *Radiogenic isotope data for the studied S-MAR and PAR glasses, modified after Yierpan et al. (2020). Shown for comparison are a global compilation of MORB and OIB (Stracke, 2012 and references therein). MORBs (and seamounts) near the East Pacific Rise (EPR) (Chen et al., 2022 and references therein), Mohns-Knipovich ridges (MKR) (Bezard et al., 2016), and PAR (Hamelin et al., 2011 and references therein) are plotted for comparison. A more detailed precompilation of S-MAR basalts can be found in Labidi et al. (2013). Dashed lines indicate the composition of the S-MAR ambient depleted mantle (Douglass et al., 1999; Andres et al., 2002). In (d),* $^{208}$*Pb**/$^{206}$*Pb* exemplifies the time-integrated Th/U ratios (Stracke, 2012).*

Two additional samples from the Pacific-Antarctic Ridge (PAR) complement existing PAR-MORB Mo isotope data (Bezard et al., 2016). This setting is dominantly sourced by depleted mantle being devoid of any deep mantle plume influence (e.g., Hamelin et al., 2011) with radiogenic Sr and Nd isotope signature similar to the ambient depleted mantle (ADM) constrained for the S-MAR suite (Table S-2; Douglass et al., 1999; Andres et al., 2002).

***Table S-1.*** *Average and individual Mo isotope and elemental data of analyzed MORBs from S-MAR and PAR. MgO and calculated Cl/K are from (le Roux et al., 2002a; Labidi et al., 2013). Individual measurements represent separate sample digestions and chromatographic separations. *Internal precision on a sample run (over 80 cycles) is reported as 2 standard error (2 SE).*

| Sample | Type | Individual measurements | | | Mean values | | | | |
|---|---|---|---|---|---|---|---|---|---|
| | | $\delta^{98/95}$Mo (‰) | 2 SE* (‰) | Mo (µg/g) | $\delta^{98/95}$Mo (‰) | 2 SD (‰) | Mo (µg/g) | MgO (wt. %) | Cl/K |
| *Southern Mid-Atlantic ridge* | | | | | | | | | |
| EW9309 40D-1g | Depleted N-MORB | −0.226 | 0.015 | 0.254 | −0.231 | 0.064 | 0.254 | 8.3 | 0.11 |
| | | −0.201 | 0.022 | 0.255 | | | | | |
| | | −0.265 | 0.02 | 0.254 | | | | | |
| EW9309 33D-1g | Discovery influenced MORB (North) | −0.100 | 0.013 | 1.25 | −0.098 | 0.048 | 1.25 | 7.83 | 0.04 |
| | | −0.073 | 0.02 | 1.25 | | | | | |
| | | −0.121 | 0.013 | 1.25 | | | | | |
| EW9309 28D-1g | Discovery influenced MORB (North) | −0.191 | 0.018 | 0.168 | −0.239 | 0.136 | 0.169 | 8.22 | 0.06 |
| | | −0.287 | 0.018 | 0.17 | | | | | |
| EW9309 2D-1g | Discovery influenced MORB (South) | −0.122 | 0.02 | 0.665 | −0.148 | 0.074 | 0.663 | 6.24 | 0.03 |
| | | −0.174 | 0.014 | 0.661 | | | | | |
| EW9309 4D-3g | Discovery influenced MORB (South) | −0.136 | 0.015 | 0.539 | −0.152 | 0.077 | 0.528 | 7.6 | 0.04 |
| | | −0.124 | 0.02 | 0.527 | | | | | |
| | | −0.195 | 0.016 | 0.517 | | | | | |
| EW9309 9D-3g | LOMU MORB | −0.167 | 0.017 | 0.654 | −0.183 | 0.045 | 0.654 | 8.67 | 0.06 |
| | | −0.199 | 0.015 | 0.654 | | | | | |
| EW9309 15D-1g | Shona influenced MORB | −0.199 | 0.028 | 0.363 | −0.207 | 0.023 | 0.364 | 7.81 | 0.08 |
| | | −0.215 | 0.019 | 0.364 | | | | | |
| EW9309 21D-1g | Shona influenced MORB | −0.179 | 0.027 | 0.587 | −0.188 | 0.024 | 0.586 | 7.1 | 0.05 |
| | | −0.196 | 0.013 | 0.585 | | | | | |
| EW9309 22D-3g | Shona influenced MORB | −0.155 | 0.019 | 1.03 | −0.187 | 0.09 | 1.03 | 4.83 | 0.07 |
| | | −0.219 | 0.017 | 1.03 | | | | | |
| *Pacific-Antarctic ridge* | | | | | | | | | |
| PAC2 DR33-1 | Depleted N-MORB | −0.225 | 0.018 | 0.47 | −0.245 | 0.062 | 0.462 | 6.63 | - |
| | | −0.228 | 0.028 | 0.461 | | | | | |
| | | −0.281 | 0.016 | 0.454 | | | | | |
| PAC1 CV-02g | Depleted N-MORB | −0.249 | 0.016 | 0.213 | −0.297 | 0.116 | 0.215 | 7.74 | - |
| | | −0.280 | 0.031 | 0.213 | | | | | |
| | | −0.361 | 0.021 | 0.218 | | | | | |
| *Rock reference materials* | | | | | | | | | |
| AGV-2 | Andesite | −0.192 | 0.015 | 2.13 | −0.194 | 0.042 | 2.14 | - | - |
| | | −0.211 | 0.019 | 2.11 | | | | | |
| | | −0.179 | 0.012 | 2.19 | | | | | |
| BHVO-2 | Basalt | −0.092 | 0.015 | 3.43 | −0.108 | 0.032 | 3.68 | - | - |
| | | −0.099 | 0.017 | 4.64 | | | | | |
| | | −0.132 | 0.015 | 2.96 | | | | | |
| W-2a | Diabase | −0.100 | 0.018 | 0.462 | −0.087 | 0.053 | 0.452 | - | - |
| | | −0.104 | 0.021 | 0.455 | | | | | |
| | | −0.057 | 0.01 | 0.439 | | | | | |

## Potential Controls on the Mo Isotope Variability of S-MAR Basalts

Observed correlations between $\delta^{98/95}$Mo and $^{143}$Nd/$^{144}$Nd or $^{176}$Hf/$^{177}$Hf (Figs. 1, S-4a) exclude post-emplacement seawater alteration effects on the Mo isotope composition, as seawater incorporation is insensitive to relatively fluid-immobile Nd or Hf (see Labidi et al., 2013). This is also supported by Cl/K ratios close to the range of global MORB (Table S-1) (Labidi et al., 2013). Also unlikely is isotope fractionation due to the segregation of an isotopically heavy sulfide melt at low melting degrees, which results in an isotopically light silicate melt (Liang et al., 2017). The studied samples were sulfide-saturated during melting (Labidi et al., 2013 and references therein), however, there is no correlation between $\delta^{98/95}$Mo and Mo/Ce, with Ce being similarly incompatible during mantle melting but Mo being more compatible in presence of a segregated sulfide melt. Furthermore, a potential sulfide melt segregation would have removed any relationship between $\delta^{98/95}$Mo, and radiogenic isotopes (see Labidi et al., 2013). This covariation together with the lack of covariations between $\delta^{98/95}$Mo and MgO or Mg#, and overall high MgO contents (Table S-1) suggests that also fractional crystallization during differentiation is not the cause of the observed Mo isotope variation (e.g., Voegelin et al., 2014). This is in line with other tholeiitic systems (e.g., Yang et al., 2015; Bezard et al., 2016).

Elemental systematics of S-MAR basalts suggest mixing of the ambient mantle with low-degree melts (F = 2–3 %; le Roux et al., 2002b). Previously, elevated $\delta^{98/95}$Mo in lavas from the EPR (devoid of a mantle plume component) were interpreted to reflect mixing of depleted MORB with an isotopically heavy end member of magmatic origin without the contribution of recycled crustal components (Chen et al., 2022). The authors argued that this heavy end member is an ancient (>1 Ga) low-degree melt (F = 0.2 %) of depleted mantle material that led to an initial fractionation of $\delta^{98/95}$Mo (due to different magmatic compatibilities of Mo$^{4+}$ and Mo$^{6+}$; McCoy-West et al., 2019), similar incompatible elements (e.g., Nb/Zr), and further parent-daughter ratios of radiogenic isotopes. This explains the observed correlation of $\delta^{98/95}$Mo and radiogenic isotopes of Pb, Nd, and Sr (Chen et al., 2022). In the S-MAR sample suite, the trace element ratios are accompanied by radiogenic isotope systematics attributable to an enriched mantle 1 (EM-1) signature requiring a higher initial Rb/Sr, lower Sm/Nd and Lu/Hf, and similar U/Pb compared to DMM (Fig. S-2). These signatures, however, are primary and cannot be explained by low-F melting of plume mantle material (le Roux et al., 2002b). Furthermore, plume-material is pre-enriched in isotopically heavy S and Se prior to low-F melting (Labidi et al., 2013; Yierpan et al., 2020). The question remains, if heavy Mo is primary or if it is generated during low-F mantle melting. If we consider a low-F melting of F = 2.5 % melting (le Roux et al., 2002b) of plume material (T = 1200 °C; Mo$^{6+}$/ΣMo = 0.99), we would expect a maximum isotope shift of $\Delta^{98/95}$Mo$_{max}$

of ~ 0.085 ‰ between pyroxenite melt and DMM (F = 15 %) (McCoy-West et al., 2019). A mixture of both of these end members with 20 % pyroxenite contribution in our heaviest sample EW9309 33D-1g (le Roux et al., 2002b) would lead to a maximum $\Delta^{98/95}\mathrm{Mo}_{\mathrm{max}}$ of 0.059 ‰ (melting model from Wang and Becker, 2018). This value is likely lower ($\Delta^{98/95}\mathrm{Mo}_{\mathrm{max}}$ = 0.040 ‰) when considering lower N-MORB like [Mo] of pyroxenite melts, as there is no covariation of $\delta^{98/95}$Mo and Mo/Ce (Fig. S-5). Moreover, these pyroxenites are formed along the plume-adiabat, which is hotter than the N-MORB adiabat, lowering further the isotopic fractionation induced by low-F melting. Furthermore, we do not observe a correlation of $\delta^{98/95}$Mo with Pb isotopes, which is inconsistent with the increase of U/Pb during ancient low-F melting (Chen et al., 2022). In contrast, we observe LOMU-samples that carry an isotopic heavy signature, which is consistent with an e.g., Proterozoic sediment contribution (e.g., Rehkämper and Hofmann, 1997; Douglass et al., 1999; Andres et al., 2002). As correlations between radiogenic isotopes and $\delta^{34/32}$S, $\delta^{82/76}$Se, and $\delta^{98/95}$Mo (e.g., Fig. 1, S-4b) cannot be explained by magmatic processes or post-emplacement alteration (see Labidi et al., 2013; Yierpan et al., 2019, 2020, 2021), this relationship is in strong support of recycling of enriched mantle components with $\delta^{98/95}$Mo > depleted mantle.

## Origin of Enriched Mantle

Different recycled components (e.g., sub-continental mantle, lower continental crust, oceanic crust, and sediment) in the mantle source of the S-MAR (Douglass et al., 1999; Andres et al., 2002; le Roux et al., 2002c; Labidi et al., 2013; Yierpan et al., 2020) can have an influence on $\delta^{98/95}$Mo of the samples. The Sub-continental mantle can be excluded as a significant component, since worldwide peridotites have a MORB-like $\delta^{98/95}$Mo (–0.206 ± 0.05 ‰; Liang et al., 2017). An aqueous fluid expelled from subducted crust can influence the mantle composition leading to elevated $\delta^{98/95}$Mo and [Mo] (e.g., Ahmad et al., 2021); however, we observe correlations between $\delta^{98/95}$Mo and aqueous fluid-immobile Nd and Hf isotopes (Figs. 1, S-4a) and no covariation is observed with fluid proxies, such as Ba/Th ($R^2$ = 0.1). There is no direct estimate of $\delta^{98/95}$Mo of the lower continental crust (LCC), however, cumulates that possibly reside in the LCC, likely incorporate preferentially light Mo isotopes (Wille et al., 2018; Nebel-Jacobsen et al., 2021) and are unsuitable candidates to explain Mo signatures in the basalt samples. Apart from a clear EM-1 affinity, two samples analyzed here show a trend towards HIMU (Fig. S-2), thus a signature of recycled AOC. However, $^{206}$Pb/$^{204}$Pb ratios do not correlate with $\delta^{98/95}$Mo and most radiogenic $^{206}$Pb/$^{204}$Pb values are accompanied by depleted mantle-like $\delta^{98/95}$Mo (Fig. S-4c). This leads to the conclusion that a significant influence of recycled AOC is unlikely. Furthermore, prograde subduction metamorphism can modify the AOC Mo isotopic signature to lighter values than mantle due to AOC and serpentinite dehydration (Freymuth et al., 2015; Chen et al., 2019), which is also not observed. Oxic sediments are no suitable candidates, as a) oxidized Phanerozoic subducted metasediments are characterized by $\delta^{98/95}$Mo lower than mantle (Ahmad et al., 2021) and b) modeled Mid-Proterozoic sediment recycling ages (Douglass et al., 1999; Andres et al., 2002; Labidi et al., 2013) suggest anoxic deep ocean redox conditions during the Proterozoic (e.g., Lyons et al., 2014). Based on previous stable S and Se studies, the recycled sediment component is likely anoxic and experienced negligible subduction-related S and Se mobilization (Labidi et al., 2013; Yierpan et al., 2020) indicating a stable sedimentary sulfide phase (and potential Mo host) during potential hotter subduction zone conditions in the Proterozoic. This is in line with a previous Mo isotope study on a partially melted Archean eclogite, which indicates stable Mo host phases such as rutile and sulfide (Greaney et al., 2018). Preservation of isotopically heavy Se and Mo in the recycled component further indicates that there was negligible modification by oxidising fluids during anoxic Proterozoic sediment subduction (see König et al., 2021; see discussion in the main text). In line with previous investigations showing covariations between $fO_2$-sensitive stable Se-S isotope systematics and radiogenic isotopes, $\delta^{98/95}$Mo higher than depleted mantle, and overall low Mo mobility during anoxic sediment subduction (see discussion in the main text) we suggest that an anoxic Proterozoic sediment contribution to the S-MAR mantle source is the most likely scenario for the observed heavy Mo isotope enrichment in our samples.

## Analytical Methods

Molybdenum purification and isotope analysis were conducted in the clean laboratory facilities at the Institute of Geological Sciences, University of Bern. For all samples, enough powder was weighed to have 25–50 ng Mo for analysis. The material was spiked with an enriched isotope tracer solution ($^{97}$Mo-$^{100}$Mo double spike). The samples were then dissolved in concentrated single distilled acids in the following sequence: (i) concentrated HF-$HNO_3$ (3:1 mixture), (ii) concentrated $HNO_3$, (iii) 6 M HCl in Savillex™ Teflon vials. The dissolved samples were processed through anion- and cation exchange columns to obtain a clean Mo separate (Wille et al., 2013). In the first step, samples were taken up in 4 M HCl and passed through Dowex 1X8, 200–400 mesh, anion resin. In a second step, the sample material was taken up in 0.5 M HCl and passed through Dowex 50WX8 200–400 mesh, cation exchange resin. Stable Mo isotope measurements were carried out on a Neptune Plus MC-ICP-MS coupled with an Aridus II desolvating nebulizer with an uptake rate of 100–150 $\mu L \cdot min^{-1}$ (details are provided in Ahmad et al., 2021). Six Mo isotopes ($^{94}$Mo, $^{95}$Mo, $^{96}$Mo, $^{97}$Mo, $^{98}$Mo, and $^{100}$Mo) were measured as well as $^{99}$Ru and $^{101}$Ru to monitor potential isobaric interference. We used resistors with $10^{-11}$ Ω to analyze all isotopes except $^{101}$Ru, which was measured using a $10^{-12}$ Ω resistor. For analyses, we have used a combination of 'H' Ni sampler cone and 'X' Ni skimmer cone and obtained ~120

V/ppm on $^{95}$Mo. We used a double spike correction method based on an iterative calculation procedure (see Siebert et al., 2001). The total procedural blank was between 0.22 to 0.65 ng. We present all data in the δ-notation and relative to NIST SRM 3134 in ‰ (Greber et al., 2012; Goldberg et al., 2013) with an interference correction based on $^{99}$Ru:

$$\delta^{98/95}\mathrm{Mo} = \left( \frac{\left(\frac{^{98}\mathrm{Mo}}{^{95}\mathrm{Mo}}\right)_{\mathrm{Sample}}}{\left(\frac{^{98}\mathrm{Mo}}{^{95}\mathrm{Mo}}\right)_{\mathrm{NIST\ SRM\ 3134}}} - 1 \right) * 1{,}000$$

Interference-corrected $\delta^{98/95}$Mo ratios based on $^{99}$Ru and $^{101}$Ru correction were compared to ensure accurate determination of the Ru interference. Background correction was obtained by bracketing samples with measurements of 0.5 M $HNO_3$ carrier solution on-peak. Sample and background analysis consisted of 80 and 30 cycles, respectively, with a signal integration time of 4.194 s for each cycle. Repeated measurements of the standard NIST SRM 3134 and an in-house J&M standard solution lot 602332B gave an isotopic difference of $\Delta^{98/95}$Mo = 0.269 ± 0.017 ‰ (2 SD, n = 14), in agreement with Greber et al. (2012) and Ahmad et al. (2021). Solution standards were measured at a concentration of 25 ppb. Individually digested and chemically purified whole-rock reference materials AGV-2, BHVO-2 and W-2a yielded a $\delta^{98/95}$Mo of −0.19 ± 0.03 ‰ (2 SD, n = 3), −0.11 ± 0.04 ‰ (2 SD, n = 3) and −0.09 ± 0.05 ‰ (2 SD, n = 3), respectively (Table S-1). The values are within uncertainty of those determined previously (e.g., Burkhardt et al., 2014; Willbold et al., 2016; Zhao et al., 2016). Individual measurements of whole rock reference materials (Table S-1) are within the long-term 2 SD external reproducibility of ±0.05 ‰ as determined by previous measurements of BHVO-2 (Ahmad et al., 2021). Including these previous BHVO-2 measurements (−0.09 ± 0.05 ‰, n = 10), we consider ±0.05 ‰ as the long-term 2 SD external reproducibility of our sample measurements. All samples were measured multiple times (after individual digestions and chemical separation) and obtained $\delta^{98/95}$Mo and Mo concentration values were averaged for data presentation and interpretation (Table S-1). All individual sample measurements are within ±0.05 ‰ compared to their average $\delta^{98/95}$Mo, except PAR sample PAC CV-02g.

## Misfit Model

The "linear" Mo-Sr(-Nd) isotope sample array (Fig. 1) represents only a small segment relative to the sediment end member (Table S-2), suggesting that a hyperbolic mixing curve could also account for the observed correlation. Mixing of two components (sediment, 'SED', and ambient depleted mantle end members, 'DM') with different Mo-Sr(-Nd) isotope compositions and concentrations will result in a hyperbola (cf. Vollmer, 1976) of the form:

$$Ax + Bxy + Cy + D = 0$$

where

$$A = a_{\mathrm{DM}} b_{\mathrm{SED}} y_{\mathrm{DM}} - a_{\mathrm{SED}} b_{\mathrm{DM}} y_{\mathrm{SED}}$$

$$B = a_{\mathrm{SED}} b_{\mathrm{DM}} - a_{\mathrm{DM}} b_{\mathrm{SED}}$$

$$C = a_{\mathrm{DM}} b_{\mathrm{SED}} x_{\mathrm{SED}} - a_{\mathrm{SED}} b_{\mathrm{DM}} x_{\mathrm{DM}}$$

$$D = a_{\mathrm{SED}} b_{\mathrm{DM}} x_{\mathrm{DM}} y_{\mathrm{SED}} - a_{\mathrm{DM}} b_{\mathrm{SED}} x_{\mathrm{SED}} y_{\mathrm{DM}}$$

and

$x = {}^{87}\mathrm{Sr}/{}^{86}\mathrm{Sr}$ or ${}^{143}\mathrm{Nd}/{}^{144}\mathrm{Nd}$
$y = \delta^{98/95}\mathrm{Mo}$

$$\left.\begin{array}{l} a_{\mathrm{SED}} = \text{conc. of Mo} \\ b_{\mathrm{SED}} = \text{conc. of } {}^{86}\mathrm{Sr}\ (\sim\mathrm{Sr}) \text{ or } {}^{144}\mathrm{Nd}\ (\sim\mathrm{Nd}) \end{array}\right\} \text{ of the sediment end member with the isotopic composition } (x_{\mathrm{SED}}/y_{\mathrm{SED}})$$

$$\left.\begin{array}{l} a_{\mathrm{DM}} = \text{conc. of Mo} \\ b_{\mathrm{DM}} = \text{conc. of } {}^{86}\mathrm{Sr}\ (\sim\mathrm{Sr}) \text{ or } {}^{144}\mathrm{Nd}\ (\sim\mathrm{Nd}) \end{array}\right\} \text{ of the depleted mantle end member with the isotopic composition } (x_{\mathrm{DM}}/y_{\mathrm{DM}}).$$

By inserting Mo, Sr, and Nd concentrations and isotope compositions from the literature (Table S-2) into above equations, this leads to two unknowns of the sediment end member, $a_{\mathrm{SED}}$ and $y_{\mathrm{SED}}$. By varying $a_{\mathrm{SED}}$ from $a_{\mathrm{SED,\,min}}$ to $a_{\mathrm{SED,\,max}}$ and $y_{\mathrm{SED}}$ from $y_{\mathrm{SED,\,min}}$ to $y_{\mathrm{SED,\,max}}$, a total least squares error can be determined for each $\delta^{98/95}\mathrm{Mo}^{\mathrm{exp}}$ generated at a given ${}^{87}\mathrm{Sr}/{}^{86}\mathrm{Sr}$ or ${}^{143}\mathrm{Nd}/{}^{144}\mathrm{Nd}$ against the observed sample points as:

$$\sum_{i=a_{\mathrm{SED,\,min}}}^{a_{\mathrm{SED,\,max}}} \sum_{j=y_{\mathrm{SED,\,min}}}^{y_{\mathrm{SED,\,max}}} \sqrt{\left(\delta^{98/95}\mathrm{Mo}_{i,j}^{\mathrm{exp}} - \delta^{98/95}\mathrm{Mo}^{\mathrm{sample}}\right)^2}$$

where $a_{\mathrm{SED,\,min}} = 0.1$ µg/g, $a_{\mathrm{SED,\,max}} = 100$ µg/g, $y_{\mathrm{SED,\,min}} = -1$ ‰, and $y_{\mathrm{SED,\,max}} = 1$ ‰.

In the obtained misfit plot (Fig. 2), the best agreement between potential sediment end member and measured samples is given by the least squares error (blue field) of the misfit function. The white dashed line indicates the sample amount multiplied by the external 2 SD reproducibility to obtain a conservative upper limit of model compositions. The white solid line indicates the contour line of the least squares error obtained (see minimum $\Delta^{98/95}$Mo in Fig. 2a, b) added by $\Delta^{98/95}$Mo ≈ 0.1 ‰. For comparison, the compositions of OM-rich sediments sorted by age intervals (Ye et al., 2021; Table S-2), UCC (Greber et al., 2014; Rudnick and Gao, 2014; Voegelin et al., 2014; Freymuth et al., 2015; Willbold and Elliott, 2017; Yang et al., 2017; Greaney et al., 2020;), MORB (Gale et al., 2013; Bezard et al., 2016; Chen et al., 2022;), pelagic Mn-rich and clastic metasediments (Ahmad et al., 2021), and blueschists and MORB-type eclogites (Chen et al., 2019; Ahmad et al., 2021) are plotted (Fig. 2).

Additional scenarios considered for misfit calculations, such as 1 Ga and 2 Ga model sediments, are plotted in Figure S-3 and show least squares errors similar to those in Figure 2. This indicates that a mid-Proterozoic UCC-like sediment with minor authigenic Mo enrichment is a likely sediment end member (see main text).

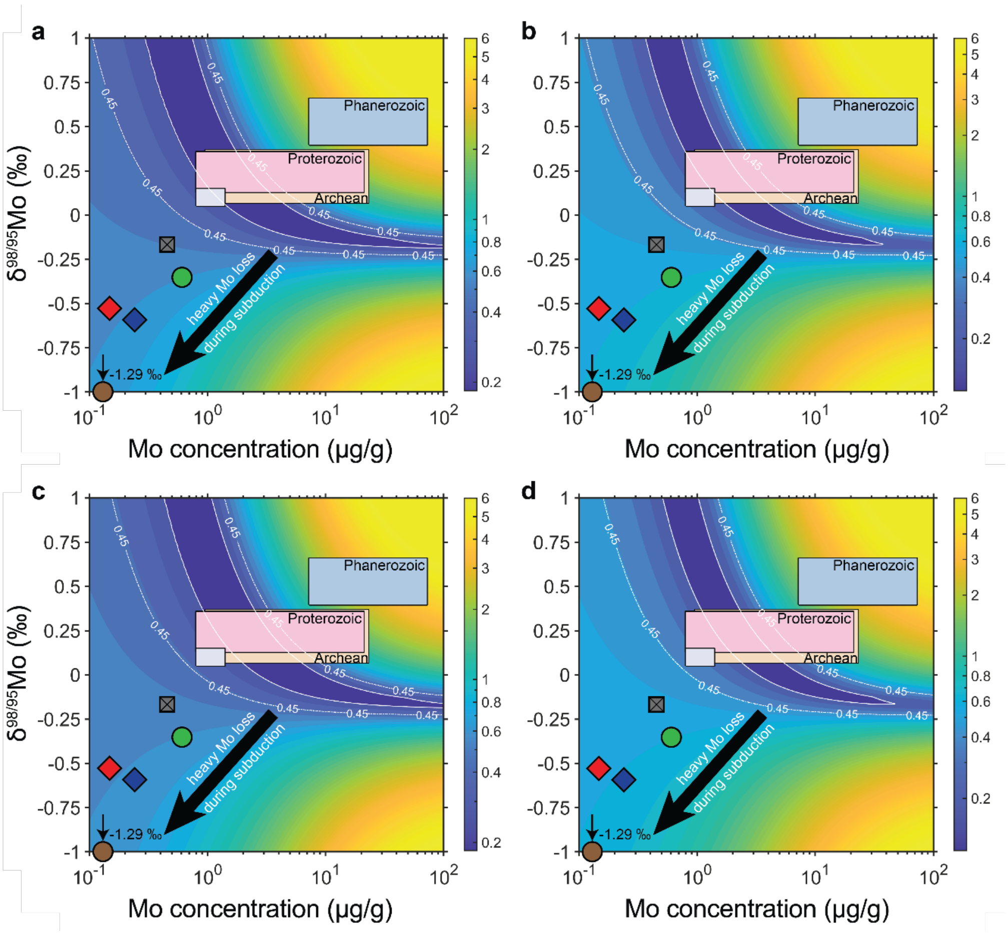

***Figure S-3.*** *Misfit calculation based on mixing parameters reported in Figure 2 and adjusted time-integrated Sr and Nd isotope compositions of the model sediment: (a)* $^{87}$Sr/$^{86}$Sr *(1 Ga) = 0.7173; (b)* $^{143}$Nd/$^{144}$Nd *(1 Ga) = 0.5115; (c)* $^{87}$Sr/$^{86}$Sr *(2 Ga) = 0.7233; (d)* $^{143}$Nd/$^{144}$Nd *(2 Ga) = 0.5119.*

***Table S-2.*** *Parameters from the two-component mixing model (Fig. 2) and compositions of marine sediments.*

| | $\delta^{98/95}$Mo (‰) | [Mo] (µg/g) | $^{87}$Sr/$^{86}$Sr | Sr (µg/g) | $^{143}$Nd/$^{144}$Nd | Nd (µg/g) |
|---|---|---|---|---|---|---|
| *End members* | | | | | | |
| Ambient depleted mantle | −0.245 ± 0.05[A] | 0.025 ± 0.007 | 0.7025 or *0.702488 ± 0.000032* | 9.80 ± 1.86 | 0.51312 or *0.513135 ± 0.00002* | 0.713 ± 0.05 |
| 1.5 Ga old recycled pelagic sediment | 0.78 ± 0.20[B] or *0.12 ± 0.06*[B] | 0.76[B] or *2.98*[B] | 0.7203 | 300 ± 17 | 0.5117 | 85 ± 5.2[C] |
| *Marine sediments*[D] | | | | | | |
| Archean | 0.218 ± 0.150 (*M* = 19, *N* = 417) | $4.70^{+18.4}_{-3.75}$ (*M* = 19, *N* = 744) | | | | |
| Proterozoic | 0.244 ± 0.114 (*M* = 51, *N* = 696) | $4.10^{+17.0}_{-3.30}$ (*M* = 53, *N* = 1262) | | | | |
| Phanerozoic | 0.528 ± 0.132 (*M* = 48, *N* = 882) | $22.9^{+49.7}_{-15.7}$ (*M* = 48, *N* = 1154) | | | | |

The mixing trends are generated using compositions of the Pacific/ambient depleted mantle or the most depleted MORB: PAC2 DR33-1 and PAC1 CV-02g (in italics). Uncertainties on mixing end member elemental concentrations (Rehkämper and Hofmann, 1997; Salters and Stracke, 2004; Labidi et al., 2013; Plank, 2014; Yierpan et al., 2020) and on [Mo]-$\delta^{98/95}$Mo values of the marine sediment compilation (Ye et al., 2021) are all 1σ (except [Mo] uncertainty in depleted mantle, see Salters and Stracke, 2004).

Pelagic sediment and ambient mantle end member isotope compositions (Rehkämper and Hofmann, 1997; Andres et al., 2002; le Roux et al., 2002c; Labidi et al., 2013; Yierpan et al., 2020) are reported with 1σ uncertainties, (except $\delta^{98/95}$Mo uncertainty, which is reported as 2σ). M = number of age averaged data, N = number of different sediment samples from the literature.

[A] The Mo isotope composition of the Pacific-Antarctic Ridge (PAR) basalts can be used as the depleted mantle end member, because their Sr and Nd isotope composition matches the S-MAR ambient depleted mantle isotopic composition determined previously (Douglass et al., 1999; Andres et al., 2002). The Mo isotope composition of the depleted N-MORB DR33-1g ($\delta^{98/95}$Mo = −0.245 ± 0.05 ‰) matches the light isotope composition of Phanerozoic Gorgona komatiites ($\delta^{98/95}$Mo = −0.18 to −0.25 ‰, McCoy-West et al., 2019) and the lighter end of PAR basalts measured previously ($^{98/95}$Mo = −0.06 to −0.24 ‰, excluding the three heavy outliers; Bezard et al., 2016). Because $\delta^{98/95}$Mo values of S-MAR basalts (and MORBs from EPR and PAR, Fig. 1) extend towards slightly lower values (but still within error) compared to the mean depleted mantle estimate (e.g., McCoy-West et al., 2019), we use this lower end of observed literature values for the ambient depleted mantle. The depleted N-MORB CV-02g ($\delta^{98/95}$Mo = −0.297 ± 0.05 ‰), however, represents an outlier being lighter than this range (but still within error) and is excluded in this model.

[B] Obtained best fit parameters from the linear correlation between Mo-Sr isotope and Mo-Nd isotope (italic font) trend and the Mo, Sr, and Nd contents of the depleted mantle and 1.5 Ga pelagic sediment (see above). Note the discrepancy between both $\delta^{98/95}$Mo and [Mo] obtained from both relationships (Fig. 1).

[C] Assigned relative error from GLOSS-II (Plank, 2014) as there was no uncertainty considered for pelagic sediment Nd content.

[D] Marine sediment values of different eons are log-normal means of sediments sorted by age intervals (>1 Myr) from the literature (see the compilation of Ye et al., 2021). The literature data represent mostly shallow-marine (continental shelf/closed basins) sediments from anoxic/euxinic settings, where e.g., sulfate reduction leads to higher authigenic accumulation of isotopically heavy Mo from seawater compared to lower Mo accumulation in the anoxic deep-sea (see main text).

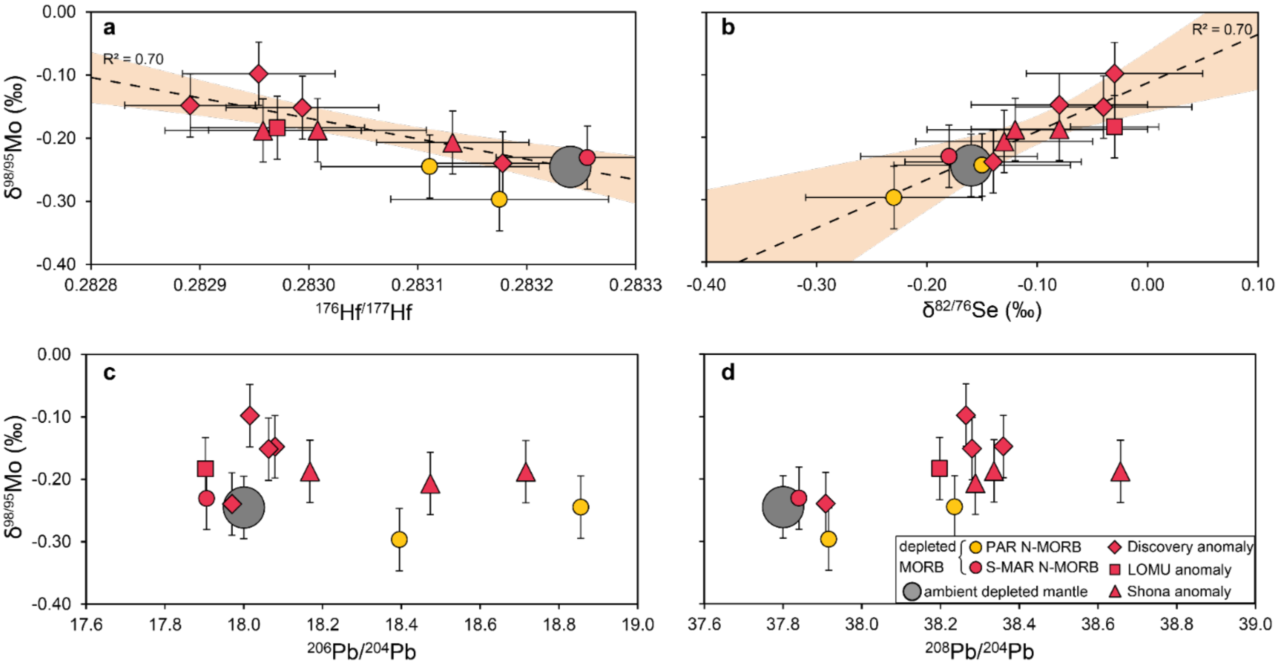

***Figure S-4.*** *Covariation diagram of S-MAR samples with: (a)* $\delta^{98/95}$*Mo vs.* $^{176}$*Hf/*$^{177}$*Hf; (b)* $\delta^{98/95}$*Mo vs.* $\delta^{82}$*Se (c)* $\delta^{98/95}$*Mo vs.* $^{206}$*Pb/*$^{204}$*Pb; and (d)* $\delta^{98/95}$*Mo vs.* $^{208}$*Pb/*$^{204}$*Pb. Error bars indicate 2 SD external reproducibility. External reproducibility on each isotope value is considered for regressions in (a) and (b), and shaded areas indicate 95 % CI error envelope. PAR samples are excluded from the regression. Radiogenic isotopes and Se isotopes for this sample set together with ambient depleted mantle values are from Douglass et al. (1999), Andres et al. (2002), and Yierpan et al. (2020).*

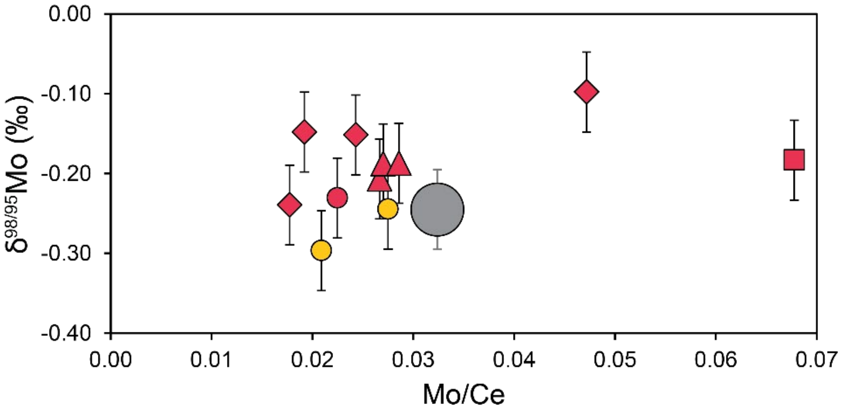

***Figure S-5.*** *Covariation diagram of S-MAR samples with* $\delta^{98/95}$*Mo vs. Mo/Ce. Ce contents of samples and depleted mantle Mo/Ce are from Salters and Stracke (2004) and Kelley et al. (2013).*

## Supplementary Information References

Ahmad, Q., Wille, M., König, S., Rosca, C., Hensel, A., Pettke, T., Hermann, J. (2021) The Molybdenum isotope subduction recycling conundrum: A case study from the Tongan subduction zone, Western Alps and Alpine Corsica. Chemical Geology 576, 120231. https://doi.org/10.1016/j.chemgeo.2021.120231

Andres, M., Blichert-Toft, J., Schilling, J.-G. (2002) Hafnium isotopes in basalts from the southern Mid-Atlantic Ridge from 40°S to 55°S: Discovery and Shona plume–ridge interactions and the role of recycled sediments. Geochemistry, Geophysics, Geosystems 3, 1–25. https://doi.org/10.1029/2002GC000324

Bezard, R., Fischer-Gödde, M., Hamelin, C., Brennecka, G.A., Kleine, T. (2016) The effects of magmatic processes and crustal recycling on the molybdenum stable isotopic composition of Mid-Ocean Ridge Basalts. Earth and Planetary Science Letters 453, 171–181. https://doi.org/10.1016/j.epsl.2016.07.056

Burkhardt, C., Hin, R.C., Kleine, T., Bourdon, B. (2014) Evidence for Mo isotope fractionation in the solar nebula and during planetary differentiation. Earth and Planetary Science Letters 391, 201–211. https://doi.org/10.1016/j.epsl.2014.01.037

Chen, S., Hin, R.C., John, T., Brooker, R., Bryan, B., Niu, Y., Elliott, T. (2019) Molybdenum systematics of subducted crust record reactive fluid flow from underlying slab serpentine dehydration. Nature Communications 10, 4773. https://doi.org/10.1038/s41467-019-12696-3

Chen, S., Sun, P., Niu, Y., Guo, P., Elliott, T., Hin, R.C. (2022) Molybdenum isotope systematics of lavas from the East Pacific Rise: Constraints on the source of enriched mid-ocean ridge basalt. Earth and Planetary Science Letters 578, 117283. https://doi.org/10.1016/j.epsl.2021.117283

Douglass, J., Schilling, J.-G, Kingsley, R.H., Small, C. (1995) Influence of the discovery and Shona mantle plumes on the southern Mid-Atlantic Ridge: Rare earth evidence. Geophysical Research Letters 22, 2893–2896. https://doi.org/10.1029/95GL02665

Douglass, J., Schilling, J.-G., Fontignie, D. (1999) Plume-ridge interactions of the Discovery and Shona mantle plumes with the southern Mid-Atlantic Ridge (40°-55°S). Journal of Geophysical Research: Solid Earth 104, 2941–2962. https://doi.org/10.1029/98JB02642

Freymuth, H., Vils, F., Willbold, M., Taylor, R.N., Elliott, T. (2015) Molybdenum mobility and isotopic fractionation during subduction at the Mariana arc. Earth and Planetary Science Letters 432, 176–186. https://doi.org/10.1016/j.epsl.2015.10.006

Gale, A., Dalton, C.A., Langmuir, C.H., Su, Y., Schilling, J.-G. (2013) The mean composition of ocean ridge basalts. Geochemistry, Geophysics, Geosystems 14, 489–518. https://doi.org/10.1029/2012GC004334

Goldberg, T., Gordon, G., Izon, G., Archer, C., Pearce, C.R., McManus, J., Anbar, A.D., Rehkämper, M. (2013) Resolution of inter-laboratory discrepancies in Mo isotope data: an intercalibration. Journal of Analytical Atomic Spectrometry 28, 724–735. https://doi.org/10.1039/c3ja30375f

Greaney, A.T., Rudnick R.L., Romaniello, S.J., Anbar, A.D. (2018) Completing the Molybdenum Isotope Mass Balance in Subduction Zones. Goldschmidt Abstracts 872. https://goldschmidtabstracts.info/abstracts/abstractView?id=2018001568

Greaney, A.T., Rudnick, R.L., Romaniello, S.J., Johnson, A.C., Gaschnig, R.M., Anbar, A.D. (2020) Molybdenum isotope fractionation in glacial diamictites tracks the onset of oxidative weathering of the continental crust. Earth and Planetary Science Letters 534, 116083. https://doi.org/10.1016/j.epsl.2020.116083

Greber, N.D., Siebert, C., Nägler, T.F., Pettke, T. (2012) δ98/95Mo values and Molybdenum Concentration Data for NIST SRM 610, 612 and 3134: Towards a Common Protocol for Reporting Mo Data. Geostandards and Geoanalytical Research 36, 291–300. https://doi.org/10.1111/j.1751-908X.2012.00160.x

Greber, N.D., Pettke, T., Nägler, T.F. (2014) Magmatic–hydrothermal molybdenum isotope fractionation and its relevance to the igneous crustal signature. Lithos 190–191, 104–110. https://doi.org/10.1016/j.lithos.2013.11.006

Hamelin, C., Dosso, L., Hanan, B.B., Moreira, M., Kositsky, A.P., Thomas, M.Y. (2011) Geochemical portray of the Pacific Ridge: New isotopic data and statistical techniques. Earth and Planetary Science Letters 302, 154–162. https://doi.org/10.1016/j.epsl.2010.12.007

Kelley, K.A., Kingsley, R., Schilling, J.-G. (2013) Composition of plume-influenced mid-ocean ridge lavas and glasses from the Mid-Atlantic Ridge, East Pacific Rise, Galápagos Spreading Center, and Gulf of Aden. Geochemistry, Geophysics, Geosystems 14, 223–242. https://doi.org/10.1002/ggge.20049

König, S., Rosca, C., Kurzawa, T., Varas-Reus, M.I., Dragovic, B., Schoenberg, R., John, T. (2021) Selenium isotope evidence for pulsed flow of oxidative slab fluids. Geochemical Perspectives Letters 17, 27–32. https://doi.org/10.7185/geochemlet.2110

Labidi, J., Cartigny, P., Moreira, M. (2013) Non-chondritic sulphur isotope composition of the terrestrial mantle. Nature 501, 208–211. https://doi.org/10.1038/nature12490

le Roux, P., le Roex, A., Schilling, J.-G. (2002a) Crystallization processes beneath the southern Mid-Atlantic Ridge (40–55°S), evidence for high-pressure initiation of crystallization. Contributions to Mineralogy and Petrology 142, 582–602. https://doi.org/10.1007/s00410-001-0312-y

le Roux, P., le Roex, A., Schilling, J.G. (2002b) MORB melting processes beneath the southern Mid-Atlantic Ridge (40–55°S): a role for mantle plume-derived pyroxenite. Contributions to Mineralogy and Petrology 144, 206–229. https://doi.org/10.1007/s00410-002-0376-3

le Roux, P.J., le Roex, A.P., Schilling, J.G., Shimizu, N., Perkins, W.W., Pearce, N.J.G. (2002c) Mantle heterogeneity beneath the southern Mid-Atlantic Ridge: trace element evidence for contamination of ambient asthenospheric mantle. Earth and Planetary Science Letters 203, 479–498. https://doi.org/10.1016/S0012-821X(02)00832-4

Liang, Y.-H., Halliday, A.N., Siebert, C., Fitton, J.G., Burton, K.W., Wang, K.-L., Harvey, J. (2017) Molybdenum isotope fractionation in the mantle. Geochimica et Cosmochimica Acta 199, 91–111. https://doi.org/10.1016/j.gca.2016.11.023

Lyons, T.W., Reinhard, C.T., Planavsky, N.J. (2014) The rise of oxygen in Earth's early ocean and atmosphere. Nature 506, 307–315. https://doi.org/10.1038/nature13068

McCoy-West, A.J., Chowdhury, P., Burton, K.W., Sossi, P., Nowell, G.M., Fitton, J.G., Kerr, A.C., Cawood, P.A., Williams, H.M. (2019) Extensive crustal extraction in Earth's early history inferred from molybdenum isotopes. Nature Geoscience 12, 946–951. https://doi.org/10.1038/s41561-019-0451-2

Moreira, M., Staudacher, T., Sarda, P., Schilling, J.-G., Allègre, C.J. (1995) A primitive plume neon component in MORB: The Shona ridge-anomaly, South Atlantic (51–52°S). Earth and Planetary Science Letters 133, 367–377. https://doi.org/10.1016/0012-821X(95)00080-V

Nebel-Jacobsen, Y., Wille, M., Ivanic, T., Nebel, O. (2021) Molybdenum isotope systematics in cumulate rock of the 2.8 Windimurra layered intrusion: A test for igneous differentiation and the composition of the Archean mantle. Precambrian Research 355, 106087. https://doi.org/10.1016/j.precamres.2020.106087

Plank, T. (2014) 4.17 - The Chemical Composition of Subducting Sediments. In: Holland, H.D., Turekian, K.K. (Eds.) Treatise on Geochemistry. Second Edition, Elsevier, Oxford, 607–629. https://doi.org/10.1016/B978-0-08-095975-7.00319-3

Rehkämper, M., Hofmann, A.W. (1997) Recycled ocean crust and sediment in Indian Ocean MORB. Earth and Planetary Science Letters 147, 93–106. https://doi.org/10.1016/S0012-821X(97)00009-5

Rudnick, R.L., Gao, S. (2014) 4.1 - Composition of the Continental Crust. In: Holland, H.D., Turekian, K.K. (Eds.) Treatise on Geochemistry. Second Edition, Elsevier, Oxford, 1–51. https://doi.org/10.1016/B978-0-08-095975-7.00301-6

Salters, V.J.M., Stracke, A. (2004) Composition of the depleted mantle. Geochemistry, Geophysics, Geosystems 5, Q05B07. https://doi.org/10.1029/2003GC000597

Sarda, P., Moreira, M., Staudacher, T., Schilling, J.-G., Allègre, C.J. (2000) Rare gas systematics on the southernmost Mid-Atlantic Ridge: Constraints on the lower mantle and the Dupal source. Journal of Geophysical Research: Solid Earth 105, 5973–5996. https://doi.org/10.1029/1999JB900282

Siebert, C., Nägler, T.F., Kramers, J.D. (2001) Determination of molybdenum isotope fractionation by double-spike multicollector inductively coupled plasma mass spectrometry. Geochemistry, Geophysics, Geosystems 2, 2000GC000124. https://doi.org/10.1029/2000GC000124

Stracke, A. (2012) Earth's heterogeneous mantle: A product of convection-driven interaction between crust and mantle. Chemical Geology 330–331, 274–299. https://doi.org/10.1016/j.chemgeo.2012.08.007

Voegelin, A.R., Pettke, T., Greber, N.D., von Niederhäusern, B., Nägler, T.F. (2014) Magma differentiation fractionates Mo isotope ratios: Evidence from the Kos Plateau Tuff (Aegean Arc). Lithos 190–191, 440–448. https://doi.org/10.1016/j.lithos.2013.12.016

Vollmer, R. (1976) Rb-Sr and U-Th-Pb systematics of alkaline rocks: the alkaline rocks from Italy. Geochimica et Cosmochimica Acta 40, 283–295. https://doi.org/10.1016/0016-7037(76)90205-2

Wang, Z., Becker, H. (2018) Molybdenum partitioning behavior and content in the depleted mantle: Insights from Balmuccia and Baldissero mantle tectonites (Ivrea Zone, Italian Alps). Chemical Geology 499, 138–150. https://doi.org/10.1016/j.chemgeo.2018.09.023

Willbold, M., Elliott, T. (2017) Molybdenum isotope variations in magmatic rocks. Chemical Geology 449, 253–268. https://doi.org/10.1016/j.chemgeo.2016.12.011

Willbold, M., Hibbert, K., Lai, Y.-J., Freymuth, H., Hin, R.C., Coath, C., Vils, F., Elliott, T. (2016) High-Precision Mass-Dependent Molybdenum Isotope Variations in Magmatic Rocks Determined by Double-Spike MC-ICP-MS. Geostandards and Geoanalytical Research 40, 389–403. https://doi.org/10.1111/j.1751-908X.2015.00388.x

Wille, M., Nebel, O., Van Kranendonk, M.J., Schoenberg, R., Kleinhanns, I.C., Ellwood, M.J. (2013) Mo–Cr isotope evidence for a reducing Archean atmosphere in 3.46–2.76 Ga black shales from the Pilbara, Western Australia. Chemical Geology 340, 68–76. https://doi.org/10.1016/j.chemgeo.2012.12.018

Wille, M., Nebel, O., Pettke, T., Vroon, P.Z., König, S., Schoenberg, R. (2018) Molybdenum isotope variations in calc-alkaline lavas from the Banda arc, Indonesia: Assessing the effect of crystal fractionation in creating isotopically heavy continental crust. Chemical Geology 485, 1–13. https://doi.org/10.1016/j.chemgeo.2018.02.037

Yang, J., Siebert, C., Barling, J., Savage, P., Liang, Y.-H., Halliday, A.N. (2015) Absence of molybdenum isotope fractionation during magmatic differentiation at Hekla volcano, Iceland. Geochimica et Cosmochimica Acta 162, 126–136. https://doi.org/10.1016/j.gca.2015.04.011

Yang, J., Barling, J., Siebert, C., Fietzke, J., Stephens, E., Halliday, A.N. (2017) The molybdenum isotopic compositions of I-, S- and A-type granitic suites. Geochimica et Cosmochimica Acta 205, 168–186. https://doi.org/10.1016/j.gca.2017.01.027

Ye, Y., Zhang, S., Wang, H., Wang, X., Tan, C., Li, M., Wu, C., Canfield, D.E. (2021) Black shale Mo isotope record reveals dynamic ocean redox during the Mesoproterozoic Era. Geochemical Perspectives Letters 18, 16–21. https://doi.org/10.7185/geochemlet.2118

Yierpan A., König S., Labidi J., Schoenberg R. (2019) Selenium isotope and S-Se-Te elemental systematics along the Pacific-Antarctic ridge: Role of mantle processes. Geochimica et Cosmochimica Acta 249, 199–224. https://doi.org/10.1016/j.gca.2019.01.028

Yierpan, A., König, S., Labidi, J., Schoenberg, R. (2020) Recycled selenium in hot spot–influenced lavas records ocean-atmosphere oxygenation. Science Advances 6, abb6179. https://doi.org/10.1126/sciadv.abb6179

Yierpan A., Redlinger J., König S., (2021) Selenium and tellurium in Reykjanes Ridge and Icelandic basalts: Evidence for degassing-induced Se isotope fractionation. Geochimica et Cosmochimica Acta 313, 155–172. https://doi.org/10.1016/j.gca.2021.07.029

Zhao, P.-P., Li, J., Zhang, L., Wang, Z.-B., Kong, D.-X., Ma, J.-L., Wei, G.-J., Xu, J.-F. (2016) Molybdenum Mass Fractions and Isotopic Compositions of International Geological Reference Materials. Geostandards and Geoanalytical Research 40, 217–226. https://doi.org/10.1111/j.1751-908X.2015.00373.x

# 3

# Heavy Mo in the Pitcairn plume and global implications for the subduction cycle of anoxic sediments

Ahmad Q., Wille M., Labidi J., Devey C., König S., and Mezger K.

## Abstract

Subduction-related processes influence the solid Earth's principal geochemical reservoirs by redistributing elements during Earth's evolution. These processes affect the chemical composition of Earth's mantle, crust, atmosphere, and hydrosphere, and consequently have an impact on the evolution of life itself. Subduction of surface material, which has been geochemically modified by low-temperature processes, leads to mineralogical and chemical heterogeneities in mantle reservoirs. One of the geochemical end members of the heterogeneous deep mantle, the enriched mantle 1 (EM-1) source of Pitcairn Island, has been attributed to the contribution of crustal material with vastly different chemical compositions and ages. The Mo isotope composition of lavas from Pitcairn Island constrains the nature of this recycled crustal component. Pitcairn lavas have elevated $\delta^{98/95}$Mo relative to the depleted mantle. The high $\delta^{98/95}$Mo is associated with high time-integrated $^{232}$Th/$^{238}$U and $^{87}$Rb/$^{86}$Sr with low time-integrated $^{147}$Sm/$^{144}$Nd and $^{238}$U/$^{206}$Pb, which can be attributed to the recycling of nearly pristine pelagic sediments that were deposited in a Proterozoic redox-stratified deep-ocean. The isotope data at Pitcairn is similar to that of EM-1 hotspots from the South Atlantic, indicating the addition of reduced sediments in both of Earth's large low shear wave velocity provinces (LLSVPs). The data seem to argue in favor of the preservation of pre-subduction isotope and element signatures. This indicates that the subduction cycling of redox-sensitive elements such as Mo, S, Se, and U into arc magmas was inefficient in the Precambrian. This conclusion is in line with the appearance of widespread oxidation of global arc magmas only after the Neoproterozoic Oxidation Event. Likely the transition to a fully aerobic ocean within the Phanerozoic impacted the redox budget in subduction zones and affected the mobility and recycling of redox-sensitive elements in convergent margin settings, where new continental crust is dominantly formed. This likely had an influence on the composition of the Precambrian continental crust and therefore, the trace element budget of the ocean and the evolution of life in the oceans.

## Introduction

Plate tectonics and Earth's surface oxygenation are intimately linked and influence the Earth's principal geochemical reservoirs by redistributing elements during Earth's evolution (e.g., Kump and Barley, 2007; Campbell and Allen, 2008; Keller and Schoene, 2012; Lee et al., 2016; Smit and Mezger, 2017). This determines the chemical composition of Earth's mantle, crust, atmosphere, and hydrosphere, and consequently has an impact on the distribution of elements essential for life (Zerkle, 2018). The subduction of Earth's surface material, which has been geochemically modified by low-temperature processes, leads to distinct chemical heterogeneities in Earth's interior and can provide complementary information about secular changes in the surface redox conditions (e.g., Cabral et al., 2013; Andersen et al., 2015; Gaschnig et al., 2017, 2021b; Stolper and Bucholz, 2019; Liu et al., 2019; Dottin et al., 2020; Yierpan et al., 2020; Ahmad et al., 2022). Redox-sensitive stable metal isotopes can be used to further constrain the origin, nature, and scale of compositional heterogeneity in the Earth's deep mantle, which has conventionally been constrained by major- and trace-element, and radiogenic isotope systematics in plume-influenced mid-ocean ridge basalts (MORB) or ocean island basalts (OIB). The isotope variations of the redox-sensitive element Mo are a suitable tool to study the compositional heterogeneity in the Earth's deep mantle and how this heterogeneity relates to processes on and materials from the Earth's surface; in particular the redox condition of this material. The elemental and isotope signatures of Mo are distinct between the mantle and surface reservoirs due to the incompatible behavior of Mo during magmatic processes (e.g., Newsom et al., 1986) and its redox-dependent aqueous mobility (e.g., Bali et al., 2012; Freymuth et al., 2015; König et al., 2016; Kendall et al., 2017; Ahmad et al., 2021). Therefore, Mo isotopes can track the subduction of surface-derived material into the mantle (e.g., Gaschnig et al., 2021b; Ma et al., 2022; Ahmad et al., 2022; Hin et al., 2022).

The Mo isotope systematics are particularly interesting because the extent of Mo isotope fractionation during subduction depends on the oxidation state of the slabs. In principle, Mo isotope ratios are modified by mass-dependent isotope fractionation during prograde subduction metamorphism (e.g., Freymuth et al., 2015; König et al., 2016; Chen et al., 2019; Ahmad et al., 2021). The extent of this isotope fractionation on bulk rocks is directly dependent on the Mo mobility during subduction (e.g., Chen et al., 2019; Ahmad et al., 2021, 2022), which in turn depends on the oxygen fugacity ($fO_2$) in the associated subduction zone fluids (Bali et al., 2012; Skora et al., 2017; Chowdhury et al., 2022). In other words, the stable Mo isotope ratio of a subducted slab integrates the redox-dependent aqueous mobility of Mo during subduction processes. Because the redox state of subducting sediments is a reflection of Earth's surface $O_2$ availability (e.g., Evans, 2012), Mo isotopes of subducted slabs indirectly reflect Earth's surface oxygen levels. Plumes that sample a deep mantle domain can be modified by this surface signature (Gaschnig et al., 2021b; Ahmad et al., 2022). Here, the constraints brought by Mo isotopes on the notorious Pitcairn mantle source are investigated.

This study presents Mo isotope compositions of basalts collected from active submarine volcanoes about 80 km east of the island of Pitcairn in the South-Pacific Ocean during the Polynaut cruise (1999) (Hekinian et al., 2003). Pitcairn Island represents one of the end member type-localities of the compositionally heterogeneous deep mantle, the enriched mantle 1 (EM-1) domain, and is associated with the Pacific large low shear wave velocity province (LLSVPs) (e.g., French and Romanowicz, 2015; Jackson et al., 2021). Pitcairn Island basalts have moderately primordial Ne (Honda and Woodhead, 2005) associated with highly radiogenic $^{87}Sr/^{86}Sr$ and $^{208}Pb/^{204}Pb$, while having some of the least radiogenic $^{206}Pb/^{204}Pb$ among known OIBs (Woodhead and Devey, 1993). This enriched component requires a low time-integrated μ ($^{238}U/^{204}Pb$) associated with high time-integrated κ ($^{232}Th/^{238}U$) and $^{87}Rb/^{86}Sr$. Different recycled geochemical reservoirs have been proposed to explain the enriched mantle source of Pitcairn Island, including metasomatized lithospheric mantle, pelagic sediments, marine carbonates, and lower continental crust (e.g., Woodhead and McCulloch, 1989; Eisele et al., 2002; Stracke, 2012; Garapić et al., 2015; Delavault et al., 2016; Wang et al., 2018; Labidi et al., 2022). The recycling age of potentially recycled subducted sediments was interpreted to be Precambrian based on radiogenic isotopes and stable S isotopes (Eisele et al., 2002; Garapić et al., 2015; Delavault et al., 2016; Labidi et al., 2022). The occurrence of sediments in the source of the Pitcairn basalts can be tested using Mo isotopes. Due to the redox-sensitive behavior of Mo, a potential recycled anoxic (Precambrian) deep-sea sediment will exhibit a Mo isotope composition that is heavier than the depleted mantle (Ahmad et al., 2022). Previously measured samples from Pitcairn Island are subaerial lavas, erupted on land. They exhibit $\delta^{98/95}Mo$ lighter than the depleted mantle (Gaschnig et al., 2021b). The light isotopic signature, however, was explained by the influence of tropical weathering due to the correlation with Mo/Ce ratios and a secular disequilibrium recorded by $^{238}U/^{234}U$ ratios (Gaschnig et al., 2021b). Therefore, it was not possible to constrain the primary Mo isotope signature of the Pitcairn mantle plume. The active seamounts studied here offer fresh basaltic glassy material that is likely not affected by secondary processes such as weathering and thus can be expected to preserve the geochemical characteristics of the hotspot. We analyzed glassy rims of pillow basalts that were sampled with the Nautile submersible from the flanks of the seamounts "Bounty" and "Volcano 5". All samples are well-characterized in terms of radiogenic isotopes (Sr, Nd, and Pb), S isotopes, volatile abundances, and major element abundances (Labidi et al., 2022). Furthermore, selected trace element data is available (Clog, 2010) making it ideal to study the EM-1 end member component of the Pitcairn mantle source with Mo isotopes.

## Results

Details on Mo purification and isotope analysis, and individual sample measurements can be found in the Supplementary Information. The samples reported in Table 1 have $^{87}Sr/^{86}Sr$, $^{143}Nd/^{144}Nd$, $^{206}Pb/^{204}Pb$, and $^{208}Pb/^{204}Pb$ of EM-1 type (Labidi et al., 2022). The radiogenic isotope signatures of the basalts are similar to the most enriched EM-1 influenced MORBs from the South-Mid Atlantic Ridge (Fig. 3). The $\delta^{98/95}Mo$ values of Pitcairn basaltic glass samples exhibit a small range between −0.12 ‰ and −0.09 ‰ (n=10), with an average of −0.11 ‰. The variation between Pitcairn basalts is smaller than the external 2SD reproducibility of ± 0.05 ‰ (Table 1). Within uncertainty, all samples are isotopically heavier than the depleted mantle ($\delta^{98/95}Mo = -0.204 \pm 0.008$ ‰; McCoy-West et al., 2019), unlike previously published Mo isotope data of Pitcairn Island lavas that are influenced by weathering (Gaschnig et al., 2021b). Overall, Mo concentrations range between 1.26 and 4.40 µg/g, higher than average MORB (~0.45 µg/g; Gale et al., 2013). Only considering the least differentiated samples, with MgO content ranging from 4.6 to 5.6 wt%, a large [Mo] variability between 1.26 and 2.93 µg/g can be observed. Furthermore, Mo/Ce ratios are variable (0.022 to 0.038) overlapping with average MORB Mo/Ce (~0.031; Gale et al., 2013) (Fig. 2).

***Table 1.*** *Mo concentration and isotope data on Pitcairn Island lavas. Literature data from Labidi et al. (2022), except (A) is from Bourdon and Van Orman (2009) and La/Sm ratios, and Ce values are from Clog (2010). Element oxides are in wt%, while minor and trace elements are in µg/g.*

| sample ID | pn03-01 | pn03-02 | pn03-03 | pn03-05 | pn03-07 | pn03-08 | pn03-10 | pn03-11 | pn08-07 | pn14-04 |
|---|---|---|---|---|---|---|---|---|---|---|
| seamount | bounty | bounty | bounty | bounty | bounty | bounty | bounty | bounty | volc. 5 | bounty |
| depth (mbsl) | 2508 | 2508 | 2500 | 2408 | 2276 | 2250 | 2165 | 1957 | | 1705 |
| | | | | | | | | | | |
| $Na_2O$ | 4.2 | 4.2 | 4.2 | 3.8 | 3.9 | 4.2 | 3.5 | 4.0 | 4.2 | 4.2 |
| $SiO_2$ | 47.8 | 47.9 | 47.7 | 47.8 | 47.6 | 48.8 | 50.6 | 48.9 | 54.4 | 54.2 |
| $K_2O$ | 1.4 | 1.4 | 1.5 | 1.4 | 1.4 | 1.6 | 0.8 | 1.6 | 2.7 | 2.3 |
| $Al_2O_3$ | 16.0 | 16.0 | 15.8 | 15.4 | 15.3 | 16.2 | 15.1 | 15.3 | 16.1 | 15.3 |
| CaO | 9.1 | 9.1 | 9.1 | 9.8 | 9.7 | 8.1 | 8.6 | 8.7 | 4.9 | 5.4 |
| MgO | 5.4 | 5.5 | 4.8 | 5.2 | 5.4 | 5.0 | 5.6 | 4.6 | 2.6 | 2.6 |
| $P_2O_5$ | 0.7 | 0.7 | 0.8 | 0.7 | 0.7 | 0.8 | 0.5 | 0.8 | 1.2 | 1.2 |
| FeO | 9.7 | 9.8 | 9.7 | 9.9 | 10.0 | 9.7 | 9.6 | 9.7 | 9.1 | 9.5 |
| MnO | 0.2 | 0.2 | 0.2 | 0.2 | 0.2 | 0.2 | 0.1 | 0.2 | 0.2 | 0.2 |
| $TiO_2$ | 2.9 | 2.9 | 3.0 | 3.1 | 3.1 | 3.3 | 3.1 | 3.4 | 1.9 | 2.2 |
| total | 97.5 | 97.6 | 96.8 | 97.2 | 97.1 | 97.9 | 97.6 | 97.2 | 97.2 | 97.0 |
| | | | | | | | | | | |
| Mo | 2.47 | 1.26 | 2.45 | 2.23 | 1.53 | 2.93 | 1.38 | 2.41 | 4.40 | 4.22 |
| Cl | 502 | 494 | 498 | 426 | 424 | 459 | 324 | 417 | 493 | 750 |
| Cu | 59 | 50 | 52 | 50 | 56 | 33 | 37 | 50 | 3 | 11 |
| $H_2O$ | 9192 | 9807 | 9662 | 8512 | 8125 | 9099 | 5696 | 5667 | | 12123 |
| $S^{2-}$ | 1279 | 1299 | 1133 | 953 | 875 | 738 | 1017 | 569 | 602 | 507 |
| Ce | | | | 70.4 | 69.7 | 77.0 | 48.9 | 69.9 | | |
| | | | | | | | | | | |
| $K_2O/TiO_2$ | 0.49 | 0.48 | 0.49 | 0.44 | 0.45 | 0.49 | 0.27 | 0.47 | 1.40 | 1.06 |
| $CaO/Al_2O_3$ | 0.57 | 0.57 | 0.58 | 0.63 | 0.63 | 0.50 | 0.57 | 0.57 | 0.30 | 0.36 |
| Cl/K | 0.04 | 0.04 | 0.04 | 0.04 | 0.04 | 0.03 | 0.05 | 0.03 | 0.02 | 0.04 |
| $S^{2-}/S_{tot}$ | 97 | 98 | 80 | 95 | 91 | 100 | 95 | 72 | 100 | 99 |
| Mo/Ce | | | | 0.032 | 0.022 | 0.038 | 0.028 | 0.034 | | |
| $(La/Sm)_N$ | | | | 2.66 | 2.64 | 3.17 | 2.07 | 3.17 | | |
| | | | | | | | | | | |
| $\delta^{98/95}Mo$ (‰) | −0.121 | −0.121 | −0.112 | −0.113 | −0.111 | −0.119 | −0.115 | −0.111 | −0.097 | −0.093 |
| $\delta^{34}S$ (‰) | 0.1 | 0.2 | −1.0 | −1.2 | −1.3 | −1.0 | −1.2 | −1.2 | 1.6 | 0.7 |
| $\Delta^{33}S$ (‰) | 0.020 | 0.028 | 0.025 | 0.028 | 0.012 | 0.027 | 0.030 | 0.031 | 0.026 | 0.007 |
| $\Delta^{36}S$ (‰) | 0.08 | 0.08 | 0.05 | 0.13 | 0.08 | 0.06 | 0.06 | 0.06 | 0.02 | −0.06 |
| | | | | | | | | | | |
| $^{206}Pb/^{204}Pb$ | 17.742 | 17.742 | 17.749 | 17.816 | 17.809 | 17.747 | 17.926 | 17.770 | | 18.1982335 |
| $^{207}Pb/^{204}Pb$ | 15.470 | 15.470 | 15.474 | 15.482 | 15.479 | 15.475 | 15.493 | 15.479 | | 15.5167915 |
| $^{208}Pb/^{204}Pb$ | 38.569 | 38.570 | 38.579 | 38.645 | 38.658 | 38.644 | 38.798 | 38.668 | | 38.9161373 |
| $^{143}Nd/^{144}Nd$ | | | 0.512567 | 0.512599 | 0.512583 | 0.512537 | | 0.512944 | | 0.512762 |
| $^{87}Sr/^{86}Sr$ | 0.704483 | 0.704477 | 0.704485 | 0.704482 | 0.704498 | 0.704624 | 0.704481 | 0.704531 | | 0.704002 |
| $^{87}Sr/^{86}Sr^A$ | | | | 0.70446 | | 0.70463 | 0.70447 | | 0.70530 | |

# Discussion

The Pitcairn lavas define the end member of the EM-1 component. Their composition is a result of a complex history of mixing processes prior to eruption including mantle source enrichment, low degrees of partial mantle melting, followed by magmatic differentiation and sulfide segregation, and various extents of volatile loss via degassing (see Labidi et al., 2022). All these processes can potentially affect the Mo isotopic composition of the erupted melts.

## The potential effect of secondary and magmatic processes on $\delta^{98/95}$Mo

The primary isotope composition of Mo preserved in rocks and minerals can be modified by direct or indirect interaction with seawater. Although careful picking of fresh glass avoids the former, it is not possible to visibly detect magmatic assimilation of altered oceanic crust (AOC) that happened en route to the surface or to eliminate all traces of Fe-Mn coating in picked samples. The Cl/K ratios are < 0.05 for Bounty lavas and <0.02 for Volcano 5 samples (Labidi et al., 2022) (Table 1), which is below the threshold of 0.10, above which lavas are considered to be contaminated significantly by Cl-rich brines (Michael and Cornell, 1998). These low Cl/K ratios exclude Cl enrichment caused by hydrated oceanic crust, brine assimilation, and potential seawater alteration. Also excluded can be effects caused by Mo adsorption on Fe-Mn oxides, because this would have shifted the Mo isotope composition towards $\delta^{98/95}$Mo<depleted mantle (-0.20 ‰; McCoy-West et al., 2019). It is also unlikely that seafloor alteration, crustal assimilation, or Mn-oxide contribution would generate a statistically homogeneous $\delta^{98/95}$Mo in all investigated samples derived from different sampling depths (Table 1).

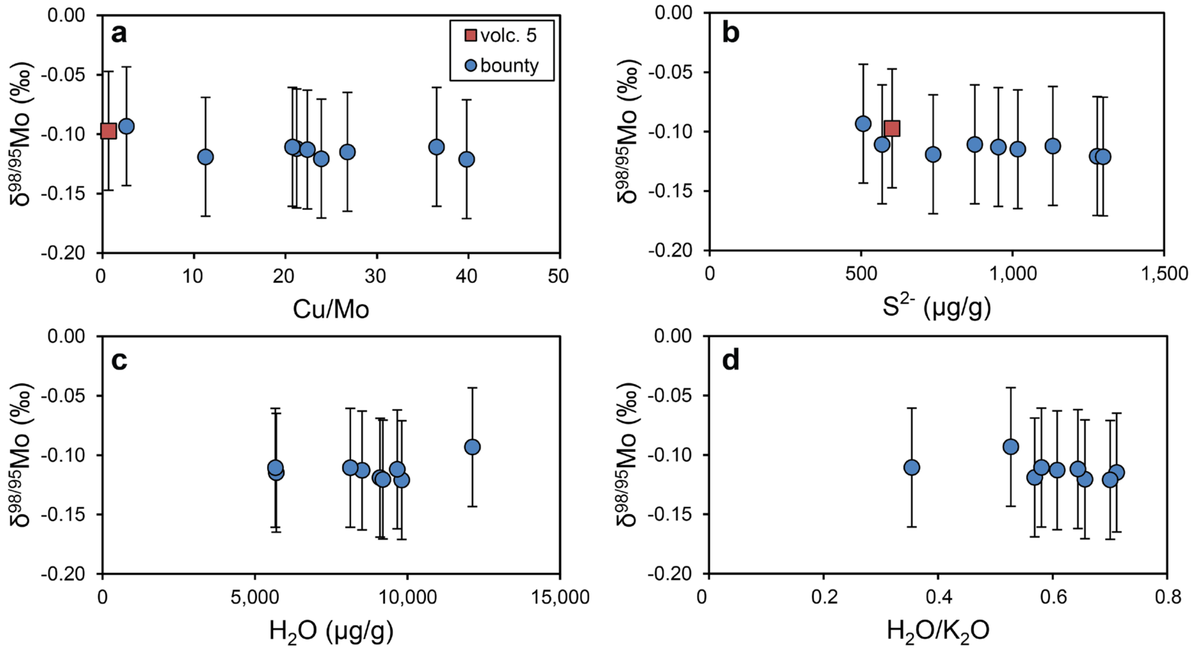

***Figure 1.*** *Plots of $\delta^{98/95}$Mo vs. (a) Cu/Mo; (b) $S^{2-}$; (c) $H_2O$; (d) $H_2O/K_2O$. Error bars indicate 2 SD external reproducibility.*

The variability of the bulk S content in the Pitcairn lava is attributed to continuous tholeiite-like sulfide segregation and magmatic degassing (Labidi et al., 2022), which may have also affected the Mo isotope composition of the residual silicate melt (e.g., Greber et al., 2014; Liang et al., 2017; Kaufmann et al., 2021; Hin et al., 2022). However, increasing sulfide melt segregation indicated by decreasing Cu/Mo ratios in the silicate melt due to the more chalcophile affinity of Cu does not show any covariation with $\delta^{98/95}$Mo (Fig. 1). Furthermore, no control of magmatic degassing onto the Mo isotope composition is observed, because the variable $H_2O$ (and $H_2O/K_2O$) and S contents of the samples, which correlate with water depth (Labidi et al., 2022), are decoupled from Mo isotopes (Fig. 1).

No measurable isotopic difference among the least and most primitive samples (i.e. pn03-10 and pn14-04; Fig. 2) is observed indicating that the effect of fractional crystallization (e.g., Voegelin et al., 2014; Wille et al., 2018) is negligible on the Mo isotope composition of the Pitcairn samples, which is similar to observations made in other magmatic systems (Yang et al., 2015; Bezard et al., 2016; Nebel-Jacobsen et al., 2021; Gaschnig et al., 2021a).

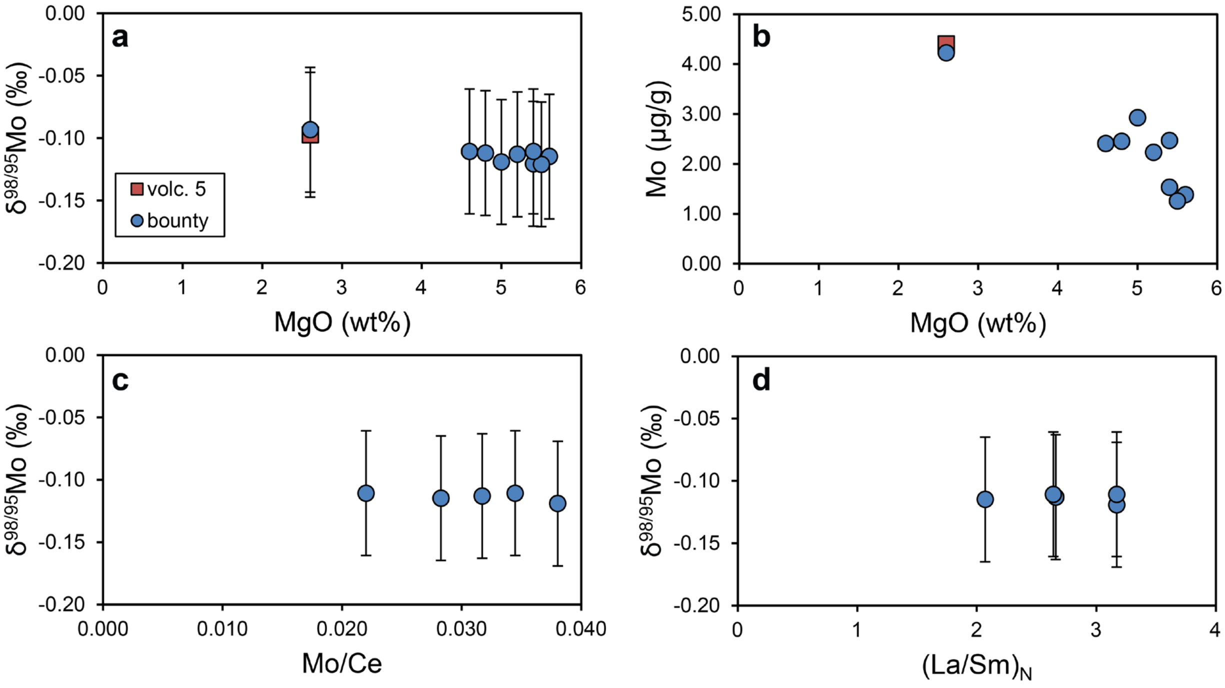

***Figure 2.*** *Plots of (a) $\delta^{98/95}$Mo vs. MgO; (b) Mo vs. MgO; (c) $\delta^{98/95}$Mo vs. Mo/Ce; (d) $\delta^{98/95}$Mo vs. $(La/Sm)_N$. Error bars indicate 2 SD external reproducibility.*

Sample Mo/Ce and La/Sm ratios vary significantly (Fig 2), potentially indicating a variable input of isotopically heavy low-degree melts due to the higher incompatibility of isotopically heavy $Mo^{6+}$ over light $Mo^{4+}$ during mantle melting (McCoy-West et al., 2019; Chen et al., 2022). However, the homogeneous $\delta^{98/95}$Mo values of the basaltic lavas indicate that low-degree mantle melting had an insignificant effect on the Mo isotope composition of investigated lavas. This potentially indicates a minor influence of low-degree melts onto the Mo isotope composition in plume-influenced OIBs compared to MORB settings (e.g., East Pacific Rise; Chen et al., 2022). This might be explained by melting at higher temperatures along the hotter plume-adiabat (e.g., Putirka, 2008), resulting in smaller effects on Mo isotope fractionation during mantle melting (Ahmad et al., 2022).

## The potential role of recycled components

As the heavy Mo isotope composition of Pitcairn Island basalts cannot be attributed to assimilation or mineral fractionation, this indicates that the enrichment of the EM-1 component in $^{98}$Mo is a mantle source feature. Various crustal materials have been proposed as the recycled material in the plume source, including metasomatized lithospheric mantle, oceanic sediments, and components from the lower continental crust.

Worldwide peridotites have a depleted mantle-like $\delta^{98/95}$Mo (−0.206 ± 0.05‰) (Liang et al., 2017) which is also likely the composition of the subcontinental mantle and cannot explain the homogeneous $\delta^{98/95}$Mo heavier than depleted mantle in the Pitcairn lavas. Processes involving fluid-driven enrichments of isotopically heavy Mo into the subcontinental mantle in convergent plate settings (e.g., Freymuth et al., 2015; König et al., 2016; Chen et al., 2019; Ahmad et al., 2021) could in principle account for the data. A similar model was taken to account for the O isotope data of Pitcairn Island phenocrysts (Eiler et al., 1995). However, systematic enrichments or depletions of fluid mobile elements are not observed in the Pitcairn Island source (Willbold and Stracke, 2006). Overall, the trace element data argue against the presence of a subduction-influenced lithospheric mantle in the source of Pitcairn.

A major component of lower continental crust (LCC) material has been suggested earlier for the Pitcairn Island mantle source (e.g., Stracke, 2012 and references therein). There is no direct estimate of $\delta^{98/95}$Mo of the LCC, however, cumulates that possibly reside in the LCC, likely have light Mo isotope signatures (Wille et al., 2018; Nebel-Jacobsen et al., 2021) and are unsuitable candidates to explain the observed Mo isotope compositions in the basalt samples. Furthermore, the low time-integrated $^{238}$U/$^{204}$Pb, which is characteristic of the Pitcairn EM-1 mantle source, and overall unradiogenic $^{206}$Pb/$^{204}$Pb indicate that recycled isotopically variable AOC (Freymuth et al., 2015; Ahmad et al., 2021) is not suitable to produce the EM-1 characteristics. Phanerozoic subducted sediments and mafic oceanic crust are isotopically light (Chen et al., 2019; Ahmad et al., 2021) and can also not explain the isotopically heavy nature of the EM-1 component. Previous studies have attributed the radiogenic isotope and stable Mg isotope composition of the Pitcairn Island mantle source to the recycling of subducted marine carbonates (Delavault et al., 2016; Wang et al., 2018).

However, mixing with such a component is not reflected in the Mo isotope composition of the basalts, as carbonates have low Mo concentrations (< 100 ng/g) (e.g., Voegelin et al., 2009) (see Fig. 4).

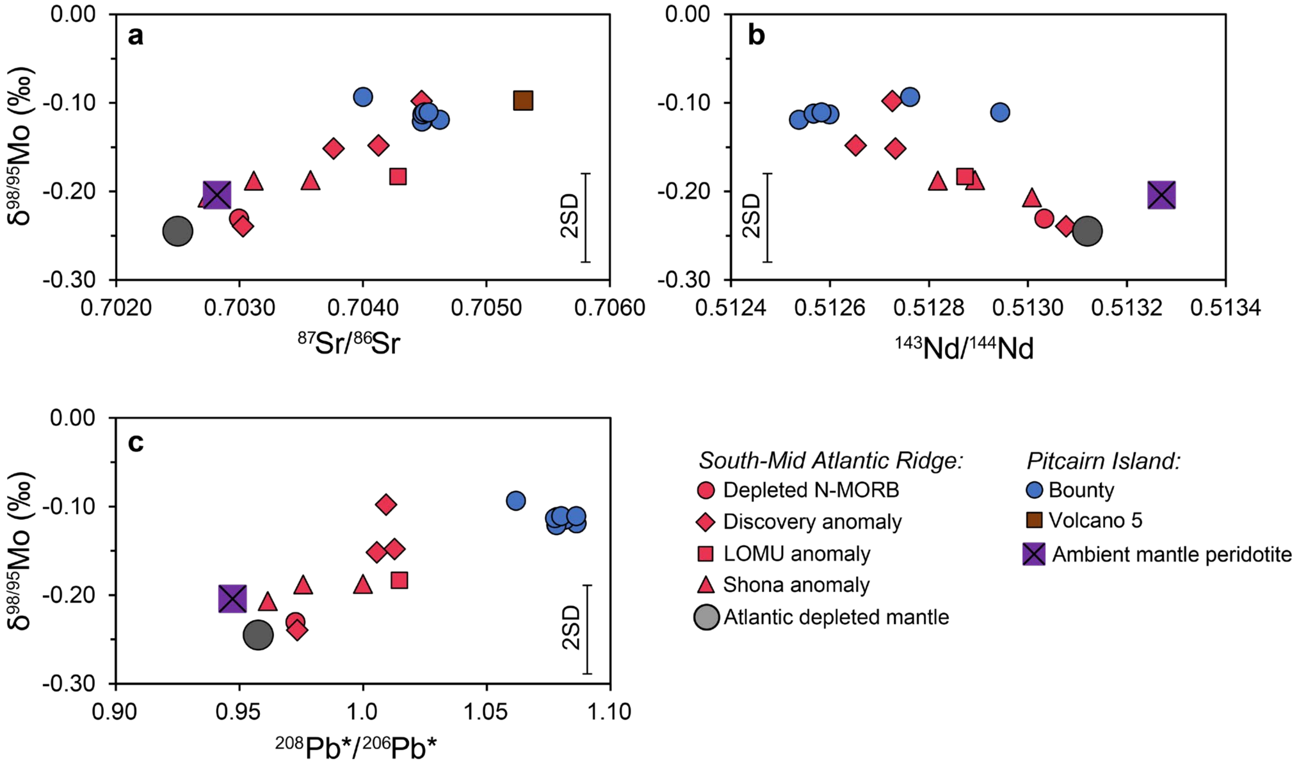

***Figure 3.*** *Covariation diagram of EM-1 influenced lavas from S-MAR and Pitcairn Island (this study). (a) $\delta^{98/95}$Mo vs. $^{87}$Sr/$^{86}$Sr; (b) $\delta^{98/95}$Mo vs. $^{143}$Nd/$^{144}$Nd; $\delta^{98/95}$Mo vs. $^{208}$Pb*/$^{206}$Pb* (time-integrated Th/U). Error bars indicate 2 SD external reproducibility.*

A Proterozoic pelagic sediment contribution can best explain the observed Mo isotope systematics. First, the Mo isotope signature of the modeled sedimentary end member (Fig. 4) is UCC-like, which is expected for subducted pelagic sediments deposited in the Proterozoic anoxic bottom ocean (Ahmad et al., 2022). Also, less than 2 % of this material is needed to explain the heavy Mo signature of the Pitcairn Island mantle source (2 component mixing between UCC and DM; Table S-2). A sedimentary origin for the EM-1 source of Pitcairn Island was argued against on the basis of basalt phenocryst O isotope signatures (Eiler et al., 1995, 1997). However, sediment contributions in the mantle below 2% remain undetected with stable O isotopes (Eiler et al., 1995). In addition, modeling of a sedimentary end member based on S-isotope data on the Pitcairn samples (Table 1) (Labidi et al., 2022), suggested that a contribution of ≤ 2% anoxic Proterozoic deep-sea sediments can fulfill the trace element and isotope systematics of the EM-1 source of Pitcairn Island. Due to the increased compatibility of $Mo^{4+}$ in stable Mo-bearing hosts in the anoxic subducted sedimentary units, such as rutile or sulfides (see Bali et al., 2012; Skora et al., 2017; Chowdhury et al., 2022) it is expected that Mo is immobile in reduced sediments during prograde subduction metamorphism (Ahmad et al., 2022). Therefore, no significant isotope fractionation during the subduction of reduced sediment is expected. Thus, the original sedimentary Mo isotope signatures and element abundances are preserved in the deep mantle. Such behavior is not expected for Mo in Phanerozoic oxidized sediments (Ahmad et al., 2022).

## Anoxic pelagic sediments as a source for EM-1

Different ages for the recycled sediments in the mantle source of Pitcairn Island lavas have been proposed. Labidi et al. (2022) argue that based on the small range of $\Delta^{33}$S and $\Delta^{36}$S most likely Proterozoic (reduced) sediments were recycled into the mantle source of Pitcairn Island. This is supported by other studies indicating a sediment contribution of (Mid-)Proterozoic age as a likely end member of the Pitcairn plume e.g., (Woodhead and McCulloch, 1989; Eisele et al., 2002; Delavault et al., 2015). A (Mid-)Proterozoic pelagic sediment end member has also been identified for EM-1 influenced lavas from the South-Mid Atlantic Ridge (S-MAR), which interact with the Discovery- and Shona mantle plumes, based on correlations between radiogenic isotopes of Sr, Nd, and Hf, and $fO_2$-sensitive stable isotope systems of S, Se, and Mo (Douglass et al., 1999; Andres et al., 2002; le Roux et al., 2002; Labidi et al., 2013; Yierpan et al., 2020; Ahmad et al., 2022) (Fig 3). The Mo and radiogenic isotope systematics of the Pitcairn lavas are similar to S-MAR (Fig. 3). A cross-plot of $\delta^{98/95}$Mo vs. $^{87}$Sr/$^{86}$Sr, $^{143}$Nd/$^{144}$Nd, and $^{208}$Pb*/$^{206}$Pb* (time-integrated Th/U) shows that the Pitcairn lavas influenced by the EM-1 component extend the covariation seen in S-MAR samples, pointing towards a similar Proterozoic pelagic sedimentary end member with a Mo isotopic composition heavier than the depleted mantle (Fig. 3). It is likely that the Proterozoic deep-ocean processes under anoxic conditions imparted a major control on the Th/U ratios of the sedimentary end member causing the EM-1 Pb-isotope signatures in Pitcairn Island and S-MAR (Fig 3c). Under reducing conditions, U is immobile like Th. However, Th behaves particle-reactive independent of ocean redox conditions, leading to higher Th enrichments over U in deep-sea pelagic clay similar to present-day pelagic clays (Plank and Langmuir, 1998). The chemical composition of modern pelagic sediments likely differs from those deposited in Precambrian anoxic deep waters, because potential U hosts such as biogenic phosphate (bone and teeth debris) and Fe-Mn oxides were absent. The absence of these U hosts together with a much lower dissolved U ocean reservoir (Lyons et al., 2014) lowered the U flux into deep-sea sediments. Furthermore, the anoxic Proterozoic deep-ocean setting did not allow significant U enrichments in pelagic sediments due to the larger euxinic sink with larger organic matter (OM) flux close to the continents (i.e. continental shelves) leading to preferential U deposition in these areas (e.g., Lyons et al., 2014; Laakso and Schrag, 2019). This suggests that high Th/U in ancient deep-sea sediments is a consequence of global Proterozoic (anoxic) deep-sea conditions. In the case of Pitcairn Island, previous studies argued that rising atmospheric oxygen levels at the Archean-Proterozoic boundary and oxidative weathering led to the formation of sediments with high time-integrated Th/U (e.g., Eisele et al., 2002; Garapić et al., 2015). The sediments were subsequently recycled into the EM-1 source. It has been argued that the rise in atmospheric oxygen levels oxidized crustal $U^{4+}$ to the aqueous mobile $U^{6+}$ that was therefore fractionated during continental weathering from the similar magmatic incompatible and aqueous immobile Th. This led to high Th/U in the residue of oxidatively weathered continental material and subsequently to high Th/U in pelagic sediments. However, crustal weathering under oxidizing conditions would also release preferentially heavy aqueously soluble $Mo^{6+}$, which would lower the Mo/Pr (and Mo/Ce) and $\delta^{98/95}$Mo of this residual material below the average UCC (Greaney et al., 2020), which cannot not explain the observed data (Fig. 4). Therefore, it can be argued that the EM-1 source signature reflects the contamination by pelagic sedimentary Th/U and $\delta^{98/95}$Mo from a continental source with enrichments of particle-reactive Th and Pb from a Mo and U depleted Proterozoic redox-stratified ocean.

The fact that two EM-1 influenced suites (i.e. Pitcairn and Shona/Discovery plumes) from both LLSVPs, i.e. the Pacific and the African, show a common trend in radiogenic isotopes that correlates with $\delta^{98/95}$Mo (Fig. 3) might indicate widespread recycling of (Mid-)Proterozoic anoxic pelagic sediments into the deep mantle. This is consistent with geochemical similarities between EM-type plume-influenced volcanic rocks from both LLSVPs indicating broadly similar formation processes and similar histories (Jackson et al., 2018). The anoxic Proterozoic deep-sea bottom waters (e.g., Lyons et al., 2014) together with the low abundances of passive margins during the formation and stabilization of the Columbia supercontinent during the Mid-Proterozoic (e.g., Bradley, 2011) indicates widespread accumulation of pelagic sediments in the superocean with potentially high $\delta^{98/95}$Mo and Th/U. Subduction recycling of this material at the subduction girdle surrounding the supercontinent (see Li et al., 2019) can therefore account for the widespread contamination of the LLSVPs with anoxic sediments. This recycling of surface material to the lower mantle generated EM-1 sources with high $^{208}Pb^{*}/^{206}Pb^{*}$, $\delta^{98/95}$Mo, $\delta^{82/76}$Se and $\delta^{34/32}$S (e.g., Labidi et al., 2013, 2022; Yierpan et al., 2020; Ahmad et al., 2022). Furthermore, deep-mantle contamination with anoxic material is supported by C isotope data of degassed $CO_2$ at Pitcairn Island and OIBs elsewhere, which suggests recycled reduced C in their source (Eguchi et al., 2020).

These findings support the model that the redox structure of Earth's surface is directly connected to the deep-mantle compositional (Mo isotope) differences (Gaschnig et al., 2021b) and inform about redox conditions of subducted material (Ahmad et al., 2022). Phanerozoic subducted Mn-Fe rich sediments can efficiently buffer subduction zone fluids towards oxidizing conditions (see Ague et al., 2022), while Precambrian subducted anoxic sediments buffer redox-conditions during prograde subduction metamorphism to anoxic conditions (see Ahmad et al., 2022). The widespread subduction of anoxic material and the preservation of isotopic signatures of Mo, Se, and S characteristic of sediments in EM-1 sources (Labidi et al., 2013; Yierpan et al., 2020; Ahmad et al., 2022) suggests a stable sulfide phase during Precambrian subduction and negligible mobilization of these elements during prograde subduction metamorphism. As a consequence, decreasing subduction recycling efficiency into the mantle wedge and ultimately arc magmatism is expected for these (and probably other) redox-sensitive elements compared to the Phanerozoic. This is in line with inefficient subduction recycling of U during the Precambrian except during the major oxidation events (Liu et al., 2019) and limited redox transfer as indicated by $Fe^{3+}/Fe^{2+}$ and V/Sc ratios in arc lavas, which systematically rose only after the Neoproterozoic Oxidation Event (NOE) due to the oxygenation of the deep ocean with increased levels of sulfates that were available for subduction (Stolper and Bucholz, 2019). This further supports the notion that subducted anoxic sediments acted as a redox filter, which could buffer fluids from the underlying AOC and serpentinites to reducing conditions independent of their original $fO_2$ (by analogy to the model of (Ague et al., 2022)). This low $fO_2$ consequently leads to suppressed redox budget transfer into arc magmas as well as mobility of e.g., Mo, Se, S, and U, therefore, decreasing abundances of these elements in the continent forming magmatic rocks. This, in turn, has implications on e.g., the formation of subduction-related ore deposits through Earth's evolution (e.g., Richards and Mumin, 2013). Furthermore, the changing composition of the continental crust (i.e. with respect to bio-essential elements) during Earth's evolution might have an influence on the trace element budget of the ocean (Dürr et al., 2005), which places a first-order control on the evolution of complex life (Zerkle, 2018).

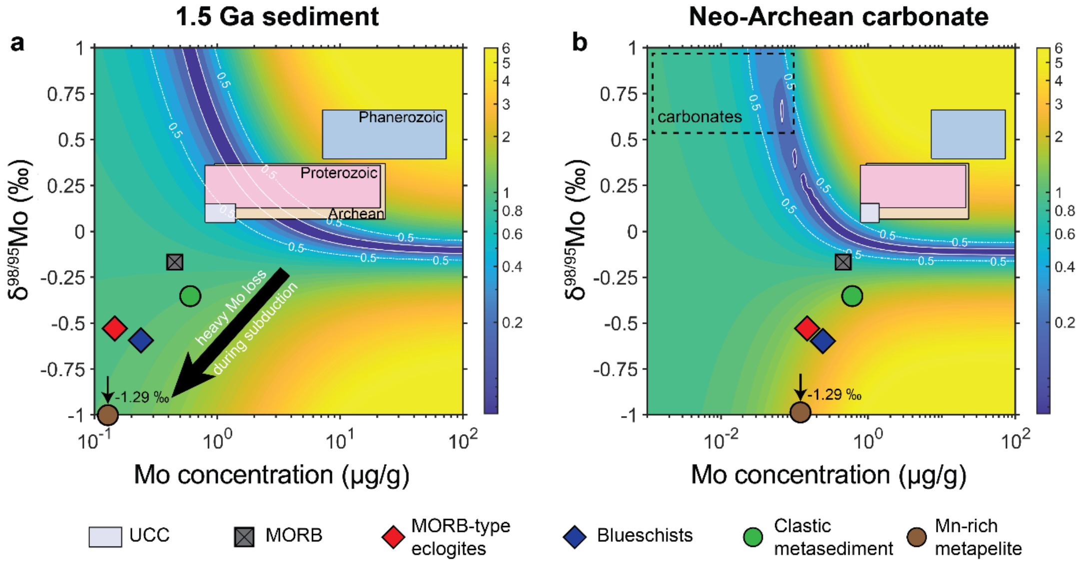

***Figure 4.*** *Least squares error ($\Delta^{98/95}$Mo in ‰; up to 6 ‰) between calculated mixing lines and analyzed samples (after Ahmad et al., 2022). Variables are the $\delta^{98/95}$Mo and [Mo] values derived from the $\delta^{98/95}$Mo vs. $^{87}Sr/^{86}Sr$ relationship (Fig. 3). Literature values for potential (concentration averaged) recycled lithologies, and anoxic sediments sorted by age intervals are shown for comparison. See Supplementary Information for references, mixing parameters, and further details.*

## Conclusion

The lavas from Pitcairn Island define the known end member of the EM-1 mantle component. This makes it particularly suitable to constrain the chemical and isotopic composition of this distinct and important mantle component and elucidate its genesis. Applying mixing models using combined Mo and radiogenic isotopes from fresh Pitcairn Island basalts suggests that Proterozoic pelagic sediments are a plausible contaminant to explain the Mo isotopic signature of the Pitcairn mantle source. This conclusion is in line with EM-1 influenced lavas from the South Atlantic, where a recycled anoxic sediment contribution was proposed previously. Correlations of radiogenic isotopes and stable Mo isotopes from both settings suggest a common origin of the widespread contamination of Earth's LLSVPs, likely caused by the subduction of Proterozoic anoxic pelagic sediments. This confirms that the Mo isotope signature of enriched mantle-influenced lavas can constrain the redox conditions of potentially recycled sediments as well as during the subduction of those (see Ahmad et al., 2022). The preservation of pre-subducted sedimentary Mo and S isotope signatures in the EM-1 mantle source suggests decreased subduction recycling of certain redox-sensitive elements into the mantle wedge in the Precambrian. This can explain the widespread oxidation of global arc magmas just to occur at the NOE. Furthermore, this has a first-order control on the chemical composition of the continental crust in the Precambrian and can therefore have an impact on ocean chemistry and the evolution of life itself.

## Acknowledgements

This study was funded by the Swiss National Science Foundation, Switzerland (Grant number 182508) to MW. The MC-ICP-MS at the Institute of Geological Sciences, University of Bern used in this study was acquired within the framework of the NCCR project PlanetS (Grant nr. 1NF40-141881) funded by the Swiss National Science Foundation. SK acknowledges Ramón y Cajal contract RYC2020-030014-I.

# References

Ague, J.J., Tassara, S., Holycross, M.E., Li, J.-L., Cottrell, E., Schwarzenbach, E.M., Fassoulas, C., and John, T., 2022, Slab-derived devolatilization fluids oxidized by subducted metasedimentary rocks: Nature Geoscience 2022, p. 1–7, https://doi.org/10.1038/s41561-022-00904-7.

Ahmad, Q., Wille, M., König, S., Rosca, C., Hensel, A., Pettke, T., and Hermann, J., 2021, The Molybdenum isotope subduction recycling conundrum: A case study from the Tongan subduction zone, Western Alps and Alpine Corsica: Chemical Geology, v. 576, p. 120231, https://doi.org/10.1016/J.CHEMGEO.2021.120231.

Ahmad, Q., Wille, M., Rosca, C., Labidi, J., Schmid, T., Mezger, K., and König, S., 2022, Molybdenum isotopes in plume-influenced MORBs reveal recycling of ancient anoxic sediments: Geochemical Perspectives Letters, v. 23, p. 43–48, https://doi.org/10.7185/GEOCHEMLET.2236.

Andersen, M.B., Elliott, T., Freymuth, H., Sims, K.W.W., Niu, Y., and Kelley, K.A., 2015, The terrestrial uranium isotope cycle: Nature 2015 517:7534, v. 517, p. 356–359, https://doi.org/10.1038/nature14062.

Andres, M., Blichert-Toft, J., and Schilling, J.-G., 2002, Hafnium isotopes in basalts from the southern Mid-Atlantic Ridge from 40°S to 55°S: Discovery and Shona plume–ridge interactions and the role of recycled sediments: Geochemistry, Geophysics, Geosystems, v. 3, p. 1–25, https://doi.org/10.1029/2002GC000324.

Bali, E., Keppler, H., and Audetat, A., 2012, The mobility of W and Mo in subduction zone fluids and the Mo-W-Th-U systematics of island arc magmas: Earth and Planetary Science Letters, v. 351–352, p. 195–207, https://doi.org/10.1016/j.epsl.2012.07.032.

Bezard, R., Fischer-Gödde, M., Hamelin, C., Brennecka, G.A., and Kleine, T., 2016, The effects of magmatic processes and crustal recycling on the molybdenum stable isotopic composition of Mid-Ocean Ridge Basalts: Earth and Planetary Science Letters, v. 453, p. 171–181, https://doi.org/10.1016/j.epsl.2016.07.056.

Bourdon, B., & Van Orman, J. A. 2009, Melting of enriched mantle beneath Pitcairn seamounts: Unusual U–Th–Ra systematics provide insights into melt extraction processes. Earth and Planetary Science Letters, 277(3-4), p. 474-481. https://doi.org/10.1016/j.epsl.2008.11.017.

Bradley, D.C., 2011, Secular trends in the geologic record and the supercontinent cycle: Earth-Science Reviews, v. 108, p. 16–33, https://doi.org/10.1016/j.earscirev.2011.05.003.

Cabral, R.A., Jackson, M.G., Rose-Koga, E.F., Koga, K.T., Whitehouse, M.J., Antonelli, M.A., Farquhar, J., Day, J.M.D., and Hauri, E.H., 2013, Anomalous sulphur isotopes in plume lavas reveal deep mantle storage of Archaean crust: Nature, v. 496, p. 490–493, https://doi.org/10.1038/nature12020.

Campbell, I.H., and Allen, C.M., 2008, Formation of supercontinents linked to increases in atmospheric oxygen: Nature Geoscience, v. 1, p. 554–558, https://doi.org/10.1038/ngeo259.

Chen, S., Hin, R.C., John, T., Brooker, R., Bryan, B., Niu, Y., and Elliott, T., 2019, Molybdenum systematics of subducted crust record reactive fluid flow from underlying slab serpentine dehydration: Nature Communications, v. 10, https://doi.org/10.1038/s41467-019-12696-3.

Chen, S., Sun, P., Niu, Y., Guo, P., Elliott, T., and Hin, R.C., 2022, Molybdenum isotope systematics of lavas from the East Pacific Rise: Constraints on the source of enriched mid-ocean ridge basalt: Earth and Planetary Science Letters, v. 578, p. 117283, https://doi.org/10.1016/J.EPSL.2021.117283.

Chowdhury, P., Dasgupta, R., Phelps, P.R., Costin, G., and Lee, C.T.A., 2022, Oxygen fugacity range of subducting crust inferred from fractionation of trace elements during fluid-present slab melting in the presence of anhydrite versus sulfide: Geochimica et Cosmochimica Acta, v. 325, p. 214–231, https://doi.org/10.1016/J.GCA.2022.02.030.

Clog, M., 2010, Concentration et composition isotopique en hydrogène du manteau terrestre. PhD thesis - Institut de Physique du Globe de Paris, Paris, France.

Delavault, H., Chauvel, C., Sobolev, A., and Batanova, V., 2015, Combined petrological, geochemical and isotopic modeling of a plume source: Example of Gambier Island, Pitcairn chain: Earth and Planetary Science Letters, v. 426, p. 23–35, https://doi.org/10.1016/j.epsl.2015.06.013.

Delavault, H., Chauvel, C., Thomassot, E., Devey, C.W., and Dazas, B., 2016, Sulfur and lead isotopic evidence of relic Archean sediments in the Pitcairn mantle plume: Proceedings of the National Academy of Sciences of the United States of America, v. 113, p. 12952–12956, https://doi.org/10.1073/pnas.1523805113.

Dottin, J.W., Labidi, J., Lekic, V., Jackson, M.G., and Farquhar, J., 2020, Sulfur isotope characterization of primordial and recycled sources feeding the Samoan mantle plume: Earth and Planetary Science Letters, v. 534, p. 116073, https://doi.org/10.1016/J.EPSL.2020.116073.

Douglass, J., Schilling, J.-G., and Fontignie, D., 1999, Plume-ridge interactions of the Discovery and Shona mantle plumes with the southern Mid-Atlantic Ridge (40°-55°S): Journal of Geophysical Research: Solid Earth, v. 104, p. 2941–2962, https://doi.org/10.1029/98JB02642.

Dürr, H.H., Meybeck, M., and Dürr, S.H., 2005, Lithologic composition of the Earth's continental surfaces derived from a new digital map emphasizing riverine material transfer: Global Biogeochemical Cycles, v. 19, https://doi.org/10.1029/2005GB002515.

Eguchi, J., Seales, J., and Dasgupta, R., 2020, Great Oxidation and Lomagundi events linked by deep cycling and enhanced degassing of carbon: Nature Geoscience, v. 13, p. 71–76, https://doi.org/10.1038/s41561-019-0492-6.

Eiler, J.M., Farley, K.A., Valley, J.W., Hauri, E., Craig, H., Hart, S.R., and Stolper, E.M., 1997, Oxygen isotope variations in ocean island basalt phenocrysts: Geochimica et Cosmochimica Acta, v. 61, p. 2281–2293, https://doi.org/10.1016/S0016-7037(97)00075-6.

Eiler, J.M., Farley, K.A., Valley, J.W., Stolper, E.M., Hauri, E.H., and Craig, H., 1995, Oxygen isotope evidence against bulk recycled sediment in the mantle sources of Pitcairn Island lavas: Nature 1995 377:6545, v. 377, p. 138–141, https://doi.org/10.1038/377138a0.

Eisele, J., Sharma, M., Galer, S.J.G., Blichert-Toft, J., Devey, C.W., and Hofmann, A.W., 2002, The role of sediment recycling in EM-1 inferred from Os, Pb, Hf, Nd, Sr isotope and trace element systematics of the Pitcairn hotspot: Earth and Planetary Science Letters, v. 196, p. 197–212, https://doi.org/10.1016/S0012-821X(01)00601-X.

Evans, K.A., 2012, The redox budget of subduction zones: Earth-Science Reviews, v. 113, p. 11–32, https://doi.org/10.1016/J.EARSCIREV.2012.03.003.

French, S.W., and Romanowicz, B., 2015, Broad plumes rooted at the base of the Earth's mantle beneath major hotspots: Nature 2015 525:7567, v. 525, p. 95–99, https://doi.org/10.1038/nature14876.

Freymuth, H., Vils, F., Willbold, M., Taylor, R.N., and Elliott, T., 2015, Molybdenum mobility and isotopic fractionation during subduction at the Mariana arc: Earth and Planetary Science Letters, v. 432, p. 176–186, https://doi.org/10.1016/j.epsl.2015.10.006.

Gale, A., Dalton, C.A., Langmuir, C.H., Su, Y., and Schilling, J.G., 2013, The mean composition of ocean ridge basalts: Geochemistry, Geophysics, Geosystems, v. 14, p. 489–518, https://doi.org/10.1029/2012GC004334.

Garapić, G., Jackson, M.G., Hauri, E.H., Hart, S.R., Farley, K.A., Blusztajn, J.S., and Woodhead, J.D., 2015, A radiogenic isotopic (He-Sr-Nd-Pb-Os) study of lavas from the Pitcairn hotspot: Implications for the origin of EM-1 (enriched mantle 1): Lithos, v. 228–229, p. 1–11, https://doi.org/10.1016/J.LITHOS.2015.04.010.

Gaschnig, R.M., Rader, S.T., Reinhard, C.T., Owens, J.D., Planavsky, N., Wang, X., Asael, D., Greaney, A., and Helz, R., 2021a, Behavior of the Mo, Tl, and U isotope systems during differentiation in the Kilauea Iki lava lake: Chemical Geology, v. 574, p. 120239, https://doi.org/10.1016/J.CHEMGEO.2021.120239.

Gaschnig, R.M., Reinhard, C.T., Planavsky, N.J., Wang, X., Asael, D., and Chauvel, C., 2017, The Molybdenum Isotope System as a Tracer of Slab Input in Subduction Zones: An Example From Martinique, Lesser Antilles Arc: Geochemistry, Geophysics, Geosystems, v. 18, p. 4674–4689, https://doi.org/10.1002/2017GC007085.

Gaschnig, R.M., Reinhard, C.T., Planavsky, N.J., Wang, X., Asael, D., and Jackson, M.G., 2021b, The impact of primary processes and secondary alteration on the stable isotope composition of ocean island basalts: Chemical Geology, v. 581, p. 120416, doi:10.1016/J.CHEMGEO.2021.120416.

Greaney, A.T., Rudnick, R.L., Romaniello, S.J., Johnson, A.C., Gaschnig, R.M., and Anbar, A.D., 2020, Molybdenum isotope fractionation in glacial diamictites tracks the onset of oxidative weathering of the continental crust: Earth and Planetary Science Letters, v. 534, p. 116083, doi:10.1016/J.EPSL.2020.116083.

Greber, N.D., Pettke, T., and Nägler, T.F., 2014, Magmatic–hydrothermal molybdenum isotope fractionation and its relevance to the igneous crustal signature: Lithos, v. 190–191, p. 104–110, doi:10.1016/J.LITHOS.2013.11.006.

Hekinian, R. et al., 2003, The Pitcairn hotspot in the South Pacific: distribution and composition of submarine volcanic sequences: Journal of Volcanology and Geothermal Research, v. 121, p. 219–245, https://doi.org/10.1016/S0377-0273(02)00427-4.

Hin, R.C., Hibbert, K.E.J., Chen, S., Willbold, M., Andersen, M.B., Kiseeva, E.S., Wood, B.J., Niu, Y., Sims, K.W.W., and Elliott, T., 2022, The influence of crustal recycling on the molybdenum isotope composition of the Earth's mantle: Earth and Planetary Science Letters, v. 595, p. 117760, https://doi.org/10.1016/J.EPSL.2022.117760.

Honda, M., and Woodhead, J.D., 2005, A primordial solar-neon enriched component in the source of EM-I-type ocean island basalts from the Pitcairn Seamounts, Polynesia: Earth and Planetary Science Letters, v. 236, p. 597–612, https://doi.org/10.1016/J.EPSL.2005.05.038.

Jackson, M.G., Becker, T.W., and Konter, J.G., 2018, Geochemistry and Distribution of Recycled Domains in the Mantle Inferred From Nd and Pb Isotopes in Oceanic Hot Spots: Implications for Storage in the Large Low Shear Wave Velocity Provinces: Geochemistry, Geophysics, Geosystems, v. 19, p. 3496–3519, https://doi.org/10.1029/2018GC007552.

Jackson, M.G., Becker, T.W., and Steinberger, B., 2021, Spatial Characteristics of Recycled and Primordial Reservoirs in the Deep Mantle: Geochemistry, Geophysics, Geosystems, v. 22, p. e2020GC009525, https://doi.org/10.1029/2020GC009525.

Kaufmann, A.K.C., Pettke, T., and Wille, M., 2021, Molybdenum isotope fractionation at upper-crustal magmatic-hydrothermal conditions: Chemical Geology, v. 578, p. 120319, https://doi.org/10.1016/J.CHEMGEO.2021.120319.

Keller, C.B., and Schoene, B., 2012, Statistical geochemistry reveals disruption in secular lithospheric evolution about 2.5 Gyr ago: Nature, v. 485, p. 490–493, https://doi.org/10.1038/nature11024.

Kendall, B., Dahl, T.W., and Anbar, A.D., 2017, Good Golly, Why Moly? The stable isotope geochemistry of molybdenum, in Non-Traditional Stable Isotopes, Walter de Gruyter GmbH, v. 82, p. 683–732, https://doi.org/10.2138/rmg.2017.82.16.

König, S., Wille, M., Voegelin, A., and Schoenberg, R., 2016, Molybdenum isotope systematics in subduction zones: Earth and Planetary Science Letters, v. 447, p. 95–102, https://doi.org/10.1016/j.epsl.2016.04.033.

Kump, L.R., and Barley, M.E., 2007, Increased subaerial volcanism and the rise of atmospheric oxygen 2.5 billion years ago: Nature 2007 448:7157, v. 448, p. 1033–1036, https://doi.org/10.1038/nature06058.

Laakso, T.A., and Schrag, D.P., 2019, A small marine biosphere in the Proterozoic: Geobiology, v. 17, p. 161–171, https://doi.org/10.1111/GBI.12323.

Labidi, J., Cartigny, P., and Moreira, M., 2013, Non-chondritic sulphur isotope composition of the terrestrial mantle: Nature 2013 501:7466, v. 501, p. 208–211, https://doi.org/10.1038/nature12490.

Labidi, J., Dottin, J.W., Clog, M., Hemond, C., and Cartigny, P., 2022, Near-zero 33S and 36S anomalies in Pitcairn basalts suggest Proterozoic sediments in the EM-1 mantle plume: Earth and Planetary Science Letters, v. 584, p. 117422, https://doi.org/10.1016/J.EPSL.2022.117422.

Lee, C.-T.A., Yeung, L.Y., McKenzie, N.R., Yokoyama, Y., Ozaki, K., and Lenardic, A., 2016, Two-step rise of atmospheric oxygen linked to the growth of continents: Nature Geoscience, v. 9, p. 417–424, https://doi.org/10.1038/ngeo2707.

Li, Z.X., Mitchell, R.N., Spencer, C.J., Ernst, R., Pisarevsky, S., Kirscher, U., and Murphy, J.B., 2019, Decoding Earth’s rhythms: Modulation of supercontinent cycles by longer superocean episodes: Precambrian Research, v. 323, p. 1–5, https://doi.org/10.1016/j.precamres.2019.01.009.

Liang, Y.H., Halliday, A.N., Siebert, C., Fitton, J.G., Burton, K.W., Wang, K.L., and Harvey, J., 2017, Molybdenum isotope fractionation in the mantle: Geochimica et Cosmochimica Acta, v. 199, p. 91–111, https://doi.org/10.1016/j.gca.2016.11.023.

Liu, H., Zartman, R.E., Ireland, T.R., and Sun, W. dong, 2019, Global atmospheric oxygen variations recorded by Th/U systematics of igneous rocks: Proceedings of the National Academy of Sciences of the United States of America, v. 116, p. 18854–18859, https://doi.org/10.1073/pnas.1902833116.

Lyons, T.W., Reinhard, C.T., and Planavsky, N.J., 2014, The rise of oxygen in Earth's early ocean and atmosphere: Nature 2014 506:7488, v. 506, p. 307–315, https://doi.org/10.1038/nature13068.

Ma, L., Xu, Y.G., Li, J., Chen, L.H., Liu, J.Q., Li, H.Y., Huang, X.L., Ma, Q., Hong, L.B., and Wang, Y., 2022, Molybdenum isotopic constraints on the origin of EM1-type continental intraplate basalts: Geochimica et Cosmochimica Acta, v. 317, p. 255–268, https://doi.org/10.1016/J.GCA.2021.11.013.

McCoy-West, A.J., Chowdhury, P., Burton, K.W., Sossi, P., Nowell, G.M., Fitton, J.G., Kerr, A.C., Cawood, P.A., and Williams, H.M., 2019, Extensive crustal extraction in Earth's early history inferred from molybdenum isotopes: Nature Geoscience, v. 12, p. 946–951, https://doi.org/10.1038/s41561-019-0451-2.

Michael, P.J., and Cornell, W.C., 1998, Influence of spreading rate and magma supply on crystallization and assimilation beneath mid-ocean ridges: Evidence from chlorine and major element chemistry of mid-ocean ridge basalts: Journal of Geophysical Research: Solid Earth, v. 103, p. 18325–18356, https://doi.org/10.1029/98JB00791.

Nebel-Jacobsen, Y., Wille, M., Ivanic, T., and Nebel, O., 2021, Molybdenum isotope systematics in cumulate rock of the 2.8 Windimurra layered intrusion: A test for igneous differentiation and the composition of the Archean mantle: Precambrian Research, v. 355, p. 106087, https://doi.org/10.1016/J.PRECAMRES.2020.106087.

Newsom, H.E., White, W.M., Jochum, K.P., and Hofmann, A.W., 1986, Siderophile and chalcophile element abundances in oceanic basalts, Pb isotope evolution and growth of the Earth's core: Earth and Planetary Science Letters, v. 80, p. 299–313, https://doi.org/10.1016/0012-821X(86)90112-3.

Plank, T., and Langmuir, C.H., 1998, The chemical composition of subducting sediment and its consequences for the crust and mantle: Chemical Geology, v. 145, p. 325–394, https://doi.org/10.1016/S0009-2541(97)00150-2.

Putirka, K., 2008, Excess temperatures at ocean islands: Implications for mantle layering and convection: Geology, v. 36, p. 283–286, https://doi.org/10.1130/G24615A.1.

Richards, J.P., and Mumin, A.H., 2013, Magmatic-hydrothermal processes within an evolving Earth: Iron oxide-copper-gold and porphyry Cu ± Mo ± Au deposits: Geology, v. 41, p. 767–770, https://doi.org/10.1130/G34275.1.

le Roux, P.J., Le Roex, A.P., Schilling, J.G., Shimizu, N., Perkins, W.W., and Pearce, N.J.G., 2002, Mantle heterogeneity beneath the southern Mid-Atlantic Ridge: trace element evidence for contamination of ambient asthenospheric mantle: Earth and Planetary Science Letters, v. 203, p. 479–498, https://doi.org/10.1016/S0012-821X(02)00832-4.

Skora, S., Freymuth, H., Blundy, J., Elliott, T., and Guillong, M., 2017, An experimental study of the behaviour of cerium/molybdenum ratios during subduction: Implications for tracing the slab component in the Lesser Antilles and Mariana Arc: Geochimica et Cosmochimica Acta, v. 212, p. 133–155, https://doi.org/10.1016/j.gca.2017.05.025.

Smit, M.A., and Mezger, K., 2017, Earth's early O2 cycle suppressed by primitive continents: Nature Geoscience, v. 10, p. 788–792, doi:10.1038/ngeo3030.

Stolper, D.A., and Bucholz, C.E., 2019, Neoproterozoic to early Phanerozoic rise in island arc redox state due to deep ocean oxygenation and increased marine sulfate levels: Proceedings of the National Academy of Sciences of the United States of America, v. 116, p. 8746–8755, https://doi.org/10.1073/pnas.1821847116.

Stracke, A., 2012, Earth's heterogeneous mantle: A product of convection-driven interaction between crust and mantle: Chemical Geology, v. 330–331, p. 274–299, https://doi.org/10.1016/J.CHEMGEO.2012.08.007.

Voegelin, A.R., Nägler, T.F., Samankassou, E., and Villa, I.M., 2009, Molybdenum isotopic composition of modern and Carboniferous carbonates: Chemical Geology, v. 265, p. 488–498, https://doi.org/10.1016/j.chemgeo.2009.05.015.

Voegelin, A.R., Pettke, T., Greber, N.D., von Niederhäusern, B., and Nägler, T.F., 2014, Magma differentiation fractionates Mo isotope ratios: Evidence from the Kos Plateau Tuff (Aegean Arc): Lithos, v. 190–191, p. 440–448, https://doi.org/10.1016/j.lithos.2013.12.016.

Wang, X.J. et al., 2018, Recycled ancient ghost carbonate in the Pitcairn mantle plume: Proceedings of the National Academy of Sciences of the United States of America, v. 115, p. 8682–8687, https://doi.org/10.1073/pnas.1719570115.

Willbold, M., and Stracke, A., 2006, Trace element composition of mantle end-members: Implications for recycling of oceanic and upper and lower continental crust: Geochemistry, Geophysics, Geosystems, v. 7, https://doi.org/10.1029/2005GC001005.

Wille, M., Nebel, O., Pettke, T., Vroon, P.Z., König, S., and Schoenberg, R., 2018, Molybdenum isotope variations in calc-alkaline lavas from the Banda arc, Indonesia: Assessing the effect of crystal fractionation in creating isotopically heavy continental crust: Chemical Geology, v. 485, p. 1–13, https://doi.org/10.1016/j.chemgeo.2018.02.037.

Woodhead, J., and McCulloch, M., 1989, Ancient seafloor signals in Pitcairn Island lavas and evidence for large amplitude, small length-scale mantle heterogeneities: Earth and Planetary Science Letters, v. 94, p. 257–273, https://doi.org/10.1016/0012-821X(89)90145-3.

Yang, J., Siebert, C., Barling, J., Savage, P., Liang, Y.H., and Halliday, A.N., 2015, Absence of molybdenum isotope fractionation during magmatic differentiation at Hekla volcano, Iceland: Geochimica et Cosmochimica Acta, v. 162, p. 126–136, https://doi.org/10.1016/j.gca.2015.04.011.

Yierpan, A., König, S., Labidi, J., and Schoenberg, R., 2020, Recycled selenium in hot spot–influenced lavas records ocean-atmosphere oxygenation: Science Advances, v. 6, p. eabb6179, https://doi.org/10.1126/SCIADV.ABB6179.

Zerkle, A.L., 2018, Biogeodynamics: bridging the gap between surface and deep Earth processes: Philosophical Transactions of the Royal Society A: Mathematical, Physical and Engineering Sciences, v. 376, https://doi.org/10.1098/RSTA.2017.0401.

# Supplementary Material

## Analytical methods

Molybdenum purification and isotope analysis were conducted in the clean laboratory facilities at the Institute of Geological Sciences, University of Bern. For all samples, enough powder was weighed to have 100 to 500 ng Mo for each analysis. The sample was spiked with an enriched isotope tracer solution ($^{97}$Mo-$^{100}$Mo double spike) prior to dissolution. The samples were dissolved in concentrated single-distilled HF-$HNO_3$ (1.5 mL:0.5 mL mixture) in Savillex™ Teflon® vials at 100°C for at least 24 h. To minimize fluorides, additional 0.5 mL of concentrated $HNO_3$ was added to the sample during evaporation. The dry residue was then re-dissolved in 6 M HCl and heated for at least 24 h. To further minimize fluorides, this step was conducted three times, with increasing the heating temperature during each of these steps in the order: (i) 100 °C, (ii) 120 °C, (iii) 140 °C.

The dissolved samples were processed through anion- and cation exchange columns to obtain a clean Mo separate (Wille et al., 2013). In the first step, samples were taken up in 3 ml 4 M HCl + 0.15% $H_2O_2$ and passed through 1.5 ml Dowex 1X8, 200-400 mesh, anion resin (circa 10 mm column width). Additional 4 ml of the loading acid and 2 ml of 18.2 MΩ·cm deionized water were used to elute most matrix elements except for Fe, which was subsequently eluted with 6 ml 3 M $HNO_3$ together with Mo. In a second step, the sample material was taken up in 2 ml of 0.5 M HCl + 0.10% $H_2O_2$ and passed through 2 ml Dowex 50WX8 200-400 mesh cation exchange resin (circa 10 mm column width) to separate Fe. Additional 5 ml of the loading acid were used to quantitatively recover Mo. Measurement of stable Mo isotopes were carried out on a Neptune Plus MC-ICP-MS coupled with an Aridus II desolvating nebulizer with an uptake rate of 100 $\mu l \cdot min^{-1}$ (details are provided in Ahmad et al., 2021). Six Mo isotopes ($^{94}$Mo, $^{95}$Mo, $^{96}$Mo, $^{97}$Mo, $^{98}$Mo, and $^{100}$Mo) were measured simultaneously as well as $^{99}$Ru and $^{101}$Ru to monitor potential isobaric interference. All isotopes were measured with $10^{-11}$ Ω resistors with the exception of $^{101}$Ru, which was measured using a $10^{-12}$ Ω resistor. A combination of 'H' Ni sampler cone and 'H' Ni skimmer cone for analyses provides a signal intensity of ~ 45 V/ppm on $^{95}$Mo. A double spike correction method based on an iterative calculation procedure (see Siebert et al., 2001) was used to obtain the natural isotope ratios of the sample. The total procedural blank was 0.71 to 0.74 ng, which is less than 1 % of the total analyzed Mo. Mo isotope compositions are presented in the δ-notation relative to NIST SRM 3134 in ‰ (Greber et al., 2012; Goldberg et al., 2013) with an interference correction based on $^{99}$Ru:

$$\delta^{98/95}\mathrm{Mo} = \left( \frac{\left(\frac{^{98}\mathrm{Mo}}{^{95}\mathrm{Mo}}\right)_{\mathrm{Sample}}}{\left(\frac{^{98}\mathrm{Mo}}{^{95}\mathrm{Mo}}\right)_{\mathrm{NIST\ SRM\ 3134}}} - 1 \right) * 1{,}000$$

$\delta^{98/95}$Mo values corrected for Ru interferences using $^{99}$Ru and $^{101}$Ru were compared to ensure accurate correction for Ru interference on Mo ($\Delta^{98/95}\mathrm{Mo}_{^{99}\mathrm{Ru}-^{101}\mathrm{Ru}} < 0.01$ ‰). To correct for background Mo, sample measurements were bracketed by samples with measurements of 0.5 M $HNO_3$ carrier solution on-peak. Mo isotope signals in the background solution were $10^4$ times smaller than during the sample measurement. Sample and background analyses consisted of 80 and 10 cycles, respectively, with a signal integration time of 4.194 s for each cycle. Repeated measurements of the standard NIST SRM 3134 and an in-house J&M standard solution (JMCBern) lot 602332B gave an isotopic difference of $\Delta^{98/95}$Mo = 0.260 ± 0.023 ‰ (2 SD, n = 10), in agreement with other studies (Greber et al., 2012; Ahmad et al., 2021, 2022; Kaufmann et al., 2021; O'Sullivan et al., 2021). Solution standards were measured at a concentration of 50 ppb. Chemically purified whole-rock reference materials AGV-2 and BHVO-2 yielded a $\delta^{98/95}$Mo of −0.175 ± 0.037 ‰ (2 SD, n = 3) and −0.077 ± 0.024 ‰ (2 SD, n = 3) (Table S-1). The values are within uncertainty of those determined previously (e.g., Burkhardt et al., 2014; Willbold et al., 2016; Zhao et al., 2016). Individual measurements of whole rock reference materials (Table S-1) are within the long-term 2SD external reproducibility of ± 0.05 ‰ as determined by previous measurements of BHVO-2 (Ahmad et al., 2021, 2022).

Including previous BHVO-2 measurements (−0.09 ± 0.05 ‰; n = 11), we consider ± 0.05 ‰ as the long-term 2 SD external reproducibility of the sample measurements. All samples and whole-rock reference materials were measured multiple times (after one single digestion and chemical separation) and obtained $\delta^{98/95}$Mo values were averaged for data presentation and interpretation (Table S-1). All individual sample measurements differ less than ± 0.05 ‰ from their average $\delta^{98/95}$Mo.

## Individual data

***Table S-1.*** *Average and individual Mo isotope data of analyzed Pitcairn Island lavas. Individual measurements are from the same chromatographic aliquot. *Internal precision on a sample run (over 80 cycles) is reported as 2 standard error (2 SE).*

| | Individual measurements | | Mean values | | |
|---|---|---|---|---|---|
| **Sample** | **$\delta^{98/95}$Mo (‰)** | **2 SE* (‰)** | **$\delta^{98/95}$Mo (‰)** | **2 SD (‰)** | **Mo (µg/g)** |
| ***Pitcairn island basalts*** | | | | | |
| pn03-08 | −0.133 | 0.013 | −0.119 | 0.039 | 2.93 |
| | −0.097 | 0.016 | | | |
| | −0.127 | 0.014 | | | |
| pn03-10 | −0.125 | 0.015 | −0.115 | 0.030 | 1.38 |
| | −0.104 | 0.014 | | | |
| pn03-01 | −0.082 | 0.014 | −0.121 | 0.067 | 2.47 |
| | −0.133 | 0.015 | | | |
| | −0.146 | 0.016 | | | |
| pn03-02 | −0.119 | 0.016 | −0.121 | 0.006 | 1.26 |
| | −0.123 | 0.013 | | | |
| pn03-03 | −0.117 | 0.016 | −0.112 | 0.009 | 2.45 |
| | −0.108 | 0.015 | | | |
| | −0.111 | 0.016 | | | |
| pn03-05 | −0.120 | 0.012 | −0.113 | 0.026 | 2.23 |
| | −0.098 | 0.017 | | | |
| | −0.120 | 0.012 | | | |
| pn03-07 | −0.113 | 0.014 | −0.111 | 0.007 | 1.53 |
| | −0.108 | 0.017 | | | |
| pn03-11 | −0.115 | 0.016 | −0.111 | 0.022 | 2.41 |
| | −0.119 | 0.014 | | | |
| | −0.098 | 0.014 | | | |
| pn14-14 | −0.090 | 0.018 | −0.093 | 0.013 | 4.22 |
| | −0.101 | 0.016 | | | |
| | −0.090 | 0.019 | | | |
| pn08-07 | −0.077 | 0.017 | −0.097 | 0.039 | 4.40 |
| | −0.117 | 0.015 | | | |
| | −0.098 | 0.018 | | | |

| | | | | | |
|---|---|---|---|---|---|
| ***Rock reference materials*** | | | | | |
| BHVO-2 | −0.090 | 0.015 | −0.077 | 0.025 | 3.59 |
| | −0.066 | 0.014 | | | |
| | −0.076 | 0.017 | | | |
| AGV-2 | −0.187 | 0.015 | −0.175 | 0.037 | 2.00 |
| | −0.154 | 0.016 | | | |
| | −0.185 | 0.016 | | | |

## Misfit model

The applied misfit algorithm to model potential sediment end members is from Ahmad et al. (2022). In the misfit plot (Fig. 4), the best agreement between potential sediment end members and measured samples is given by the least squares error (blue field) of the misfit function. The white dashed line indicates the sample amount multiplied by the external 2 SD reproducibility to obtain a conservative upper limit for model compositions. The white solid line indicates the contour line of the least squares error (see minimum $\Delta^{98/95}$Mo in Fig. 4a, b) with added $\Delta^{98/95}$Mo ≈ 0.1 ‰. For comparison, the compositions of OM-rich sediments sorted by age intervals (Ye et al., 2021; Table S-2), UCC (Voegelin et al., 2014; Greber et al., 2014; Rudnick and Gao, 2014; Freymuth et al., 2015; Willbold and Elliott, 2017; Yang et al., 2017; Greaney et al., 2020), MORB (Gale et al., 2013; Bezard et al., 2016; Chen et al., 2022), pelagic Mn-rich and clastic metasediments (Ahmad et al., 2021), and blueschists and MORB-type eclogites (Chen et al., 2019; Ahmad et al., 2021) are plotted (Fig. 4).

***Table S-2.*** *Parameters from the two-component mixing model (Fig. 4) and compositions of marine sediments. The misfit calculation is conducted based on Mo-Sr systematics.*

| | $\delta^{98/95}$Mo (‰) | [Mo] (µg/g) | $^{87}$Sr/$^{86}$Sr | Sr (µg/g) | $^{143}$Nd/$^{144}$Nd | Nd (µg/g) |
|---|---|---|---|---|---|---|
| ***End members*** | | | | | | |
| Ambient depleted mantle[A] | −0.204 ± 0.008 | 0.025 ± 0.007 | 0.702819 | 11.32 | 0.51312 | 1.118 |
| 1.5 Ga old recycled pelagic sediment[B] | | | 0.7203 | 300 ± 17 | 0.5117 | 85 ± 5.2 |
| Neo-Archean carbonate "Pitcairn Component" [C] | 0.75 ± 0.2 | 0.01 to 0.1 | 0.708000 | 120 | 0.511264 | 8 |
| Upper continental crust[D] | 0.05 to 0.15 | 1.1 ± 0.2 | | | | |
| ***Marine sediments***[E] | | | | | | |
| Archean | 0.218 ± 0.150<br>($M$ = 19, $N$ = 417) | $4.70^{+18.4}_{-3.75}$<br>($M$ = 19, $N$ = 744) | | | | |
| Proterozoic | 0.244 ± 0.114<br>($M$ = 51, $N$ = 696) | $4.10^{+17.0}_{-3.30}$<br>($M$ = 53, $N$ = 1262) | | | | |
| Phanerozoic | 0.528 ± 0.132<br>($M$ = 48, $N$ = 882) | $22.9^{+49.7}_{-15.7}$<br>($M$ = 48, $N$ = 1154) | | | | |

[A] Ambient depleted mantle values from (Salters and Stracke, 2004; Delavault et al., 2016; McCoy-West et al., 2019)

[B] 1.5 Ga recycled pelagic sediment values from (Ahmad et al., 2022 and references therein)

[C] Neo-Archean carbonate values are from (Delavault et al., 2016) and (Voegelin et al., 2009, 2010)

[D] Upper continental crust values are from (Voegelin et al., 2014; Greber et al., 2014; Rudnick and Gao, 2014; Freymuth et al., 2015; Willbold and Elliott, 2017; Yang et al., 2017; Greaney et al., 2020)

[E] Marine sediment values of different eons are log-normal means of sediments sorted by age intervals (>1 Myr) from the literature (see compilation of Ye et al., 2021). The literature data represent mostly shallow-marine (continental shelf/closed basins) sediments from anoxic/euxinic settings, where e.g., sulfate reduction leads to higher authigenic accumulation of isotopically heavy Mo from seawater compared to lower Mo accumulation in the anoxic deep-sea (see main text).

## Supplementary Information References

Ahmad, Q., Wille, M., König, S., Rosca, C., Hensel, A., Pettke, T., and Hermann, J., 2021, The Molybdenum isotope subduction recycling conundrum: A case study from the Tongan subduction zone, Western Alps and Alpine Corsica: Chemical Geology, v. 576, p. 120231, https://doi.org/10.1016/J.CHEMGEO.2021.120231.

Ahmad, Q., Wille, M., Rosca, C., Labidi, J., Schmid, T., Mezger, K., and König, S., 2022, Molybdenum isotopes in plume-influenced MORBs reveal recycling of ancient anoxic sediments: Geochemical Perspectives Letters, v. 23, p. 43–48, https://doi.org/10.7185/GEOCHEMLET.2236.

Bezard, R., Fischer-Gödde, M., Hamelin, C., Brennecka, G.A., and Kleine, T., 2016, The effects of magmatic processes and crustal recycling on the molybdenum stable isotopic composition of Mid-Ocean Ridge Basalts: Earth and Planetary Science Letters, v. 453, p. 171–181, https://doi.org/10.1016/j.epsl.2016.07.056.

Burkhardt, C., Hin, R.C., Kleine, T., and Bourdon, B., 2014, Evidence for Mo isotope fractionation in the solar nebula and during planetary differentiation: Earth and Planetary Science Letters, v. 391, p. 201–211, https://doi.org/10.1016/j.epsl.2014.01.037.

Chen, S., Hin, R.C., John, T., Brooker, R., Bryan, B., Niu, Y., and Elliott, T., 2019, Molybdenum systematics of subducted crust record reactive fluid flow from underlying slab serpentine dehydration: Nature Communications, v. 10, https://doi.org/10.1038/s41467-019-12696-3.

Chen, S., Sun, P., Niu, Y., Guo, P., Elliott, T., and Hin, R.C., 2022, Molybdenum isotope systematics of lavas from the East Pacific Rise: Constraints on the source of enriched mid-ocean ridge basalt: Earth and Planetary Science Letters, v. 578, p. 117283, https://doi.org/10.1016/J.EPSL.2021.117283.

Delavault, H., Chauvel, C., Thomassot, E., Devey, C.W., and Dazas, B., 2016, Sulfur and lead isotopic evidence of relic Archean sediments in the Pitcairn mantle plume: Proceedings of the National Academy of Sciences of the United States of America, v. 113, p. 12952–12956, https://doi.org/10.1073/pnas.1523805113.

Freymuth, H., Vils, F., Willbold, M., Taylor, R.N., and Elliott, T., 2015, Molybdenum mobility and isotopic fractionation during subduction at the Mariana arc: Earth and Planetary Science Letters, v. 432, p. 176–186, https://doi.org/10.1016/j.epsl.2015.10.006.

Gale, A., Dalton, C.A., Langmuir, C.H., Su, Y., and Schilling, J.G., 2013, The mean composition of ocean ridge basalts: Geochemistry, Geophysics, Geosystems, v. 14, p. 489–518, https://doi.org/10.1029/2012GC004334.

Goldberg, T., Gordon, G., Izon, G., Archer, C., Pearce, C.R., McManus, J., Anbar, A.D., and Rehkämper, M., 2013, Resolution of inter-laboratory discrepancies in Mo isotope data: An intercalibration: Journal of Analytical Atomic Spectrometry, v. 28, p. 724–735, https://doi.org/10.1039/c3ja30375f.

Greaney, A.T., Rudnick, R.L., Romaniello, S.J., Johnson, A.C., Gaschnig, R.M., and Anbar, A.D., 2020, Molybdenum isotope fractionation in glacial diamictites tracks the onset of oxidative weathering of the continental crust: Earth and Planetary Science Letters, v. 534, p. 116083, https://doi.org/10.1016/J.EPSL.2020.116083.

Greber, N.D., Pettke, T., and Nägler, T.F., 2014, Magmatic–hydrothermal molybdenum isotope fractionation and its relevance to the igneous crustal signature: Lithos, v. 190–191, p. 104–110, https://doi.org/10.1016/J.LITHOS.2013.11.006.

Greber, N.D., Siebert, C., Nägler, T.F., and Pettke, T., 2012, δ98/95Mo values and Molybdenum Concentration Data for NIST SRM 610, 612 and 3134: Towards a Common Protocol for Reporting Mo Data: Geostandards and Geoanalytical Research, v. 36, p. 291–300, https://doi.org/10.1111/j.1751-908X.2012.00160.x.

McCoy-West, A.J., Chowdhury, P., Burton, K.W., Sossi, P., Nowell, G.M., Fitton, J.G., Kerr, A.C., Cawood, P.A., and Williams, H.M., 2019, Extensive crustal extraction in Earth's early history inferred from molybdenum isotopes: Nature Geoscience, v. 12, p. 946–951, https://doi.org/10.1038/s41561-019-0451-2.

Rudnick, R.L., and Gao, S., 2014, Composition of the Continental Crust, in Treatise on Geochemistry: Second Edition, Elsevier Inc., v. 4, p. 1–51, https://doi.org/10.1016/B978-0-08-095975-7.00301-6.

Salters, V.J.M., and Stracke, A., 2004, Composition of the depleted mantle: Geochemistry, Geophysics, Geosystems, v. 5, Q05B07, https://doi.org/10.1029/2003GC000597.

Siebert, C., Nägler, T.F., and Kramers, J.D., 2001, Determination of molybdenum isotope fractionation by double-spike multicollector inductively coupled plasma mass spectrometry: Geochemistry, Geophysics, Geosystems, v. 2, https://doi.org/10.1029/2000GC000124.

Voegelin, A.R., Nägler, T.F., Samankassou, E., and Villa, I.M., 2009, Molybdenum isotopic composition of modern and Carboniferous carbonates: Chemical Geology, v. 265, p. 488–498, https://doi.org/10.1016/j.chemgeo.2009.05.015.

Voegelin, A. R., Nägler, T. F., Beukes, N. J., & Lacassie, J. P. 2010, Molybdenum isotopes in late Archean carbonate rocks: implications for early Earth oxygenation. Precambrian Research, 182(1-2), p. 70-82. https://doi.org/10.1016/j.precamres.2010.07.001.

Voegelin, A.R., Pettke, T., Greber, N.D., von Niederhäusern, B., and Nägler, T.F., 2014, Magma differentiation fractionates Mo isotope ratios: Evidence from the Kos Plateau Tuff (Aegean Arc): Lithos, v. 190–191, p. 440–448, https://doi.org/10.1016/j.lithos.2013.12.016.

Willbold, M., and Elliott, T., 2017, Molybdenum isotope variations in magmatic rocks: Chemical Geology, v. 449, p. 253–268, https://doi.org/10.1016/j.chemgeo.2016.12.011.

Willbold, M., Hibbert, K., Lai, Y.-J., Freymuth, H., Hin, R.C., Coath, C., Vils, F., and Elliott, T., 2016, High-Precision Mass-Dependent Molybdenum Isotope Variations in Magmatic Rocks Determined by Double-Spike MC-ICP-MS: Geostandards and Geoanalytical Research, v. 40, p. 389–403, https://doi.org/10.1111/j.1751-908X.2015.00388.x.

Wille, M., Nebel, O., Van Kranendonk, M.J., Schoenberg, R., Kleinhanns, I.C., and Ellwood, M.J., 2013, Mo-Cr isotope evidence for a reducing Archean atmosphere in 3.46-2.76Ga black shales from the Pilbara, Western Australia: Chemical Geology, v. 340, p. 68–76, https://doi.org/10.1016/j.chemgeo.2012.12.018.

Yang, J., Barling, J., Siebert, C., Fietzke, J., Stephens, E., and Halliday, A.N., 2017, The molybdenum isotopic compositions of I-, S- and A-type granitic suites: Geochimica et Cosmochimica Acta, v. 205, p. 168–186, https://doi.org/10.1016/j.gca.2017.01.027.

Ye, Y., Zhang, S., Wang, H., Wang, X., Tan, C., Li, M., Wu, C., and Canfield, D.E., 2021, Black shale Mo isotope record reveals dynamic ocean redox during the Mesoproterozoic Era: Geochemical Perspectives Letters, v. 18, p. 16–21, https://doi.org/10.7185/GEOCHEMLET.2118.

Zhao, P.-P., Li, J., Zhang, L., Wang, Z.-B., Kong, D.-X., Ma, J.-L., Wei, G.-J., and Xu, J.-F., 2016, Molybdenum Mass Fractions and Isotopic Compositions of International Geological Reference Materials: Geostandards and Geoanalytical Research, v. 40, p. 217–226, https://doi.org/10.1111/j.1751-908X.2015.00373.x.

# Erklärung

gemäss Art. 18 PromR Phil.-nat. 2019

Name/Vorname:

Matrikelnummer:

Studiengang:

Bachelor ☐ Master ☐ Dissertation ☐

Titel der Arbeit:

LeiterIn der Arbeit:

Ich erkläre hiermit, dass ich diese Arbeit selbständig verfasst und keine anderen als die angegebenen Quel-len benutzt habe. Alle Stellen, die wörtlich oder sinn-gemäss aus Quellen entnommen wurden, habe ich als solche gekennzeichnet. Mir ist bekannt, dass andern-falls der Senat gemäss Artikel 36 Absatz 1 Buchstabe r des Gesetzes über die Universität vom 5. September 1996 und Artikel 69 des Universitätssta-tuts vom 7. Juni 2011 zum Entzug des Doktortitels be-rechtigt ist.
Für die Zwecke der Begutachtung und der Überprüfung der Einhaltung der Selbständigkeitserklärung bzw. der Reglemente betreffend Plagiate erteile ich der Univer-sität Bern das Recht, die dazu erforderlichen Perso-nendaten zu bearbeiten und Nutzungshandlungen vor-zunehmen, insbesondere die Doktorarbeit zu vervielfäl-tigen und dauerhaft in einer Datenbank zu speichern sowie diese zur Überprüfung von Arbeiten Dritter zu verwenden oder hierzu zur Verfügung zu stellen.

Ort/Datum

Unterschrift